



University
of Glasgow

Steele, Genevieve (2014) *Higgs boson searches within ATLAS: combination of channel sensitivities and extension of search range to heavy masses*. PhD thesis.

<http://theses.gla.ac.uk/5536/>

Copyright and moral rights for this thesis are retained by the author

A copy can be downloaded for personal non-commercial research or study, without prior permission or charge

This thesis cannot be reproduced or quoted extensively from without first obtaining permission in writing from the Author

The content must not be changed in any way or sold commercially in any format or medium without the formal permission of the Author

When referring to this work, full bibliographic details including the author, title, awarding institution and date of the thesis must be given

Higgs boson searches within ATLAS:
combination of channel sensitivities and
extension of search range to heavy masses.

Genevieve Steele

Department of Physics and Astronomy,
University of Glasgow

Presented as a thesis for the degree of Ph.D.
in the University of Glasgow, University Avenue,
Glasgow G12 8QQ.

©[G Steele] [2014]

August 4, 2014

Contents

Contents	i
Abstract	v
Declaration	vi
Acknowledgements	vii
Preface	ix
Summary	x
1 CERN, The LHC, ATLAS and more...	1
1.1 Introduction	1
1.1.1 CERN and the Large Hadron Collider	1
1.1.2 ATLAS	4

1.1.2.1	The Inner Detector	6
1.1.2.2	Calorimetry	8
1.1.2.3	Muon Spectrometer	10
1.1.2.4	Magnet System	13
1.1.2.5	Forward Detectors	14
1.1.2.6	Detector Co-ordinate System	15
1.1.2.7	Trigger and Data Acquisition (TDAQ).	16
2	Theory	19
2.1	Introduction	19
2.2	Quantum Electrodynamics	21
2.3	Non-Abelian Gauge Theories.	24
2.4	Electroweak Theory	26
2.5	The Higgs Mechanism	27
2.6	The Search for the Higgs Boson	30
2.7	Production and Decay of the Higgs Boson at the LHC	37
3	Analysis Techniques - Statistics	42
3.1	Introduction.	42

3.2 Hypothesis Testing	43
3.2.1 Log Likelihood Ratio	44
3.2.1.1 LEP Method	48
3.2.1.2 Tevatron Method	48
3.2.1.3 LHC method	49
3.2.2 Limit Setting	49
3.2.3 Quantifying an Excess	51
3.2.4 Bayesian Results	52
3.3 Software Tools	53
3.3.1 MCLimits	53
3.3.2 RooStats	56
3.3.3 Comparison	58
4 Adapting MCLimits in a RooStats Environment	62
4.1 Constraints of MCLimits	62
4.2 MCLimits with XML Interface	63
4.3 MCLimits from Workspaces.	68
4.3.1 HistFactory produced workspaces.	68

4.3.2	Non-HistFactory produced workspaces	76
5	Heavy Higgs Reweighting	85
5.1	Search for the Heavy Higgs	85
5.2	Complex Pole Scheme	86
5.3	Reweighting tool	88
5.3.1	Initial Gluon Gluon Fusion Reweighting	88
5.3.2	Initial Vector Boson Fusion Reweighting	92
5.3.3	Gluon Gluon Fusion Reweighting Tool, Second Incarna- tion.	96
5.3.4	Higgs Interference Effects.	98
5.3.5	Vector Boson Fusion Reweighting Tool Extension	101
5.3.6	Current and Future Use for the Tools.	105
6	Conclusions	112
	Bibliography	114

Abstract

A comparison of the two statistical frameworks, `MCLimits` and `RooStats` is presented in relation to the statistical combination of the decay channels of the Standard Model Higgs boson using data collected by the ATLAS experiment in the period up to the end of the 2012 LHC run. A wrapper mechanism designed to allow the `RooStats` model and data containers to be compatible with `MCLimits` is described. This interface is used to produce statistical plots for single channel and full combination Higgs searches. The `MCLimits` and `RooStats` results are compared and contrasted, showing good agreement throughout the mass range, acting as a double check of the published results.

The extension of the Higgs mass search range above 600 GeV is discussed, including a summary of the Complex Pole Scheme. The implementation of the Complex Pole Scheme is necessary in analyses considering a heavier Higgs-like particle. A framework was created to adjust existing Monte Carlo samples to give an approximation of the Complex Pole Scheme. This allowed quick implementation of this theory and studies of the effects on the existing analyses without the large scale tasks of rerunning all relevant Monte Carlo samples. The framework was adapted to be as general as possible to allow for the inclusion and study of other theories and modifications.

Declaration

I declare that except where explicitly mentioned as the work of others, the work presented in this thesis is my own. This work has not been submitted for any other degree at the University of Glasgow nor any other institution.

Genevieve Steele

Acknowledgements

Whenever my PhD work was going well there was undoubtedly one of the following people somewhere in my work sphere (in no particular order); Sarah Allwood-Spiers, Chris Collins-Tooth, Samir Ferrag, Kostas Nikolopoulos, Daniela Rebuzzi, Sara Diglio, Rei Tanaka. These were the group of people I could rely on to offer help of whatever kind was needed and I hope they all know how much it was appreciated.

Gavin Davies, Val O'Shea and Tony Doyle have my thanks for a viva which was nowhere near as awful as my nightmares had imagined it to be. In fact, on reflection, I enjoyed the time I spent with them in a windowless room, in a basement in CERN, not because of the venue, clearly, but because of the constructive criticism they gave as well as the encouragement that left me more proud of my achievements than ever before.

My supervisors, Dave Britton and Craig Buttar have always had some helpful advice or a kind word, whichever was needed most, and both were needed regularly.

I have been lucky to have trundled through this portion of my life alongside some, now weary, but still happy travellers. Cristy Oropeza Barerra (and Nacho), Mike Alexander (and Emma), Alistair Gemmell (and Jenny), Mike Wright (and Kimbo) have all been great office mates and continue to be great

friends.

My friend, Hel David, idolises me so much she decided to do a PhD herself just to copy off me. Whenever she is having problems understanding how hard things come to those of us that are not geniuses I can always help her out. She is lucky to have me.

Since I was a little girl, every time I have sworn to my parents that I can't do something, that it is just impossible, they have resolutely refused to believe what I say. They are always right. If I end up being half as good a person as my parents are I will have succeeded. I am a very lucky person to have them.

One last person to thank (and a dog, but the dog comes with the person). Aurélien has loved me all through this, long, PhD duration and I hope to repay his love as best I can.

Preface

During the first year of my PhD studies I performed work with the Glasgow ATLAS group, in particular for ATLFast. ATLFast is a fast simulation tool that was developed to help alleviate the problem of large monte carlo dataset requirements. My work, which formed the basis of my qualification as an ATLAS author, was the update of identification efficiencies for hadronic τ decays.

During my time spent on long term attachment at CERN I completed my required shifts working as the ATLAS distributed computing tier 0/1 shifter.

Whilst working on the `MCLimits` and `Roostats` comparison I was associated to the ATLAS Higgs combination working group as well as the joint ATLAS and CMS LHC Higgs working group. I was selected by this group to present the Higgs combination results at Higgs Hunting 2012, shortly after the July 4th announcements of the observation of a new particle.

The work on the implementation of the complex pole scheme in the search for heavy Higgs particles was done in conjunction with the $H \rightarrow ZZ \rightarrow ll\nu\nu$ working group. Through this I also became involved with the LHC Higgs cross-section working group. I left ATLAS to work on the SPS before the publication of several reports for which I played a key role.

Summary

Chapter 1 is a summary of the hardware used in the taking of the data analysed in this thesis. It contains an overview of the LHC and its experiments, focussing mainly on the ATLAS experiment. The subdetectors of the ATLAS experiment are described.

Chapter 2 is a walk through the theories relevant to the work of this thesis. It considers the theoretical building blocks of the Standard Model and leads into the development of the Higgs theory. The end of the chapter has a quick review of the search for the Standard Model Higgs boson.

Chapter 3 focusses on statistical techniques, in particular those related to the search for the Higgs boson. The specific application to high energy data produced by the LHC and its predecessors is described and the meaning of the results discussed. The two statistical software tools used in this thesis, RooStats and MCLimits, are introduced and compared using a small toy experiment run by myself.

Chapter 4 goes into more detail about the two software tools, describing how the models and data are combined to produce results within the ATLAS framework. The method of adapting official ATLAS results (designed with RooStats in mind) to MCLimits is documented. The first method of MCLimits adaptation; creating a wrapper to use the same inputs as those

used to produce the RooStats workspace was entirely my work. The second method of MCLimits adaptation; extracting the models and data from the already produced RooStats workspaces was performed for one channel by Samir Ferrag. The extension to other channels and the full channel combination was also my work.

Chapter 5 deals with the extension to higher masses of the search for the Standard Model Higgs boson. It introduces the motivations for extending this search and the restrictions which had prevented it being done previously. The Complex Pole Scheme proposed by Giampiero Passarino is described and its relevance discussed. The remaining work in this chapter is all mine; implementing a reweighting mechanism to give an approximation of the Complex Pole Scheme in existing Monte Carlo samples, extension of the mechanism to account for interference effects and errors incurred in reweighting.

Chapter 1

CERN, The LHC, ATLAS and more...

1.1 Introduction

1.1.1 CERN and the Large Hadron Collider

Located on the Franco-Swiss border just outside Geneva, the European Organisation for Nuclear Research (CERN)[1] is the home of the Large Hadron Collider (LHC). The LHC was installed in a tunnel 26.3 km long and 100 m below the surface, that had previously housed the LEP[2] accelerator. The LHC is a proton-proton collider designed to be able to reach a centre of mass energy of 14 TeV and an instantaneous machine luminosity, L , of $10^{34} \text{ cm}^{-2}\text{s}^{-1}$. In high energy physics, a number of interest to an experiment is the number of events per second that can be observed, given by $N_{\text{events}} = L \times \sigma$, where σ is the cross section of the process producing the events. Also important experiment wise is the integrated luminosity \mathcal{L} : how much luminosity (or equally events) has been gathered over a period of time, δt . Integrated luminosity is measured

in inverse barns, $1b^{-1} = 10^{-24}\text{cm}^{-2}$.

The proton beams, whilst receiving most of their acceleration from the LHC, go through a chain of other accelerators before injection into the LHC, see fig(1.1). The starting point is a bottle of hydrogen where hydrogen atoms are stripped of their orbiting electrons. The remaining protons are accelerated by Linac2 and injected, at an energy of 50 MeV, into the Proton Synchrotron Booster. Once at 1.4 GeV the beam of protons is redirected into the Proton Synchrotron (PS)[3] which is responsible for pushing the energy up to 25 GeV. The penultimate stage on the journey of the protons is the Super Proton Synchrotron (SPS)[4] which increases the energy of the circulating beams to 450 GeV. From here the protons are injected into separate beampipes in the LHC in both clockwise and anticlockwise directions and accelerated to their collision energies (currently 4 TeV per beam, just over half of the design value).

The LHC ring is made up of 8 linear sectors, with access points, which are used to house the four main experiments as well as machinery for injecting, dumping, cleaning and accelerating the beams. Connecting the linear sectors are arc sections which contain the beam bending dipole magnets, see fig.(1.2).

Each beam circulates in a vacuum pipe in the centre of the cryogenically cooled magnets, which produce a magnetic field of over 8 Tesla. The super conducting Radio Frequency (RF) cavities accelerate the beam for up to twenty minutes and ensure that the proton bunches remain tightly collimated to achieve as high a luminosity as possible.

At four points on the LHC, bunches contained in the beams are squeezed before being collided and the results are recorded by the LHC experiments. The tighter the bunch is, the higher the chance of having a proton-proton collision. Fig. (1.3) shows the distribution of the mean number of interactions per bunch

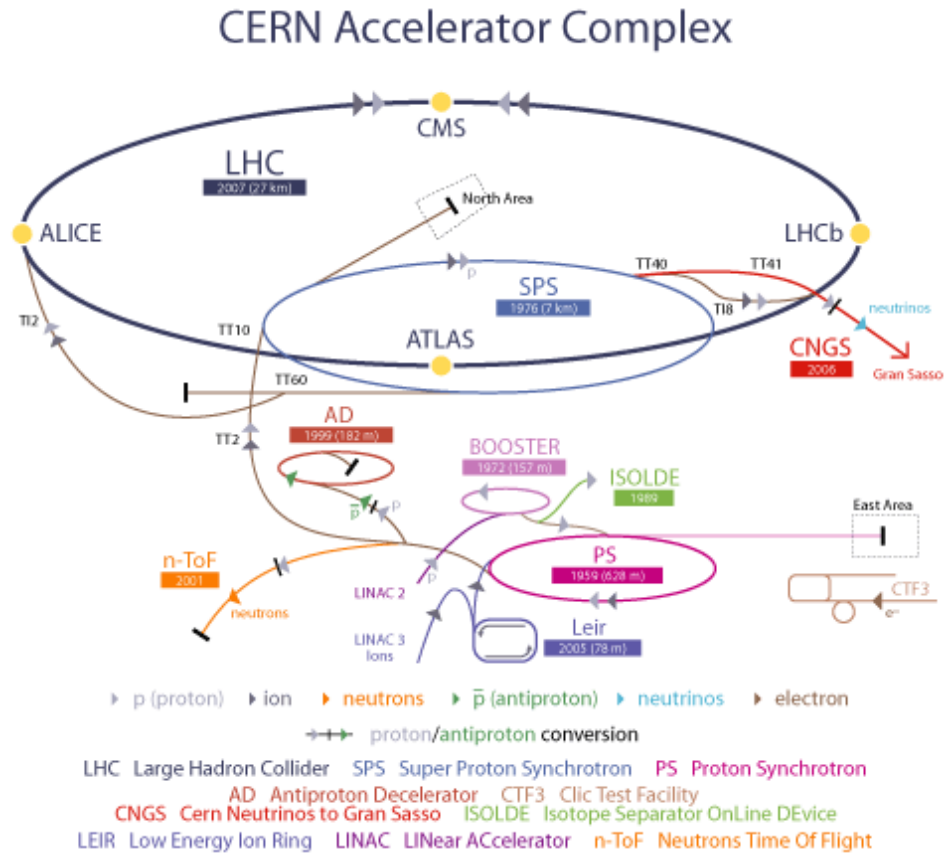


Figure 1.1: Diagram showing the accelerator complex housed at CERN (not to scale). The grey arrows show the path of protons.

crossing for 2011 and 2012 data. More than one collision per crossing is known as ‘pile up’ and adds an extra degree of complexity to physics analyses.

The four collision points of the LHC house the four main physics experiments. ATLAS (A Toroidal LHC ApparatuS)[5] and CMS (Compact Muon Solenoid)[6] are both multi-purpose detectors, designed to follow diverse physics programs over the lifetime of the LHC, complementing and cross checking each other’s results. LHCb (LHC beauty)[7] is optimised to study flavour physics and CP violation whilst ALICE (A Large Ion Collider Experiment)[8] is designed to investigate the quark gluon plasma created during heavy ion runs of the LHC.

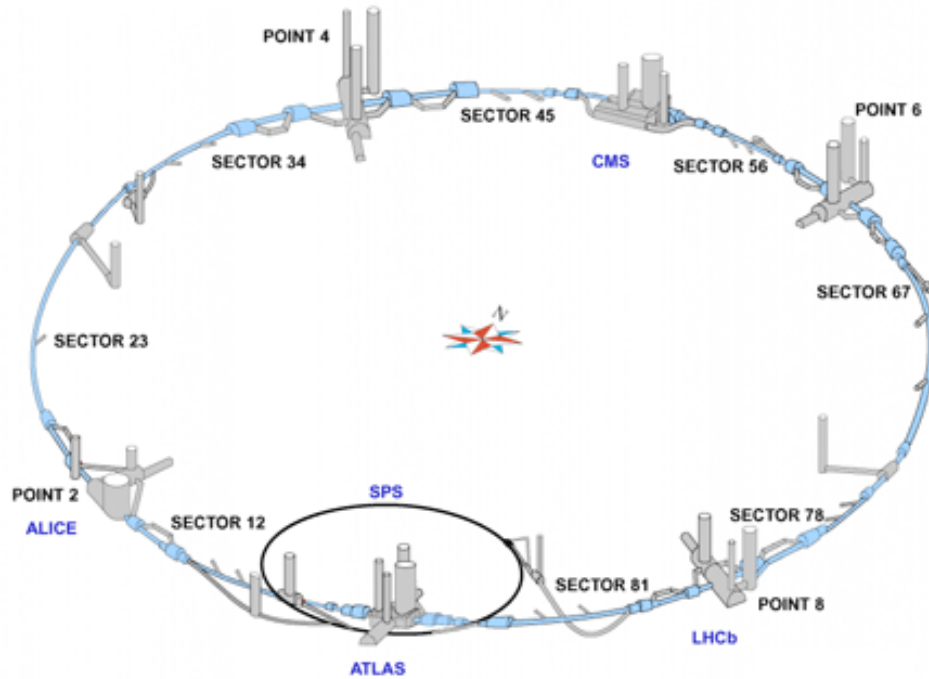


Figure 1.2: Schematic of the LHC showing positions of the main experiments and the various sectors.

1.1.2 ATLAS

The design performance of the LHC in terms of luminosity delivered to the experiments required a colossal effort in building a detector and the associated read-out systems that could deal with all of the data produced. The conditions recreated by the LHC during collisions mimic those of the universe a nanosecond after the big bang and the detectors have to be precise enough to cover the requirements behind the physics program.

ATLAS[5] is 44 m long and has a diameter of 25m, see Fig.(1.4). It is the largest particle detector, by volume, ever built. It weighs 7000 tonnes, has around 100 million electronic channels and is connected by 3000km of cables. The design is that of a barrel and two end caps. It is made up of several layers

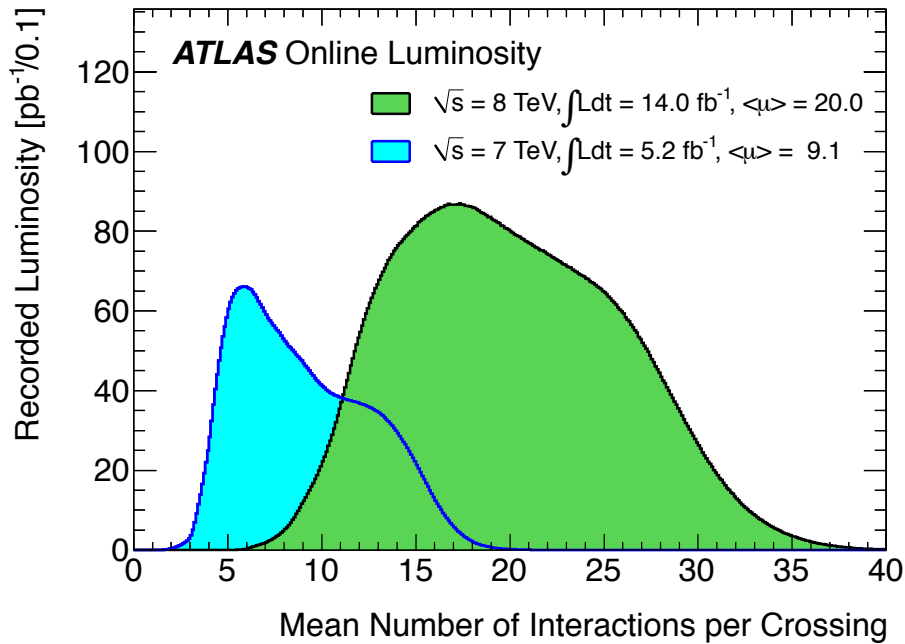


Figure 1.3: *ATLAS produced luminosity-weighted distribution of the mean number of interactions per crossing for the 2011 (blue) and 2012 (green) data (up to 17-09-12) The integrated luminosities and the mean μ values are given in the figure.[9]*

of sub-detectors to deal with triggering, particle identification and full event reconstruction. The sub-detectors can be divided into three main groups; the inner detector for tracking, calorimeters for energy reconstruction and on the outside muon chambers.

An example of the differing strengths of the sub-detectors can be seen in the identification of electrons. The ATLAS electron identification algorithm begins by looking for clusters in the electromagnetic calorimeter, that have a similar spread over $\eta - \phi$ and transverse energy to that that would be produced by the desired electrons. The selected cluster candidates are then associated to tracks reconstructed by the inner detector. To be identified as an electron candidate a cluster must be matched by a track within a sufficiently tight distance in η and ϕ .

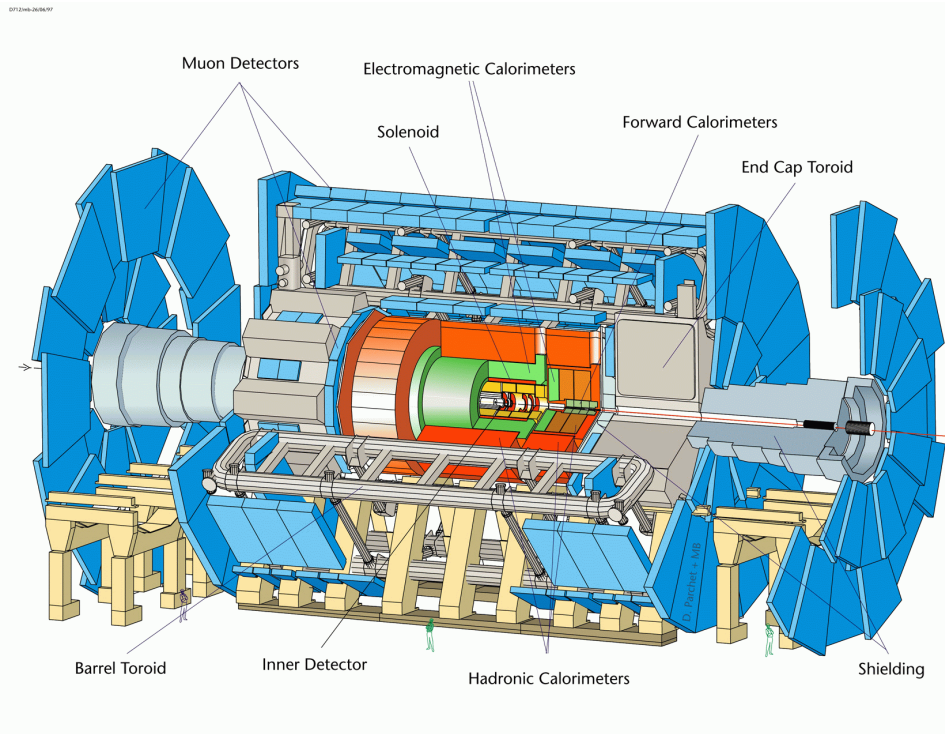


Figure 1.4: *The ATLAS Detector*

1.1.2.1 The Inner Detector

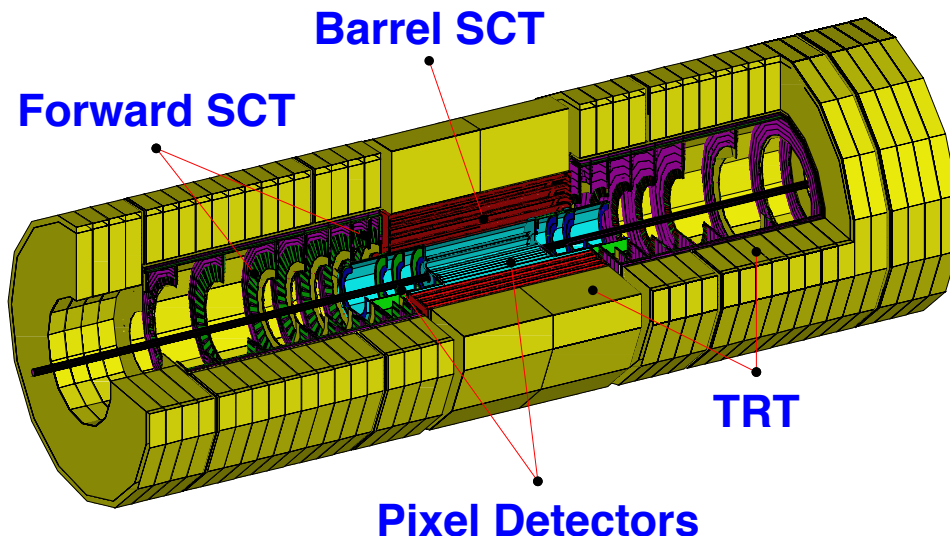


Figure 1.5: *The ATLAS Inner Detector*

The ATLAS inner detector was designed to reconstruct tracks and vertices within an event with high efficiency. It contributes, with other detectors, to electron, photon and muon recognition as well as supplying the important extra signatures for short-lived particle decay vertices[10]. Precision measurements are recorded within a pseudo-rapidity region of $|\eta| \leq 2.5$, every 50 ns, with 25 ns achievable.

The tracks are reconstructed from ‘hits’ of deposited charge left in the material layers by ionising particles as they travel outwards from the interaction point. Each subdetector is made up of barrel and end cap components, see Fig(1.5).

The inner-most subdetector is the pixel detector. It consists of three layers (in the barrel region these are at radii of 51, 89 and 123 mm from the centre of the beam pipe). The silicon (Si) pixels measure $50 \times 400 \mu\text{m}^2$. Most particles will pass through all 3 layers giving a resolution of $10/\text{mum}$ in $R - \phi$ and $115\mu\text{minz}$. The pixel detector has over 80 million read-out channels.

Next is the Semi-Conductor Tracker (SCT) which consists of silicon strips in two double cylindrical layers (in the barrel region). A double layer consists of one axial layer and another layer at a stereo angle of $40 \mu\text{rad}$. The end-cap region has the strips arranged radially, again with a second layer at an angle of $40 \mu\text{rad}$. The SCT has around 6.3 million read-out channels.

Reaching further out is the Transition Radiation Tracker (TRT), made of 4 mm diameter straw tubes, filled with a xenon based gas mixture, each with a 0.03 mm diameter gold-plated tungsten wire in the centre. In the barrel region the tubes are 144 cm long and parallel to the beam axis, whereas in the end-caps they are 39 cm long and radially arranged. Each end of a straw is read out separately. A track will produce on average 30 hits in the TRT,

enhancing pattern recognition and track momentum resolution, which provides additional information on particle type. The TRT is particularly useful in the identification of electrons as transition radiation photons can be detected in the xenon based gas inside the tubes. The TRT has around 351,000 read-out channels.

1.1.2.2 Calorimetry

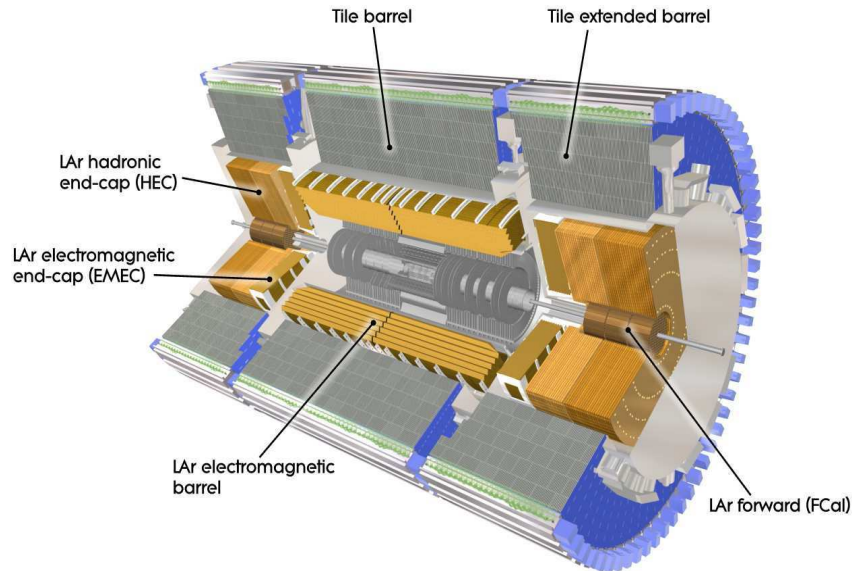


Figure 1.6: *The ATLAS calorimetry system.*

Calorimeters form an integral part of modern detectors. Sampling calorimeters, such as those in ATLAS, have alternating layers of radiative material and detectors. Particles passing through the calorimeters create showers which deposit energy. In general the thickness of the calorimetry system is enough for complete containment which allows information relating to the energy of the particle to be read out. The ATLAS calorimetry system contains two different calorimeters; the inner electromagnetic (EM) calorimeter[11] and the outer

hadronic calorimeter[12], see Fig (1.6). The EM calorimeter is used to measure the energy of electrons and photons, to build a picture of their decay. The showering of an incident electromagnetic particle in a material depends predominantly on the radiation length, χ_0 , and the Molière radius, R_M , properties of the material itself. The radiation length is the average distance travelled by an electron before it radiates (or a photon converts). The Molière radius relates the transverse scale of the electromagnetic shower to the radiation length. A smaller R_M means less diffuse jets which reduces overlap and improves event resolution.

Whilst hadrons can start to shower in the EM calorimeter it is normal for them to travel into the hadronic calorimeter before being fully absorbed. The parameter of interest for hadronic calorimeters is the interaction length, λ_0 , the average distance travelled by a hadron before it interacts via the strong force. λ_0 is typically an order of magnitude larger than χ_0 with the result that hadronic calorimeters must be thicker than EM calorimeters to achieve the same containment.

The EM calorimeter uses liquid argon (LAr) as a sampling material, as do parts of the hadronic calorimeter. The barrel region of the hadronic calorimeter uses plastic scintillating tiles as a sampling medium, giving this subdetector the nickname TileCal. Close in to the beam pipe in the endcap regions is another LAr calorimeter, known as the forward calorimeter (FCal), designed to give some information about particles, both electromagnetic and hadronic, in the very forward region of ATLAS. The ATLAS EM calorimeter is over 22 radiation lengths in the barrel and 24 in the endcap.

The LAr calorimeters contain layers of active liquid argon scintillators sandwiched between an absorbing material, all arranged in an accordion type geometry designed to give smooth coverage. The absorbing material depends

on the section of LAr detector. The EM calorimeter uses lead, whereas the endcap hadronic LAr calorimeters use copper. The FCal also uses copper as well as tungsten.

The EM calorimeter is split up into 3 regions according to their distance from the beam pipe (or from the interaction point for the endcap). The granularity of each region varies, decreasing the further away a section is. The LAr detectors have an energy resolution of approximately $\frac{10\%}{\sqrt{E}} \oplus 0.2\% \oplus K_N$ (in GeV)[13], where the first term represents the sampling term, the second the local constant and the third term constant due to noise.

The TileCal is also split into 3 longitudinal regions as well as 64 azimuthal sections for reading out, comprising over 500,000 tiles. Steel is used as an absorbing material. The granularity of the TileCal is larger than the EM calorimeter; $\Delta\eta \times \phi = 0.1 \times 0.1$, however this is sufficient to identify the various shower shapes indicative of specific decays such as τ -jets. The resolution of the TileCal is $\frac{50\%}{\sqrt{E}} \oplus 3.0\% \oplus K_N$

1.1.2.3 Muon Spectrometer

After the calorimeters, the only remaining, detectable, particles are muons. With a lifetime of 2.2×10^{-6} s they can be treated as stable particles whilst passing through the detector. The muon chambers are arranged in layers, with the aim of each muon passing through 3 tracking detectors, see Fig. (1.7). Whilst the muon chambers have a lower spatial resolution than the other detectors, they cover an area of $12,000 \text{ m}^2$ and have over 1 million readout channels. ATLAS uses 4 different types of muon chambers; Monitored Drift Tubes (MDTs) and Cathode Strip Chambers (CSCs) as tracking detectors, Resistive Plate Chambers (RPCs) as trigger chambers in the barrel region and

Thin Gap Chambers (TGCs) as endcap trigger chambers[14].

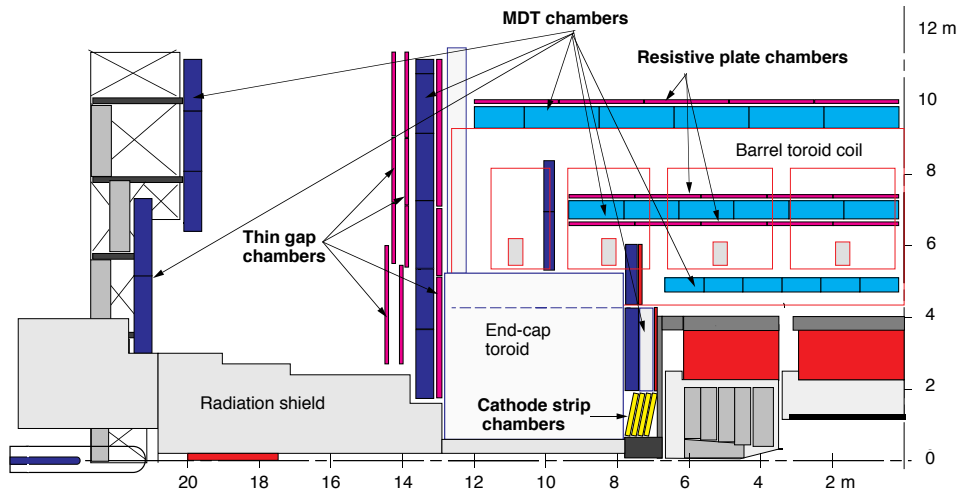


Figure 1.7: *Transverse view of the ATLAS Muon Spectrometer.*

MDTs consist of layers of 30mm diameter aluminium tubes filled with a gas mixture (90% argon, 5% methane, 4% nitrogen) each containing a $50 \mu\text{m}$ diameter tungsten-rhenium wire running down the centre. When the chamber is operating the wires are at 3270 V. A particle passing through the detector will ionise surrounding atoms in the gas. The resulting ions and electrons are accelerated by the electric field surrounding the wire, which ultimately results in a localised cascade of ionisation which is collected on the wire. The collected ionisation cascade produces an electric current proportional to the energy of the detected particle. Tube lengths vary between 70 and 630 mm according to their position in the detector.

CSCs are used in the innermost plane of the endcaps where background is greatest and high count rates are expected. Whilst operating on a similar basis to the MDTs these multiwire chambers are more adapted to their specific environment due to the shorter distance between the anode wires and cathode strips. The CSCs are symmetric cells, *i.e.* the separation between neighbouring anode wires is the same as the shortest distance between an anode wire and

the cathode, see Fig. (1.8). In the ATLAS CSCs this distance is set to 2.54 mm which gives a spatial resolution of $80 \mu\text{m}$. The gas mix in the chambers is 80% argon and 20% carbon-dioxide.

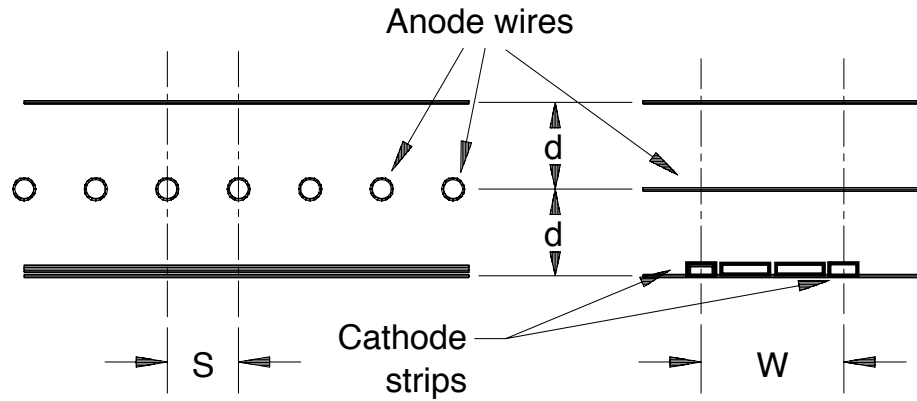


Figure 1.8: *Schematic diagram of a Cathode Strip Chamber.*

The barrel region trigger is provided by RPCs. They have excellent time resolution allowing different bunch crossings to be identified. The chambers themselves are made of two resistive plates separated by insulating spacers. The gap between the plates is filled with a gas mixture; 97% tetrafluoroethane ($C_2H_2F_4$) and 3% isobutane (C_4H_{10}). Each layer is read out by two sets of orthogonal pick up strips with one set parallel to the wires in the MDTs. This orthogonal read outs allow extra co-ordinate information as well as track bending information to be gathered.

TGCs are multiwire chambers like the CSCs except the gap between the anodes (1.8 mm) is smaller than that between an anode and the cathode (2.8 mm). The small wire-wire distance means a small drift time which is what gives the good time resolution needed for the chamber to function as a trigger. The anode wires are arranged to be parallel to the MDT wires.

Of great importance in the muon system is the alignment, so that the magnetic field can be accurately measured. The position must be known to an

accuracy of $30\mu m$, a requirement which necessitates more than 10,000 precision mounted sensors to monitor the alignment of just the MDTs.

The momentum resolution of the muon system ranges from $\sim 2.5\%$ at 20 GeV to $\sim 11\%$ at 1 TeV.

1.1.2.4 Magnet System

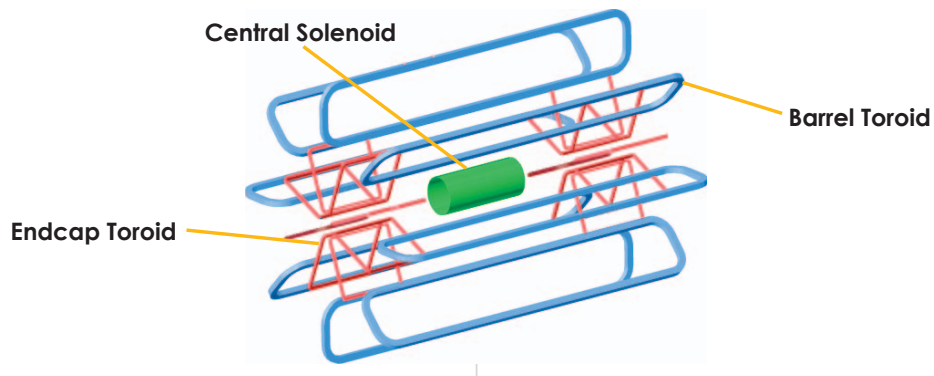


Figure 1.9: *The ATLAS Magnet system.*

The ATLAS magnet system comprises 3 toroids and a solenoid, see Fig. (1.9), and provides the magnetic field to bend the trajectory of charged particles in both the inner detector and the muon spectrometer.

The central solenoid is built into the inner detector and is aligned so that the B-field is parallel to the beam axis. It is 5.3m long, has a diameter of 2.4m, is 4.5 cm thick and weighs 5 tonnes. It contains 9km of superconducting wire and produces a magnetic field of 2 Tesla (T).

The barrel toroid magnet is one of the most distinctive features of ATLAS. It consists of 8 air-core superconducting loops orientated symmetrically around the beam axis. Each loop has its own cryostat system, operating at 4.7K. The magnetic field on the superconductor is 4T.

The two endcap toroids also contain eight loops and have similar operating specifications but they are enclosed in one casing, sharing a cryostat system. The region in the muon spectrometer where the magnetic field production is dominated by neither the barrel nor the endcap toroid is known as the transition region.

1.1.2.5 Forward Detectors

In addition to the main ATLAS subdetectors outlined above there are three additional detectors in the forward region (at increasing distances along the beam axis), to provide information about luminosity delivered to ATLAS.

First in line at 17 m from the Interaction Point (IP) is LUCID (LUminosity measurement using a Cherenkov Integrating Detector). LUCID detects inelastic proton-proton scattering per bunch crossing to provide an online measurement of relative luminosity. It comprises 170 Cherenkov tubes, approximately 1.5 m long, placed parallel to the beam pipe in a ring around it.

At 140 m from the IP, the straight section of the beam pipe has split back into two separate beam pipes. Here, between the two pipes, is the Zero Degree Calorimeter (ZDC), used to determine the centrality of heavy-ion collisions by detecting neutral particles in the very forward region. The ZDC consists of alternating layers of quartz and tungsten rods read out by photomultiplier tubes.

Furthest away, at 240 m from the IP, is ALFA (Absolute Luminosity For ATLAS). ALFA is a second system for determining luminosity which it does by monitoring elastic proton-proton collisions at small angles ($3 \mu\text{rad}$). The detector consists of scintillating fibres housed in Roman Pots which can be positioned as close as 1 mm from the beamline.

1.1.2.6 Detector Co-ordinate System

The detector co-ordinate system used by ATLAS takes the IP as the origin. From there the beam-axis defines the z direction with the $x - y$ plane perpendicular to this, x pointing to the centre of the LHC ring and y pointing upwards. In polar co-ordinates (R, θ, Φ) , the angle θ is defined as the angle from the beam axis in the $z - x$ plane and Φ , the azimuthal angle is measured in the $x - y$ plane. Due to being Lorentz invariant, pseudorapidity (η) is more normally used as a representation of the polar angle than θ . η is defined as:

$$\eta = -\ln \tan \frac{\theta}{2} \quad (1.1)$$

Transverse momentum (p_T), energy (E_T) and missing energy (E_T^{miss}) are all generally defined in the ‘transverse’ $x - y$ plane. E_T^{miss} is the term used to refer to energy transported by particles which cannot be detected, such as neutrinos. Since E_T^{miss} cannot be measured directly, it is inferred from what is not there after energy depositions in the calorimeters have been taken into account. The calculation of E_T^{miss} thus relies on the calorimeters having sufficient coverage and containment to allow only muons and neutrinos to pass. The E_T^{miss} algorithms must also take into account and gaps and dead material in the calorimeters.

A common consideration in physics analyses is the distance between two objects in the $\eta - \phi$ plane, known as ΔR and defined as;

$$\Delta R = \sqrt{\Delta\eta^2 + \Delta\phi^2} \quad (1.2)$$

The ATLAS detector has been designed to have as large an acceptance

Subdetector	η coverage
Inner detector	≤ 2.5
Electronic calorimeter	≤ 3.2
Hadronic calorimeter	≤ 4.9
Muon spectrometer	≤ 2.7
LUCID	$5.6 < \eta < 5.9$
Zero degree calorimeter	≥ 8.2

Table 1.1: *Pseudorapidity coverage of ATLAS subdetectors.*

range as feasible, to record the maximum number of particles created and to give as good a measurement of E_T^{miss} as possible.

1.1.2.7 Trigger and Data Acquisition (TDAQ).

The LHC is designed to produce 40 million bunch crossings per second. When running at design luminosity ($10^{34} \text{ cm}^{-2}\text{s}^{-1}$) there will be over 20 collisions per bunch crossing. The result of this is nearly 1 billion collisions per second, which far exceeds the rate at which events can be recorded. To get around this ATLAS uses a trigger system to filter out potentially interesting events and record only them. The trigger system in ATLAS is able to make a decision on an event very quickly. It has been designed to have an excellent efficiency and be as unbiased as possible to enable the cross sections of rare events to be measured. The system is divided into 3 components; Level 1, Level 2 and Event Filter (EF).

Level 1 is mainly a hardware trigger looking at coarse information from the muon chambers, calorimeters and tracking systems. It identifies Regions Of Interest (ROI), which contain indications of interesting signatures such as the presence of a lepton. An event passes this trigger if the specifications in

the menu held by the central trigger processor are met. The L1 trigger makes a decision within $2.5\ \mu\text{s}$ and reduces the interaction rate down from 1 GHz to 75 kHz.

Level 2 reads only the data around the ROI found by the L1 trigger, thus reducing the total amount of data to be considered. An event is rejected in 40 ms and the total rate is reduced to 2 kHz.

The EF differs from L1 and 2 trigger in that it is performed offline. Reconstruction algorithms are applied to the ROI and the decision on each takes around 4 s. The remaining 200 events per second are those that will be permanently stored for further analysis.

The trigger selections are mostly for fundamental objects (such as leptons) with high p_T thresholds. For example, channels which contain at least one electron in the final state, such as $H \rightarrow ZZ \rightarrow e\mu\nu\nu$, can trigger on an electron. A trigger stream such as $1e25i$, means that every event in the stream contains 1 electron with a p_T of at least 25 GeV, that passes the approved isolation criteria. The trigger selection in L1 locates regions of interest (RoI) in the EM calorimeter, using only a coarse granularity. L2 uses the RoI identified by L1 now with the full available granularity to consider shower shape. Initial matches with tracks are made in L2 also. Finally the events destined for the stream are identified definitively in the EF, which uses calorimeter and tracking information to refine the selection criteria.

The Data Acquisition (DAQ) system provides the interface between the ATLAS subdetectors and the trigger, and also between the different trigger levels. Each subdetector uses specific ReadOut Drivers (RODs) which create a standard form for information to then be passed from the individual sub-detector front end electronics on to the DAQ. The DAQ controls the flow of

information between the trigger levels ensuring enough data are retained to allow for the latency of the corresponding levels and handles the transfer of the final selected to data to the CERN Computer Centre. It also monitors the hardware and software connected to the data taking, allowing for configuration and control of the systems and output.

The rest of the hardware is monitored by the Detector Control System (DCS), which also handles communication between the ATLAS detector and its magnets and safety system as well as the LHC. By monitoring the behaviour of the subdetectors and comparing against standard parameters the DCS can detect unusual behaviour and even implement some adjustments where necessary.

Chapter 2

Theory

2.1 Introduction

The Standard Model (SM) of particle physics is a theory which describes a set of fundamental particles and the interactions which relate them [15]. Of the four forces recognised by modern physics; gravity, electromagnetism, the weak force and the strong force, it accounts for all except gravity. The fundamental particles can be split into 2 distinct groups according to their spin.

- Non-integer spin particles - the fermions. These particles are the constituents of matter we see around us. They can be further broken down into two groups; quarks (up, down, top, bottom, charm, strange and their respective anti-particles) and leptons (electron, electron neutrino, muon, muon neutrino, tau, tau neutrino and their respective anti-particles).
- Integer spin particles - the gauge bosons. The electromagnetic force is carried by photons (γ), the strong force by gluons and the weak force by the W^\pm and Z^0 bosons; all of which have spin 1. The Higgs boson

is predicted to have spin 0 and current experimental results support this prediction [16]

Although gravity is not described by the Standard Model, it has negligible effect on the particles at their scale. The mass of a proton is 1.672×10^{-27} kg, meaning the effect of gravity is many orders of magnitude smaller than that of the other fundamental forces.

In mathematical terms it is possible to describe the interactions of the weak, strong and electromagnetic forces as gauge theories. Electro-weak theory is a $SU(2) \times U(1)$ gauge theory which describes both electromagnetic and weak interactions. It is non-Abelian, meaning that operations within the group do not commute. Quantum ChromoDynamics (QCD) describes the interactions of the strong force and can also be represented as a non-Abelian theory with $SU(3)$ symmetry. The Standard Model combines the two sub theories to produce a $SU(3) \times SU(2) \times U(1)$ gauge theory. A feature of gauge theories like this is that the associated Lagrangian is invariant under certain symmetries, however this would predict that the weak force bosons are massless, a prediction that doesn't agree with experimental results.

Gauge invariance prohibits a mass term for the gauge bosons to be added in by hand. "Spontaneous symmetry breaking" allows for massive W^\pm and Z^0 bosons yet maintains the renormalisability of the theory, via a process known as the Higgs Mechanism. A new scalar field, called the Higgs Field, is introduced and interacts with various particles. By requiring the field to have a non-zero value in the vacuum state, the symmetry breaking required can be achieved. The Higgs field is modelled as a $SU(2)$ doublet of complex scalars. The interaction of the gauge fields with the non zero vacuum expectation give mass to the W^\pm and Z^0 bosons. The inclusion of Yukawa couplings then leads to the acquisition of mass for the fermions.

The particle associated to this field and predicted by the theory is known as the Higgs boson. After decades of searching, the 4th of July 2012 saw announcements by both ATLAS and CMS collaborations detailing the discovery of a new particle, now increasingly accepted to be the Higgs boson

2.2 Quantum Electrodynamics

Quantum Electrodynamics (QED) was the first of the relativistic quantum field theory “building blocks” which come together to make the Standard Model. The mathematical treatment of electro-magnetic (EM) interactions, developed in the 1940’s and 50’s requires the invariance of the associated Lagrangian under a local gauge transformation and results in the need for a gauge field. Photons are the quantisations of this gauge field.

If we start from the Lagrangian density for a free Dirac field ψ , used to describe the equations of motion of a system [17]:

$$\mathcal{L} = \bar{\psi}(i\gamma^\mu\partial_\mu - m)\psi. \quad (2.1)$$

For QED to be a gauge theory \mathcal{L} must be invariant under a phase transformation of the field, i.e.:

$$\psi \rightarrow e^{iQ\omega}\psi, \quad \bar{\psi} \rightarrow e^{-iQ\omega}\bar{\psi}, \quad (2.2)$$

where Q is the charge operator, ω is a real constant and thus independent of x and $\bar{\psi}$ is the conjugate field. The set of all numbers form an Abelian group (i.e. it satisfies all the normal properties of a group: closure, associativity, identity element, inverse element as well as being commutative). This group is called $U(1)$ and contains all the Unitary 1×1 matrices, where a unitary matrix is one which satisfies:

$$U^\dagger = U^{-1}, \quad (2.3)$$

where U^\dagger is the hermitian conjugate matrix. This allows us to say that the Lagrangian is invariant under global transformations. This is not enough to say that QED is a gauge field. For this we must consider cases where ω is dependent on x and show that the field is also invariant under space-time transformations.

For $\omega(x)$ the field now transforms as:

$$\delta\psi(x) = i\omega(x)Q\psi(x), \quad \delta\bar{\psi}(x) = -i\omega(x)Q\bar{\psi}(x). \quad (2.4)$$

The partial derivative between ψ and $\bar{\psi}$ means that the Lagrangian density (eqn. 2.1) is no longer invariant under these transformations. It acts on $\omega(x)$ to change the Lagrangian density by an amount $\delta\mathcal{L}$:

$$\delta\mathcal{L} = -\bar{\psi}(x)\gamma^\mu[\partial_\mu Q\omega(x)]\psi(x), \quad (2.5)$$

using the square brackets as a notation to show the limit of the application of the derivative δ_μ . Invariance can be restored by assuming the field interacts with a vector field A_μ with an interaction term $-e\bar{\psi}\gamma^\mu A_\mu Q\psi$ inserted into the Lagrangian density as follows:

$$\mathcal{L} = \bar{\psi} (i\gamma^\mu (\partial_\mu + ieQA_\mu) - m) \psi \quad (2.6)$$

A_μ , known as a gauge field, transforms as:

$$-eQA_\mu \rightarrow -eQ(A_\mu + \delta A_\mu(x)) = -eQA_\mu + Q\partial_\mu\omega(x), \quad (2.7)$$

meaning the change cancels the term shown in eqn. 2.5, restoring gauge invariance. The Lagrangian density shown in eqn. 2.6 is the fermionic part of the Lagrangian density for QED, with A_μ the photon field and e the electric charge of the fermion.

The complete quantum field theory must however incorporate a kinetic element. This will allow for the expansion of the photon field facilitating creation

and annihilation operators for photons. To avoid destroying the invariance under gauge transforms the field strength tensor is defined as;

$$F_{\mu\nu} \equiv \partial_\mu A_\nu - \partial_\nu A_\mu, \quad (2.8)$$

with the derivative acting on the photon field only. Application of the transform to this tensor results only in changes which cancel each other out. Therefore we can add the term $F_{\mu\nu}F^{\mu\nu}$, which is also Lorentz invariant, to the Lagrangian density. Furthermore if we multiply this term by the constant $-\frac{1}{4}$ the full Lagrange equations of motion match the relativistic formulation of Maxwell's equations.

The full Lagrangian density for QED is therefore:

$$\mathcal{L} = -\frac{1}{4}F_{\mu\nu}F^{\mu\nu} + \bar{\psi} (i\gamma^\mu (\partial_\mu + ieQA_\mu) - m) \psi. \quad (2.9)$$

A possible mass term for the photon could not be included with the photon field terms as it would affect the invariance of the Lagrangian, therefore one can suppose the masslessness of the photon to be a consequence of the invariance of the Lagrangian under gauge transformations.

To aid with comparisons in further sections here we will introduce the covariant derivative;

$$D_\mu \equiv \partial_\mu + ieA_\mu, \quad (2.10)$$

which will help with notation later on. It has the nice property that $D_\mu\psi$ transform in the same way as ψ . We can therefore rewrite the Lagrangian density as:

$$\mathcal{L} = -\frac{1}{4}F_{\mu\nu}F^{\mu\nu} + \bar{\psi} (i\gamma^\mu D_\mu - m) \psi. \quad (2.11)$$

2.3 Non-Abelian Gauge Theories.

To advance further we must next take the architecture used in QED and extend it to non-Abelian cases. If instead of the single fermion field we considered for QED we take n fermion fields ψ_i arranged in a multiplet, the Lagrangian density can be generalised to;

$$\mathcal{L} \equiv \bar{\psi}^i (i\gamma^\mu \partial_\mu - m)\psi_i, \quad (2.12)$$

summing over i from 1 to n . \mathcal{L} is invariant under the (space-time independent) transformation:

$$\psi \rightarrow \mathbf{U}\psi, \quad \bar{\psi} \rightarrow \bar{\psi}\mathbf{U}^\dagger, \quad (2.13)$$

here \mathbf{U} is an $n \times n$ matrix for which;

$$\mathbf{U}\mathbf{U}^\dagger = \mathbb{1}, \quad \det[\mathbf{U}] = 1. \quad (2.14)$$

The group that satisfies these conditions is called $SU(n)$, short for Special, Unitary $n \times n$ matrices, where special means that the determinant is equal to 1. An arbitrary complex $n \times n$ matrix needs $2n^2$ real parameters to define it. The n^2 constraints arising from its unitary nature and the additional $\det = 1$ constraint leaves $n^2 - 1$ real parameters.

Instead of the singular generator of $U(1)$ we now have $n^2 - 1$ generators, \mathbf{T}^a , such that;

$$\mathbf{U} = e^{-i\sum_{a=1}^{n^2-1} \omega^a \mathbf{T}^a} \equiv e^{-i\omega^a \mathbf{T}^a}. \quad (2.15)$$

We can, without loss of generality, adopt a normalisation convention such as:

$$\text{tr}(\mathbf{T}^a \mathbf{T}^b) = \frac{1}{2} \delta_{ab}, \quad (2.16)$$

which in turns leads to the signature result, namely, that two elements of $SU(2)$ do not commute, i.e.;

$$e^{-i\omega_1^a \mathbf{T}^a} e^{-i\omega_2^b \mathbf{T}^b} \neq e^{-i\omega_2^b \mathbf{T}^b} e^{-i\omega_1^a \mathbf{T}^a}, \quad (2.17)$$

hence our group is non-Abelian.

Once again, the next step is to consider a space-time dependent transformation. This time the transformed Lagrangian density is altered by;

$$\delta\mathcal{L} = \bar{\psi}\mathbf{U}^\dagger\gamma^\mu\partial_\mu\psi \quad (2.18)$$

The local symmetry can be restored by introducing a covariant derivative;

$$i\mathbf{D}_\mu = i\mathbf{I}\partial_\mu - g\mathbf{A}_\mu, \quad (2.19)$$

which is the matrix version of the one defined in eqn. 2.10 and interacts as:

$$\mathbf{D}_\mu\mathbf{U}(x)\psi(x) = \mathbf{U}(x)\mathbf{D}_\mu\psi(x). \quad (2.20)$$

Under the gauge transformation, A_μ also transforms;

$$\mathbf{A}_\mu \rightarrow \mathbf{U}\mathbf{A}_\mu\mathbf{U}^\dagger + \frac{i}{g}(\partial_\mu\mathbf{U})\mathbf{U}^\dagger, \quad (2.21)$$

meaning the Lagrangian density:

$$\mathcal{L} = \bar{\psi}(i\gamma^\mu\mathbf{D}_\mu - m)\psi, \quad (2.22)$$

is now invariant under local $SU(n)$ gauge transformations. The addition of the kinematic term is this time in the form $-\frac{1}{4}F_{\mu\nu}^a F^{a\mu\nu}$ with;

$$F_{\mu\nu}^a = \partial_\mu A_\nu^a - \partial_\nu A_\mu^a - gf^{abc}A_\mu^b A_\nu^c. \quad (2.23)$$

Unlike the QED case, here we have cross terms in the derivative of the kinematic term, which translate to a physical effect - the self interaction of the $SU(n)$ gauge bosons. The addition of a mass term for the gauge bosons would not be invariant under gauge transformations and so it is forbidden.

Quantum ChromoDynamics (QCD) is a theory describing strong interactions and is a good example of a non-Abelian gauge theory in this case with group $SU(3)$. This thesis will focus on another area of the Standard Model so we will not investigate this further, instead moving on to consider the weak interactions.

2.4 Electroweak Theory

First attempts to describe weak interactions in group theory were found to be unsatisfactory due to problems with chirality. If we return briefly to considering our elementary particles, they all have a property known as helicity which describes the particle's handedness, defined as the projection of the spin onto the direction of the momentum. For massless particles helicity is a Lorentz invariant quantity. However massive particles can be boosted into a Lorentz frame where the helicity is reversed, meaning their helicity is not Lorentz invariant. We therefore consider massive particles' chirality which is equivalent to helicity in the massless case. How a particle interacts with fields is affected by its chirality. Most particles exist in right and left-handed versions, hence we must consider them separately. For fermions we have left handed doublets and right handed singlets. So far, only left handed weak couplings have been experimentally observed.

The solution to chirality problems came with the combination of electromagnetic and weak interactions into one theory, developed by Glashow, Weinberg and Salam [18][19][20]. If we introduce a new Abelian group $U(1)_Y$, with a gauge boson B_μ and generator Y , called the hyper-charge and, due to the left-handed nature of weak interactions, say that they are described by a $SU(2)_L$ group with conserved quantity T being weak isospin we can create a group theory described by $SU(2)_L \times U(1)_Y$. Using this arrangement charge, Q can be incorporated as:

$$Q = T_3 + \frac{1}{2}Y. \quad (2.24)$$

The covariant derivative for left-handed doublets is then:

$$\mathbf{D}_\mu = \partial_\mu + ig\mathbf{T}^a W_\mu^a + ig_W \tan \theta_W Y B_\mu, \quad (2.25)$$

where W_μ^a are the three vector fields, θ_W is the weak mixing angle and g_W

is the gauge coupling strength. The covariant derivative for the right-handed singlet is given by:

$$D_\mu = \partial_\mu + ig_W \tan \theta_W Y B_\mu, \quad (2.26)$$

explicitly showing there is no term for weak interactions in the right-handed case. By superposing the fields W_μ^a and B_μ , unifying the two forces we get the physical bosons we can find experimentally, e.g.:

$$W^\pm \equiv \frac{1}{2}(W_\mu^1 \mp iW_\mu^2), \quad (2.27)$$

and:

$$\begin{pmatrix} Z_\mu \\ A_\mu \end{pmatrix} = \begin{pmatrix} \cos \theta_W & -\sin \theta_W \\ \sin \theta_W & \cos \theta_W \end{pmatrix} \cdot \begin{pmatrix} W_\mu^3 \\ B_\mu \end{pmatrix}. \quad (2.28)$$

Hence Electroweak theory is invariant under local transformations and predicts gauge bosons similar to those observed, except for the issue of mass, a possible solution for which will be outlined next.

2.5 The Higgs Mechanism

Higgs, amongst others, suggested that the W^\pm and Z bosons could attain mass through an example of spontaneous symmetry breaking. This occurs when the ground state of a system does not maintain the invariance of the system's Lagrangian. A more precise illustration can be made by considering a point mass in a potential:

$$V(\vec{r}) = \mu^2 \vec{r} \cdot \vec{r} + \lambda(\vec{r} \cdot \vec{r})^2. \quad (2.29)$$

This potential is symmetric under rotations and must have $\lambda > 0$ to have a stable ground state. For values of $\mu^2 > 0$ the minimum of the potential is at $\vec{r} = 0$, meaning the point mass falls directly to this position. However, if

$\mu^2 < 0$ the situation is more complicated. The point mass could sit at $\vec{r} = 0$ and the system would still have a symmetry, however this would not be the lowest position and therefore not the ground state. If the point mass falls in any direction from this position it will end up in the ground state but the symmetry will be broken.

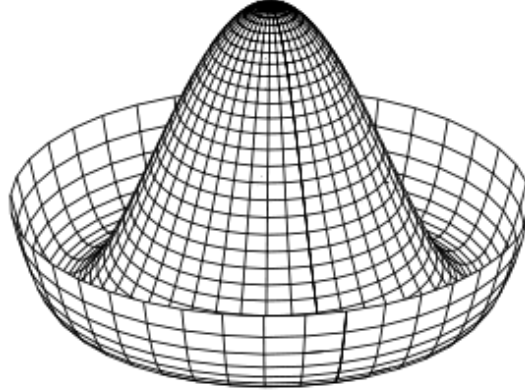


Figure 2.1: Diagram showing the potential for the situation $\mu^2 < 0$, which leads to spontaneous symmetry breaking.

Demonstrating spontaneous symmetry breaking of a gauge theory is made easier by considering a simple case first; here, a $U(1)$ in a theory of one complex scalar field, Φ . Therefore we take the Lagrangian density to be:

$$\mathcal{L} = (D_\mu \Phi)^* D^\mu \Phi - \frac{1}{4} F_{\mu\nu} F^{\mu\nu} - V(\Phi), \quad (2.30)$$

where the potential $V(\Phi)$ is:

$$V(\Phi) = \mu^2 \Phi^* \Phi + \lambda |\Phi^* \Phi|^2. \quad (2.31)$$

The Lagrangian density is invariant under the transformation:

$$\Phi \rightarrow e^{-i\omega(x)} \Phi. \quad (2.32)$$

A positive μ^2 results in a minimum at $\Phi = 0$. We call this the vacuum state, and say that operator Φ has a zero vacuum expectation value (v.e.v.). If we

were to switch the sign of μ^2 in the potential:

$$V(\Phi) = -\mu^2\Phi^*\Phi + \lambda |\Phi^*\Phi|^2, \quad (2.33)$$

the minimum at $\Phi = 0$ no longer exists, occurring instead at:

$$\Phi = e^{i\theta} \sqrt{\frac{\mu^2}{2\lambda}} \equiv e^{i\theta} \frac{\nu}{\sqrt{2}}, \quad (2.34)$$

where $0 \leq \theta \leq 2\pi$. Since all possible values break the symmetry in the same way we shall choose $\theta = 0$ as our vacuum. It should be noted that Φ has a non-zero v.e.v..

Only massless particles can have zero energy therefore we can predict their presence in this theory. We can demonstrate this mathematically by expanding Φ around its v.e.v.:

$$\Phi = \frac{e^{i\phi/\nu}}{\sqrt{2}} \left(\frac{\mu}{\sqrt{\lambda}} \right) \simeq \frac{1}{\sqrt{2}} \left(\frac{\mu}{\sqrt{\lambda}} + H + i\phi \right). \quad (2.35)$$

The fields H and ϕ have zero v.e.v.s and are the fields that will be expanded in terms of creation and annihilation operators of the particles to populate excited states. The fact that one field is represented by H is not a coincidence.

By inserting the expanded form of Φ into the potential we get:

$$V = \mu^2 H^2 + \mu\sqrt{\lambda}(H^3 + \phi^2 H) + \frac{\lambda}{4}(H^4 + \phi^4 + 2H^2\phi^2) + \frac{\mu^4}{4\lambda}. \quad (2.36)$$

The H field comes with a mass term $\mu^2 H^2 \equiv M_H/2H^2$ however there is no mass term for the ϕ field. The boson associated to the ϕ field is a massless particle known as the ‘‘Goldstone Boson’’[21].

Next we consider the kinetic terms, again substituting our expanded Φ this time into $(D_\mu\Phi)^*D^\mu\phi$ giving:

$$\begin{aligned} (D_\mu\Phi)^*D^\mu\phi &= \frac{1}{2}\partial_\mu H\partial^\mu H + \frac{1}{2}\partial_\mu\phi\partial^\mu\phi + \frac{1}{2}g^2\nu^2 A_\mu A^\mu + \frac{1}{2}g^2 A_\mu A^\mu (H^2 + \phi^2) \\ &\quad - gA_\mu(\phi\partial_\mu H - H\partial_\mu\phi) + g\nu A_\mu\partial^\mu\phi + g^2 A_\mu A^\mu H. \end{aligned} \quad (2.37)$$

From this we can see that the gauge boson has acquired a mass term given by $(1/2)g^2\nu^2 A_\mu A^\mu \equiv (1/2)M_A^2 A_\mu A^\mu$. We can also see that there is a coupling of the gauge field to the H -field;

$$g^2\nu A_\mu A^\mu H = gM_A A_\mu A^\mu H. \quad (2.38)$$

.

Next we return to the massless Goldstone boson proposed earlier as a result of a global transformation. If we instead consider a local transformation the choice of which vacuum is the true vacuum becomes equivalent to choosing a gauge. This means that the “flat” transition performed by the bosons can be into states which are not consistent with the original gauge choice, meaning the bosons are unphysical, and are often referred to as ghosts. However the degrees of freedom represented by the ghosts do not disappear, instead they provide the third degree of freedom for the gauge bosons, meaning that the gauge bosons become massive. Because of this inheritance, the Goldstone ghosts are said to be absorbed by the gauge bosons. The real Higgs mechanism contains four Goldstone bosons since the complex scalar field Φ is a doublet. The four Goldstone masses are absorbed by the W^\pm and Z bosons, as well as the massive particle introduced in eqn. 2.36, more commonly known as the Higgs boson [22][23][24][25].

2.6 The Search for the Higgs Boson

Whilst the Standard Model predicts the existence of the Higgs Boson it does not predict its mass. This could prove problematic for those wishing to search for it. Luckily both theory and experiments have provided limits on the probable mass range [26].

Unitarity The Standard Model predicts the massive gauge bosons to self interact. If a scalar mass field was not introduced, the scattering amplitude of the vector bosons above a certain centre of mass energy would occur with a probability greater than 1. This limit is around 1 TeV, which should be the upper limit that will be explored by the LHC.

Triviality and Vacuum Stability We must also consider the self interaction of the Higgs Boson, represented by its coupling constant λ . Vacuum stability requires that λ is positive which can be used for a lower bound. Triviality requires that λ must not reach a Landau Pole (the energy at which the self coupling becomes infinite). By setting an upper bound on this we can provide an upper bound for the Higgs Boson mass. If we choose the Planck scale ($\sim 10^{19}$ GeV), the Higgs mass would be in the range $130\text{GeV} \leq m_H \leq 190\text{GeV}$. More generally, the cut-off is set to the electroweak scale (~ 1 TeV) which gives looser limits of $50\text{GeV} \leq m_H \leq 800\text{GeV}$.

Precision Electroweak Tests Hints as to the mass of the Higgs boson can be deduced from measurements of observables of other particles with which it interacts. The LEP Electroweak Working Group (LEP EWWG), combines precision measurements from several experiments and uses these to make predictions on which mass is most likely, see figs. (2.2) and (2.3).

Direct Experimental Measurements The LEP experiments excluded a SM Higgs boson at 95% confidence level up to 114.5 GeV [27]. The Tevatron accelerator at Fermilab in the United States has ceased to operate but analysis of the data collected by its experiments continues for the time being. The combined results from the Tevatron in July 2011 had excluded the mass range $156\text{ GeV} < m_H < 177\text{ GeV}$ [28] at 95% confidence level. The end of 2011 saw the LHC's two multi-purpose detectors releasing their latest Higgs result. ATLAS excluded (at 95% confidence level) 112.7 GeV to 115.5 GeV, 131 GeV

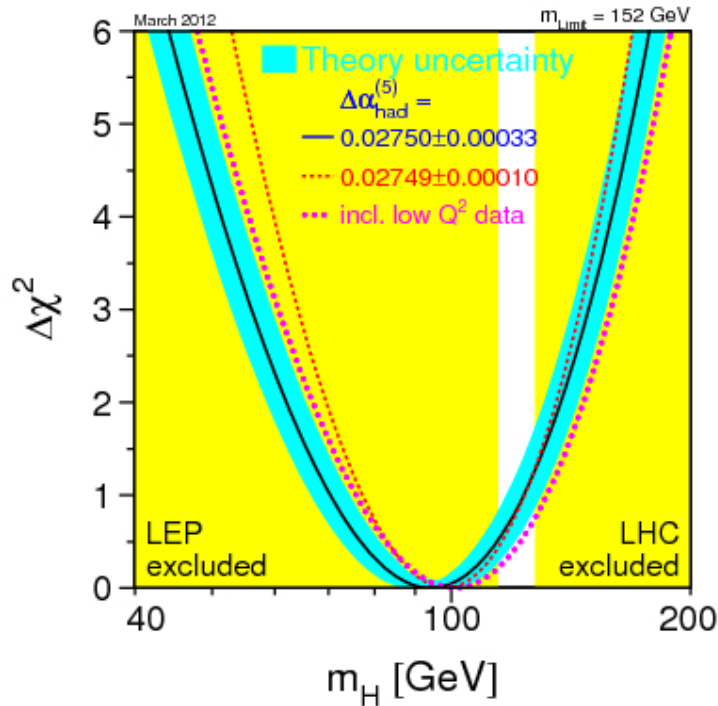


Figure 2.2: LEP EWWG produced “blue-band” plot showing a $\Delta\chi^2$ fit to precision electroweak measurements. The yellow blocks show regions excluded by experiments (results up to March 2012) [29].

to 237 GeV and 251 GeV to 468 GeV and CMS announced exclusions in the range 127 GeV to 600 GeV. Both experiments saw more events than expected elsewhere: ATLAS at $m_H \simeq 126$ GeV and CMS at $m_H \simeq 124$ GeV. Neither excess of events (with significances, after accounting for the “Look Elsewhere Effect” (see chapter 3.2.3) of 2.3 and 1.9 σ respectively) was large enough to be able to claim anything more than having seen slightly more events than one would expect but it was still treated, cautiously, as an exciting hint.

The 2012 LHC run increased the centre-of-mass energy to 8 TeV. The full 7 TeV dataset analyses were first shown at the Rencontres de Moriond conference in March 2012. The ATLAS Higgs combination with all channels using between

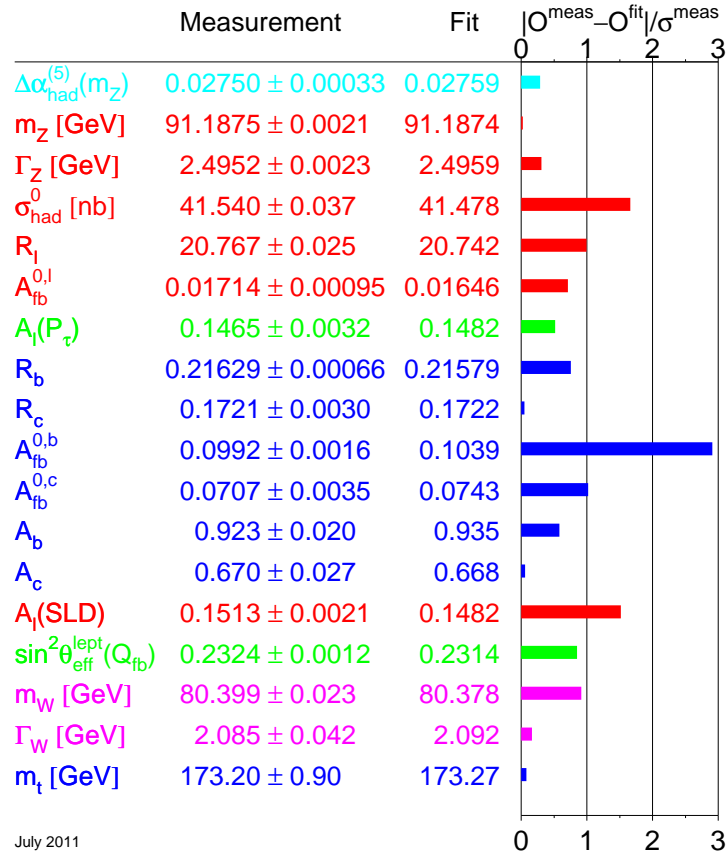


Figure 2.3: Parameter values and uncertainties used in the “blue-band” plot.

4.6 and 4.9 fb^{-1} integrated luminosity of 7 TeV data was released a few weeks after this conference. Excluded at 95% confidence level were the ranges: 110.0 to 117.5, 118.5 to 122.5, and 129 to 539 GeV. There was still a notable excess of events at 126 GeV, which had a local significance of 2.5σ .

July 2nd 2012 saw Fermilab announcing the most recent results from the Tevatron experiments, see fig. (2.5)[30]. Their results combined up to 10fb^{-1}

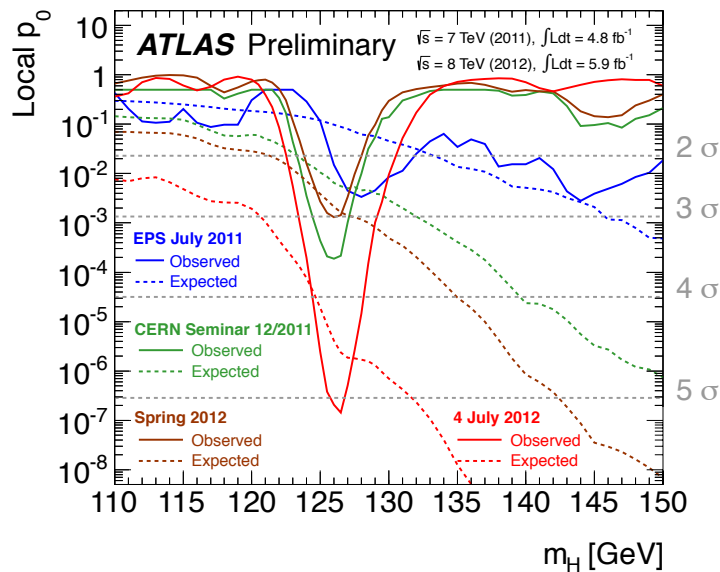


Figure 2.4: Plot showing the local significance of the excess of events at $m_H = 126.5$ GeV for several iterations of the Higgs channel combination, each time including an increased amount of data as it became available for analysis.

of luminosity at a centre of mass energy of 1.96 TeV. Using this data they excluded at 95% confidence level a Higgs boson with a mass of 100 to 103 GeV and 147 to 180 GeV. They observed an excess of events in the mass range 115 to 140 GeV meaning the limits they were able to set were not as stringent as they had expected them to be. At $m_H = 120$ GeV they observed an excess of events corresponding to a significance of 2.5σ when taking into account the look elsewhere effect.

July 4th 2012, was the date of an announcement by both the ATLAS and CMS collaborations about their searches for the Higgs boson. They both showed results which combined different Higgs decay channels using 7 and 8 TeV data. The range expected to be excluded at 95% confidence by ATLAS, using this dataset, was from 110 to 590 GeV. In fact the ranges were 110-122.7 GeV and 129.7-560 GeV. The previously observed excess of events still

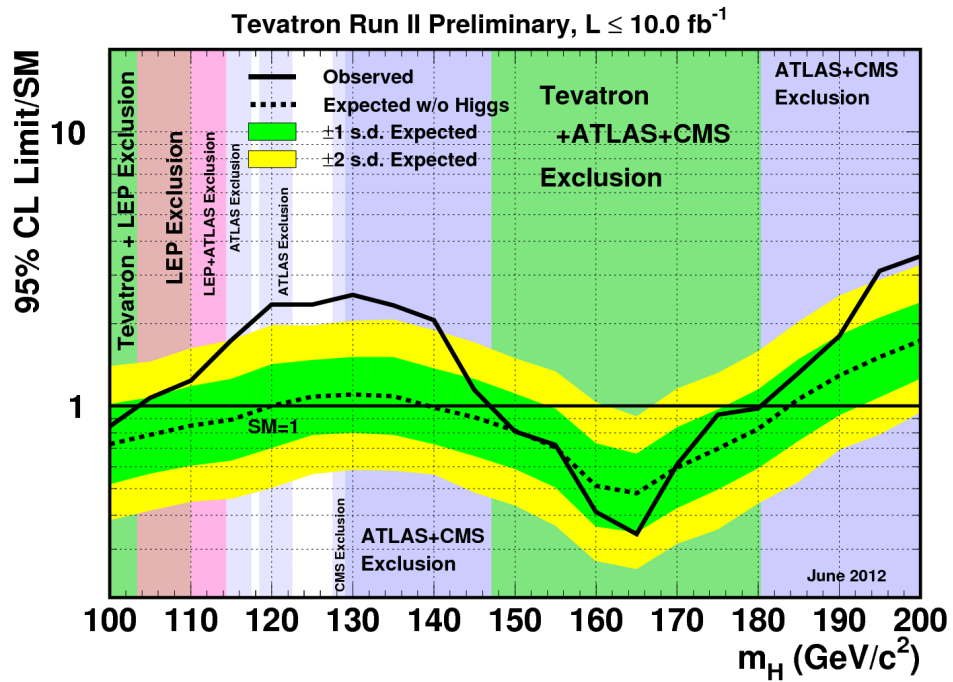


Figure 2.5: Observed and expected 95% C.L. upper limits on the ratios to the SM cross-section as a function of the Higgs boson mass for combined $D0$ and CDF analyses.

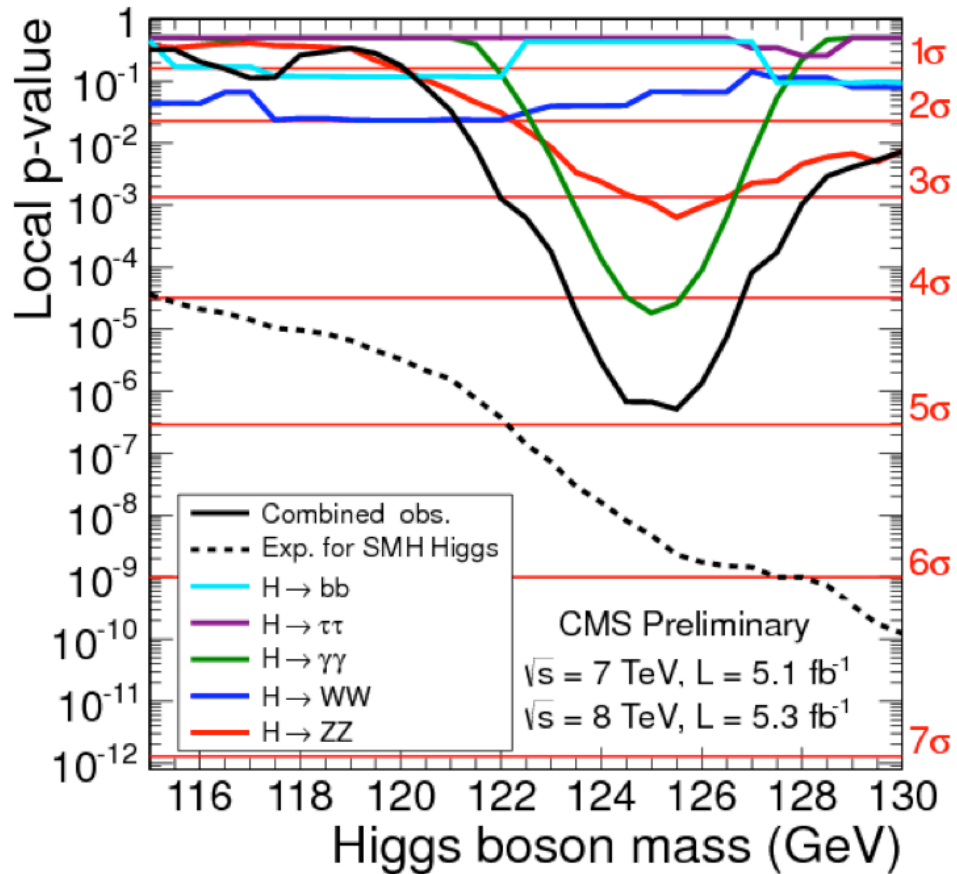


Figure 2.6: The observed probability that the background-only hypothesis yields the same excess of events as seen in the data as a function of Higgs mass for the 5 channels considered. The solid black line is the combined probability. The dotted black line shows the equivalent expected in the assumption of a signal.

remained. The maximum was located at 126.5 GeV and had a local significance just over 5σ allowing the ATLAS collaboration to, cautiously, announce the observation of a new particle, see fig. (2.4) for the time evolution of the significance. The observation was shared between ATLAS and CMS. Likewise, in the absence of a signal, CMS could have expected to completely exclude the mass range 110 to 600 GeV. The range 122.5 to 127 GeV was not excluded due to an excess of events in three of the five channels analysed, with a statistical significance of 4.9σ , see fig. (2.6). Both experiments emphasized that more investigations of the particle would be needed, which would require more LHC data, before any firm statements on the nature of the particle could be made.

2.7 Production and Decay of the Higgs Boson at the LHC

There are four main Higgs boson production mechanisms for collisions at the LHC:

- gluon gluon Fusion (ggF)
- Vector Boson Fusion (VBF)
- associated production with a vector boson (Higgsstrahlung)
- associated production with $t\bar{t}$, a top pair.

whose Feynman diagrams are shown in fig. (2.7) and respective production cross-sections as a function of Higgs mass in fig. (2.8).

The decay of the Higgs boson depends on its mass. See fig. (2.9) and since its coupling is proportional to its mass it decays preferentially to the highest

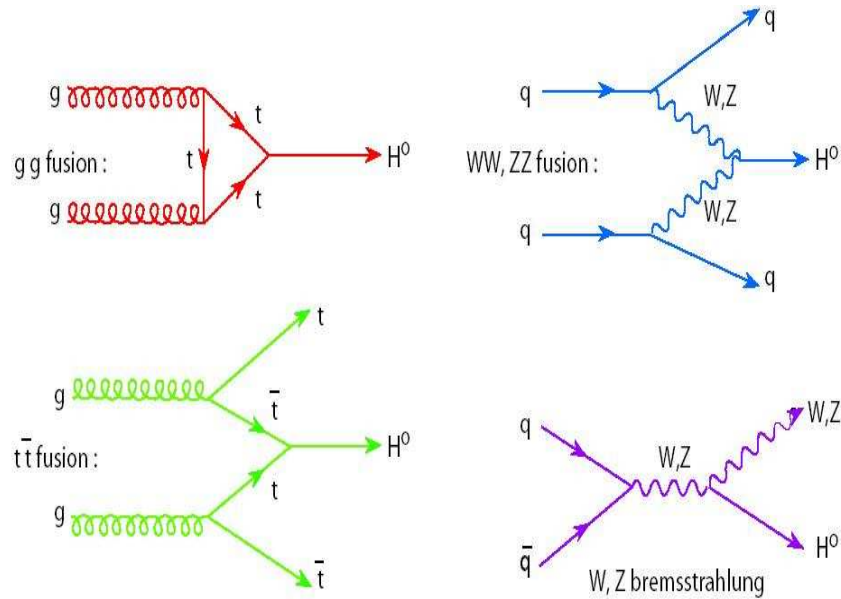


Figure 2.7: Feynman diagrams for the four major Higgs boson production mechanisms at the LHC.

mass particles available within the operating energy scale. This naturally suggests a division of the mass range when considering which channels to use for the search.

Low Mass Range ($m_H < 130\text{GeV}$) Whilst the prominent decay here is to $b\bar{b}$ this channel suffers from the massive QCD backgrounds found in hadron colliders. Nevertheless, many innovative ways are being developed to try and increase the significance. As of now, only the $VH \rightarrow b\bar{b}$ channels have ever been included in a combination of ATLAS Higgs channel searches. $H \rightarrow gg$ and $H \rightarrow c\bar{c}$ are not studied at ATLAS because their hadronic final states would be obscured by $b\bar{b}$ jets and no tagging algorithms exist for gluons or charm jets unlike for b -jets. The two main low-mass specific search channels are $H \rightarrow \gamma\gamma$ and $H \rightarrow \tau^+\tau^-$. Whilst they both have lower branching fractions than $H \rightarrow b\bar{b}$ their signal to background ratios are superior. $H \rightarrow \gamma\gamma$ requires

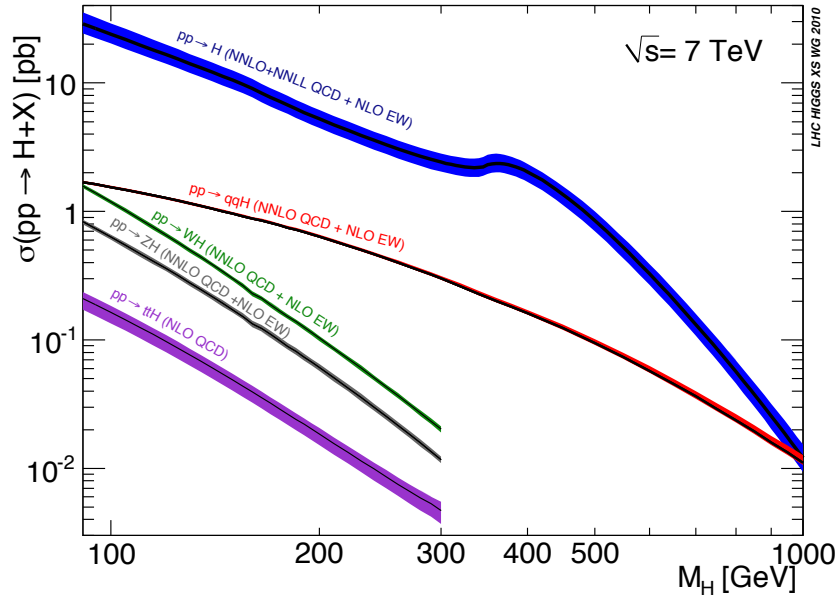


Figure 2.8: Production cross-sections for the Higgs boson over a range of possible masses[29].

excellent energy and angular resolution but results in a very clean peak for a signal on top of the irreducible $\gamma\gamma$ background. $H \rightarrow \tau^+\tau^-$ decays are studied by splitting them into 3 sub-channels; both taus decaying leptonically, one tau decaying leptonically, the other hadronically, and finally where both taus decay hadronically.

Mid-range Mass ($130\text{GeV} \leq m_H < 200\text{GeV}$) As the proposed Higgs boson mass increases first the WW and then ZZ productions “switch on” meaning they become energetically possible and become more and more prevalent taking over from $b\bar{b}$. The so called Golden Channel $H \rightarrow ZZ \rightarrow 4l$ is important both here and at higher masses. Since the decay products are all leptons, QCD backgrounds cause less problems and the mass resolution is much better than channels that include neutrinos in the final decay products such as the final channel used for searches in this mass range $H \rightarrow WW^{(*)} \rightarrow l\nu l\nu$.

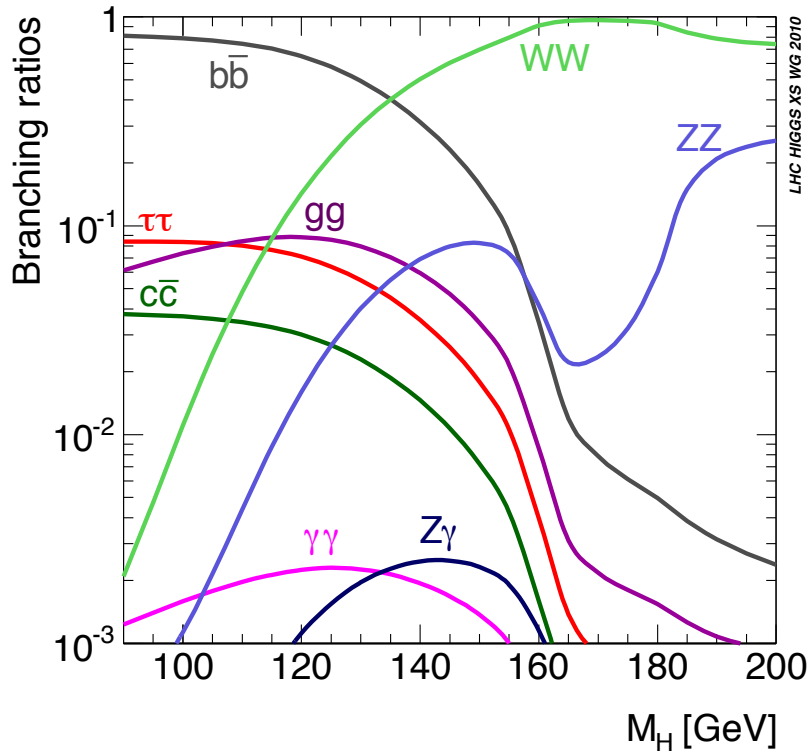


Figure 2.9: Branching ratios of Higgs boson decay products for low to mid range Higgs masses[29].

High Mass Range ($m_H > 200\text{GeV}$) This range is still covered by the golden channel and for a large proportion of this range the signal to background ratio is very favourable. However at very high masses ($> 800\text{GeV}$) the $4l$ channel rate drops meaning the other high mass channels become ever more important. The other WW channel is $H \rightarrow WW \rightarrow lvqq$ and the other ZZ channels are $H \rightarrow ZZ \rightarrow 2l2\nu$ and $H \rightarrow ZZ \rightarrow 2l2q$.

The most exhaustive search comes from combining the results from all the available channels for as much data as possible, see fig.(2.10). This is not a trivial task and requires advanced statistical software tools and techniques. The comparison of the official ATLAS procedure for combination with an alternative procedure based on and adapted from that used by the Tevatron

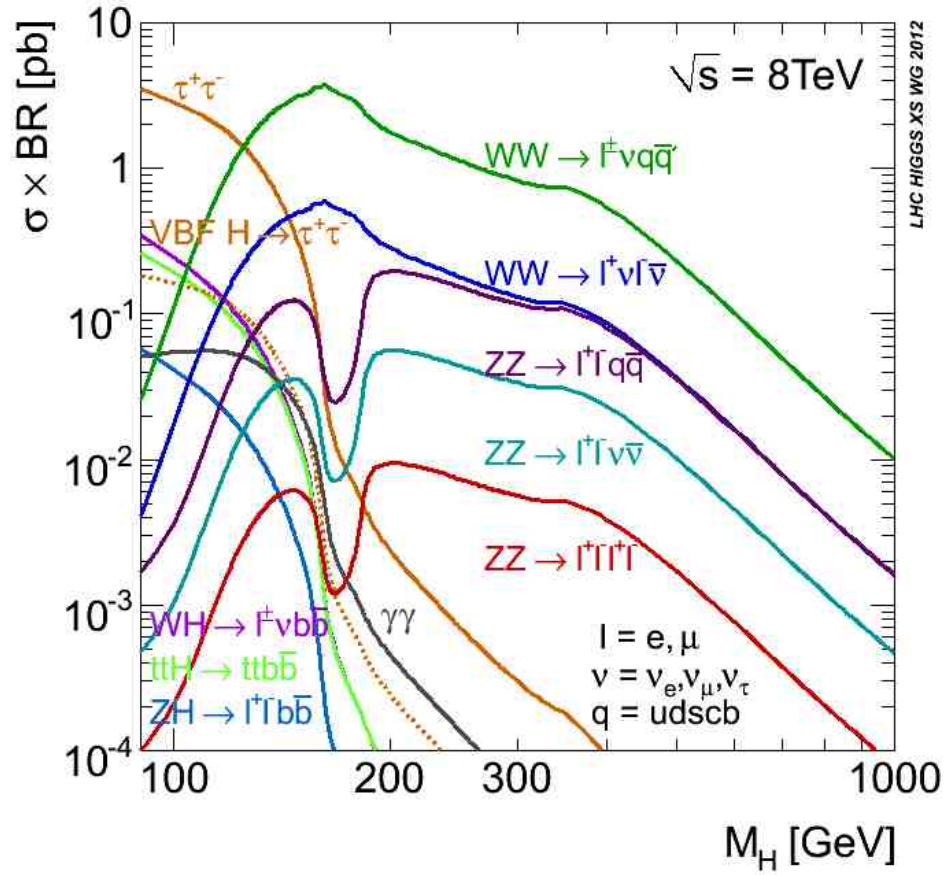


Figure 2.10: Standard Model Higgs boson production cross-section times branching ratio at 8 TeV centre of mass energy[29].

experiments forms the basis of this thesis.

Chapter 3

Analysis Techniques - Statistics

3.1 Introduction.

The Oxford English Dictionary [33] defines **Statistics** as “the practice or science of collecting and analysing numerical data in large quantities, especially for the purpose of inferring proportions in a whole from those in a representative sample”. In high energy particle physics we use statistics to analyse and interpret the data collected by our experiments, matching our observations to predictions made by theorists. Statistics tends to come in two main flavours; frequentist and Bayesian. Both methods start with the consideration of probability, i.e. the likelihood an outcome will occur. If we declare a set S and consider it as a sample space with a number of elements k . S can have a number of subsets A which are assigned probabilities $P(A)$ which are real numbers defined by the axioms;

- $\forall A \subset S, P(A) \geq 0$
- for any A, B that are disjoint, $P(A \cup B) = P(A) + P(B)$

- $P(S) = 1$

Unfortunately, for many of the variables we would like to study, their probabilities depend on other variables. So a more useful construct is the conditional probability, $P(A | B)$ (probability of A given B). This leads us to a definition of probability known as Bayes' theorem;

$$P(A | B) = \frac{P(B | A)P(A)}{P(B)}. \quad (3.1)$$

The split between the two methods occurs in how we interpret this. Frequentists see probability as a relative frequency. In terms of science this means repeating an experiment to be able to gauge the fraction of time an outcome occurs and translating this to an infinite situation, which is best represented as;

$$P(A) = \lim_{x \rightarrow \infty} \frac{\text{number of occurrences of outcome } A \text{ in } n \text{ measurements}}{n}. \quad (3.2)$$

The Bayesian interpretation is to see this as a degree of belief. This degree of belief is reconsidered with each available boolean proposition. For this reason Bayesian calculations start with a "prior", an initial probability which is updated with each bit of new, relevant, data. Whilst the two interpretations may seem radically different, their application to mature, robust analyses often produce similar results.

3.2 Hypothesis Testing

When searching for evidence of a new particle, say a Higgs boson, we have two different hypotheses. One, normally referred to as H_1 , allows the presence of a signal and is known as the test hypothesis. H_0 is the conflicting hypothe-

sis, known as the null hypothesis, and describes the situation for which only background is present.

3.2.1 Log Likelihood Ratio

We wish to assess the probabilities associated to each hypothesis with respect to the data taken. According to the Neyman-Pearson lemma, the most powerful way of doing this is by considering the Likelihood Ratio. First we must consider what we mean by likelihood. A likelihood function is a function of the parameters of a statistical model. The function will tell us the likelihood of a set of parameter values according to the data set for which it is calculated. For a binned analysis the likelihood function is the product of Poisson probabilities for all bins [34]:

$$\mathcal{L}(\mu, \theta) = \prod_{j=1}^N \frac{(\mu s_j + b_j)^{n_j}}{n_j!} e^{-(\mu s_j + b_j)} \prod_{k=1}^M \frac{u_k^{m_k}}{m_k!} e^{-u_k}, \quad (3.3)$$

where the parameter μ determines the strength of the signal process, for the background only process $\mu = 0$ and $\mu = 1$ is the nominal signal hypothesis; θ represents the nuisance parameters (variables which are not known precisely, and which are not the parameter of interest but are still part of the model); s_i and b_i are the mean numbers of entries in the i^{th} bin from signal and background events respectively; n_j is the total number of entries in the j^{th} bin and m_k is the number of entries in the k^{th} bin of the related control sample histogram. $u_k^{m_k}$ corresponds to the expectation value of m_k depending on the parameters θ .

The likelihood ratio, Q , is therefore a ratio of the likelihoods for two opposing hypotheses, H_0 and H_1 ;

$$Q = \frac{\mathcal{L}(\text{data} | H_1)}{\mathcal{L}(\text{data} | H_0)} = \frac{\mathcal{L}(\text{data} | \mu s + b)}{\mathcal{L}(\text{data} | \hat{\mu} s + b)}. \quad (3.4)$$

Here $\hat{\mu}$ corresponds to the value of μ that maximises the likelihood.

To enable decisions to be more easily made on whether to accept or reject a hypothesis the log likelihood ratio is more normally used;

$$q_{\mu} = -2 \ln Q. \quad (3.5)$$

q_{μ} is known as the test statistic and compresses all the signal versus background discriminating information into one number.

A value of the test statistic can be calculated, under the assumption of the *signal+background* hypothesis. With simulated data, this can be repeated many times to account for the Poisson probabilities of unknown parameters, allowing us to construct a *probability density function* (pdf) for the test statistic, see the H_1 distribution in fig. (3.1). This process is said to be “tossing” toy pseudo-observations.

The constructed pdf and the observed data test statistic can then be used to calculate a p-value denoted as CL_{s+b} , which is the probability for the actual value of the test statistic measured from the data q^{data} to be as or less compatible with the H_1 hypothesis. Fig. (3.1) shows a vertical line representing q^{data} . The area between this line and the H_1 distribution, shown in green, is equivalent to CL_{s+b} .

If $CL_{s+b} = 0.05$ the signal is said to be excluded at 95% Confidence Level. The procedure outlined above is the standard frequentist definition of a Confidence Level. Care must be taken with this for situations where an experiment is not sensitive. In these conditions a downward fluctuation of the background could result in the incorrect exclusion of a signal.

The sensitivity of a test can be visualised by, again, referring to fig. (3.1): If we consider the two pdf distributions, of the H_0 and H_1 hypotheses, there

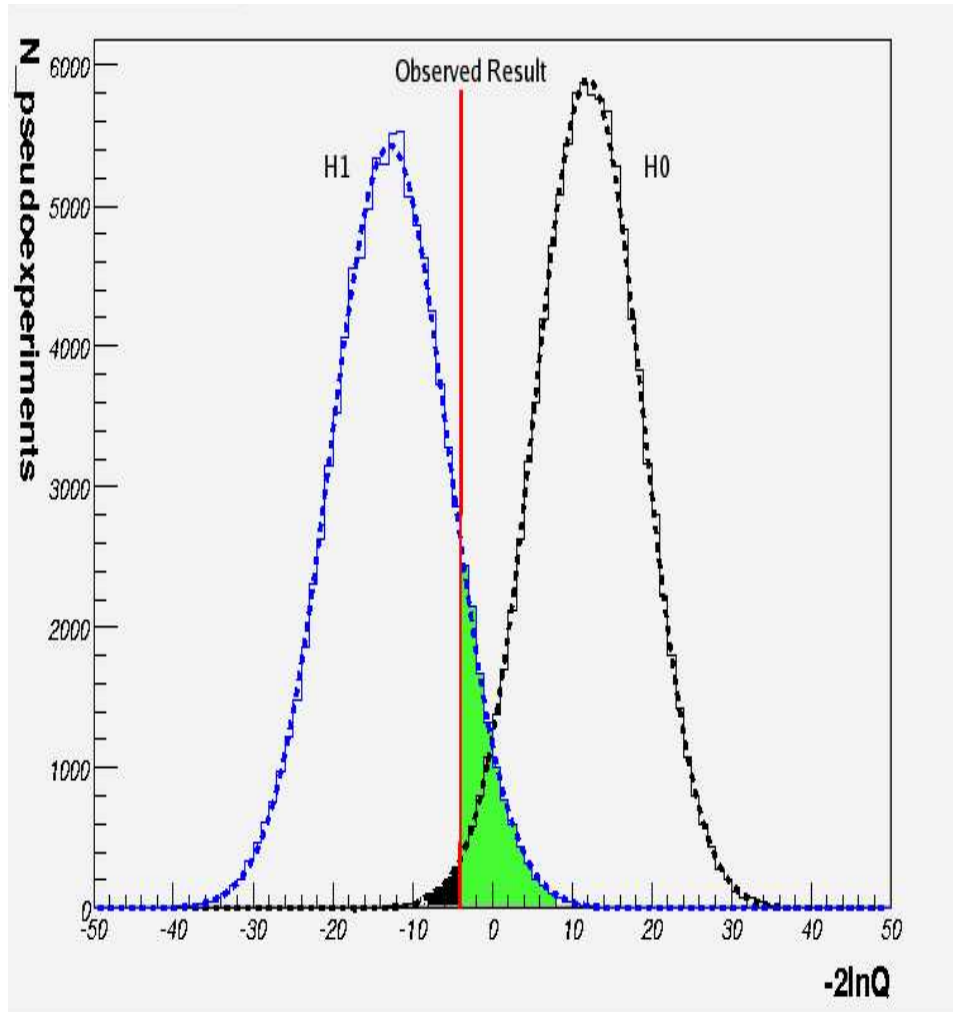


Figure 3.1: Sample plot taken from [35] showing the pdf for the test statistic under the two hypotheses, a line representing the observed test statistic, and the area representing CL_{s+b}

is a certain amount of overlap between these two distributions. If we were to translate one of the distributions, say, H_1 , along the x -axis the overlapping area would either increase or decrease according to whether the translation was in the positive or negative direction. Clearly, the smaller the overlapping area is, the easier it is to say if an observed data test statistic is more compatible with one hypothesis as opposed to the other. Therefore, the more distinct the two hypothesis distributions are, the more sensitive the experiment is.

To avoid excluding signals for which there is insufficient sensitivity, the modified frequentist method also considers $1 - \text{CL}_b$ represented by the black filled area, to the left of the observed result line in fig. (3.1). $1 - \text{CL}_b$ is the probability of observing a signal+background like event without the presence of a signal, i.e. the probability of an upward fluctuation in the background mimicking a signal. To this end, the quantity used for exclusion of signal is [36];

$$\text{CL}_s = \frac{\text{CL}_{s+b}}{\text{CL}_b} \quad (3.6)$$

The use of CL_s prevents insensitive exclusion however it is not a perfect method. By its definition it is always greater than CL_{s+b} , even in regions where the sensitivity of the experiment would not be an issue, meaning that results are conservative. In the high energy physics community a conservative method is preferred to excluding something wrongly.

The modified frequentist method was the technique chosen for Higgs search results for LEP, Tevatron and now LHC experiments. Differences between the three occur in the test statistic and the treatment of systematic uncertainties. They will be considered separately in the coming sections.

In the next sections the following nomenclature will be used; μ is the parameter of interest, known as the signal strength parameter, θ is the full suite of nuisance parameters (e.g. jet energy scale), the uncertainties on the signal and background rates are therefore $s(\theta)$ and $b(\theta)$. A set of “prior” pdfs for the nuisance parameters can be constructed, $\rho(\theta | \tilde{\theta})$, where $\tilde{\theta}$ is the “nominal” value of the nuisance parameters.

3.2.1.1 LEP Method

For LEP results, the test statistic was set to be:

$$q_\mu = -2 \ln \frac{\mathcal{L}(\text{data} \mid \mu = 1, \theta)}{\mathcal{L}(\text{data} \mid \mu = 0, \theta)} \quad (3.7)$$

Each pseudo-data set was generated after drawing random numbers from the $\rho(\theta \mid \tilde{\theta})$ distributions. This technique was first introduced to the field by Cousins and Highland [37]. The explicitly Bayesian treatment of the nuisance parameters has led to this method being known as hybrid Bayesian-frequentist.

3.2.1.2 Tevatron Method

The Tevatron experiments retained the hybrid Bayesian-frequentist technique for “tossing” pseudo-data however they altered the test statistic slightly with respect to that used by the LEP experiments [38]. The likelihood functions used in the likelihood ratio were extended to include the nuisance parameter pdfs:

$$\mathcal{L}(\text{data} \mid \mu, \theta) = \text{Poisson}(\text{data} \mid \mu s(\theta) + b(\theta)) \cdot \rho(\theta \mid \tilde{\theta}). \quad (3.8)$$

Before calculating the ratio both the numerator and denominator of the test statistic are maximised with respect to the nuisance parameters. This pre-maximised test statistic is then written as:

$$q_\mu = -2 \ln \frac{\mathcal{L}(\text{data} \mid \mu, \hat{\theta}_\mu)}{\mathcal{L}(\text{data} \mid 0, \hat{\theta}_0)}, \quad (3.9)$$

where $\hat{\theta}_\mu$ and $\hat{\theta}_0$ are the maximum likelihood estimators of θ for the H_1 and H_0 hypothesis respectively. In this case the systematic errors are “profiled”, and the test statistic is known as a Profile Likelihood.

3.2.1.3 LHC method

The LHC experiments also adopt profiling for the systematic errors however the test statistic definition differs from the Tevatron's in that the signal strength parameter in the denominator can be non-zero;

$$\tilde{q}_\mu = -2 \ln \frac{\mathcal{L}(\text{data} \mid \mu, \hat{\theta}_\mu)}{\mathcal{L}(\text{data} \mid \hat{\mu}, \hat{\theta})}, \quad \text{with a constraint } 0 \leq \hat{\mu} \leq \mu \quad (3.10)$$

where $\hat{\mu}$ and $\hat{\theta}$ are estimated using the global maximum of the likelihood. This format allows a pre-fit stage of the model to be performed, leading to a median, which in conjunction with the variance can replace having to fit the model for each toy experiment. $\hat{\theta}_\mu$ is the maximum likelihood estimator for a fixed μ . The lower constraint on μ requires a positive signal for physical reasons, whilst the upper constraint means that data fluctuations giving $\mu > \hat{\mu}$ are not taken as evidence against a signal hypothesis, just a signal with strength μ . Internal ATLAS tests performed by the statistics group have found that the Tevatron and LHC versions of CL_s , although constructed differently give almost identical results [39].

3.2.2 Limit Setting

The CL_s value is used to test the signal+ background hypothesis. The previous sections have outlined the test statistics used to calculate CL_s values. The accepted confidence level for exclusion of a signal is 95% which equates to $\text{CL}_s = 0.05$. Calculations of CL_s are repeated adjusting the value of μ until $\text{CL}_s = 0.05$. The value of μ at this point is called the “95% Confidence Level limit on μ ”. It is this value which is normally plotted when looking at limit setting for a data set, see fig. (3.2). In the case of the search for a SM Higgs boson, the signal strength parameter, μ , corresponds to the Higgs production

cross section divided by the cross section expected under the SM. This means that if the “95% Confidence Level limit on μ ” for a specific Higgs mass m_H is less than 1 a SM Higgs has been excluded at this mass.

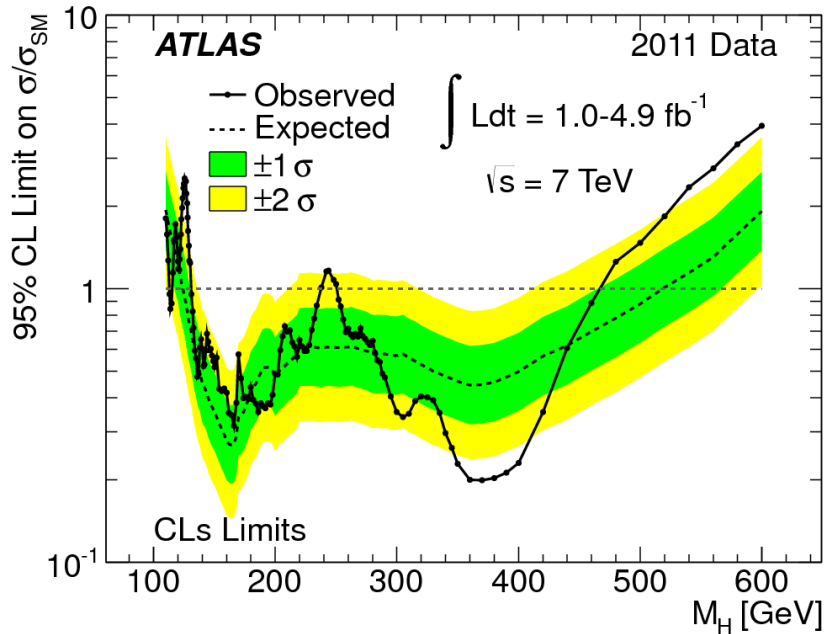


Figure 3.2: Example of a plot showing the 95% Confidence Level upper limit on μ . The horizontal dotted grey line at $y = 1$ shows the cut off for excluding a SM Higgs. If the observed limit is below this line, it is excluded. The observed limits are represented by the solid black line joining the dots which show the actual calculated values at specific mass points. The black dotted line is the expected median in the absence of a signal and the green and yellow strips show respectively the 1 and 2 σ bands.

Observed limits are produced by calculating the likelihoods of the two hypotheses with respect to observed data. Expected limits are calculated using the same procedure except calculated with respect to background only pseudo-data. The expected limits calculations are repeated several times allowing a cumulative probability distribution of results to be produced. From this the median and $\pm 1, 2\sigma$ expected bands limits can be read off. Since the expected

limits consider the background only scenario, an observed result larger than the expected result shows an excess of events. The quantification of an excess of events should be handled differently and is outlined in the next section.

3.2.3 Quantifying an Excess

If an excess of events is observed, limit setting will no longer give exclusion results. In this case we must also test the background hypothesis. The background-only p-value, as stated before, gives the probability for a background fluctuation to produce the excess of events, mimicking a signal. In this case the lower the probability of an excess being a background fluctuation the more confidence we can have in declaring the excess as a result of signal.

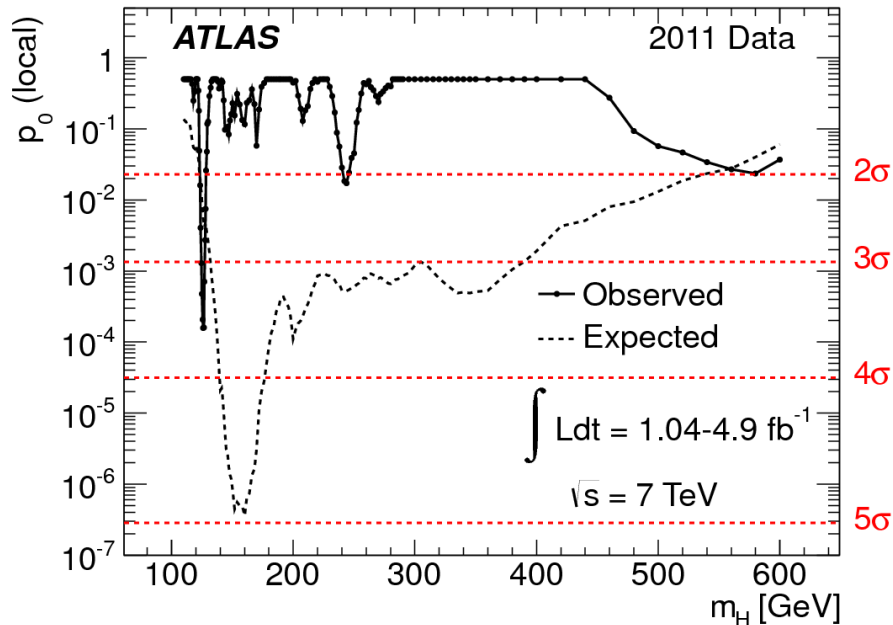


Figure 3.3: Example of a p_0 plot, showing both the local p -values and the equivalent significances (red dashed lines).

The p-value is calculated by evaluating the test statistic for the null hy-

pothesis, referred to as q_0 , see the black filled area in fig. (3.1). As for limit setting, the inclusion of the nuisance parameters and repetition of the procedure allows for a distribution to be produced $f(q_0 | 0, \hat{\theta}_0^{\text{obs}})$. The p-value corresponding to a given experimental observation q_0^{obs} is then evaluated as;

$$p_0 = P(q_0 \geq q_0^{\text{obs}}) = \int_{q_0^{\text{obs}}}^{\infty} f(q_0 | 0, \hat{\theta}_0^{\text{obs}}) dq_0. \quad (3.11)$$

An excess of events is more normally quoted as having a ‘‘significance’’ denoted as Z . This is converted by integrating one tail of a Gaussian curve from Z to infinity;

$$p = \int_Z^{\infty} \frac{1}{\sqrt{2\pi}} \exp(-x^2/2) dx = \frac{1}{2} P_{\chi_1^2}(Z^2). \quad (3.12)$$

where $P_{\chi_1^2}$ is the remnant of the Gaussian. Using this a 5σ ($Z = 5$) significance, which is the convention for claiming discovery, equates to a p-value of $p_0 = 2.8 \times 10^{-7}$, see fig. (3.3).

The p-value discussed here is calculated for a fixed mass point and is therefore referred to as a ‘‘local’’ p-value. Since this will be repeated for many mass points over the entire range of the search there is a dilution effect known as the Look Elsewhere Effect. A simplified case would be where an experiment is repeated over a range (hence ‘‘looking elsewhere’’), then a p-value of $\frac{1}{n}$ is likely to occur after n repetitions, even if there is no effect. In the simple case outlined above this effect would be compensated for by multiplying the p-value by the number of repetitions. In the more complex case of Higgs searches the treatment of the LEE is not so straight forwards, but must none the less be considered and included [40].

3.2.4 Bayesian Results

As discussed before the Bayesian approach is to assign a degree of belief to the hypothesis, in this case the presence of a SM Higgs. For a signal strength μ

we construct the posterior pdf $L(\mu)$;

$$L(\mu) = \frac{1}{C} \int_{\theta} p(\text{data} | \mu s + b) \rho_{\theta}(\theta) \pi_{\mu}(\mu) d\theta, \quad (3.13)$$

where $\rho_{\theta}(\theta)$ are functions describing our prior belief in the predictions made on count rates by uncertainties, $\pi_{\mu}(\mu)$ is the prior on the signal strength, commonly taken to be flat for positive values of μ and C is a constant so that the function is normalised to 1.

Bayesian one-sided confidence limits on μ are taken from;

$$\int_0^{\mu_{95\%CL}} L(\mu) d\mu = 0.95. \quad (3.14)$$

Frequentist results form the basis of the statistics work done on ATLAS data, however Bayesian results are also calculated.

3.3 Software Tools

3.3.1 MCLimits

`MCLimits` is a statistical program developed by Tom Junk[41]. It uses the Profile Likelihood test statistic. It was designed to include the systematic uncertainties arising from imperfectly specified models. Uncertainties in the expected count rates can be constrained by taking subsidiary measurements, which still lead to uncertainties when predictions are extrapolated or interpolated to the model to be tested. The prediction of a signal being tested will also include uncertainties. The Monte Carlo or data histograms used for hypothesis testing will also include uncertainties which must be accounted for by the program. `MCLimits` runs in ROOT [42] the data analysis framework used at CERN.

The approximation to Profile Likelihood used in `MCLimit` is given by [43]:

$$q_\mu = -2 \ln Q = \chi^2(\text{data} | H_1) - \chi^2(\text{data} | H_0) = \Delta\chi^2, \quad (3.15)$$

where the minimisations over χ^2 are done separately for both hypotheses.

Unfortunately, analyses such as those carried out in high energy physics must take account of systematics. The χ^2 function used when minimising the likelihoods in `MCLimits` takes account of symmetric and asymmetric uncertainties as well as shape uncertainties.

For a binned analysis symmetric uncertainties are described by:

$$r_{ij}^{\text{varied}} = r_{ij}^{\text{central}} \left(\prod_{k=1}^K (1 + s_k f_{kj}) \right), \quad (3.16)$$

where i is the bin number, j is which part of the model the uncertainty is associated to, k is the index for the nuisance parameters s_k which are modelled as Gaussian distributions centred around zero with unit width. f_{jk} are the fractional uncertainties on the normalisation of j due to the k^{th} nuisance parameter.

Asymmetric uncertainties are parametrised quadratically on a smoothly varying nuisance parameter, meaning the variation is given by:

$$r_{ij}^{\text{varied}} = r_{ij}^{\text{central}} \left(1 + s_k \left(\frac{f_{kj}^+ - f_{kj}^-}{2} \right) + s_k^2 \left(\frac{f_{kj}^+ + f_{kj}^-}{2} \right) \right), \quad (3.17)$$

here the quantity f_{kj}^+ (f_{kj}^-) is the fractional change in the rate of j when s_k is positive (negative) one unit. It can be positive or negative. For symmetric uncertainties $f_{kj}^+ = -f_{kj}^-$.

The function including systematics used is then:

$$\begin{aligned}
\chi^2 = & 2 \sum_{i=1}^I \left[\left(\sum_{l=1}^L t_{li} \prod_{k=1}^K (1 + f_{lk}^t S_k) + \sum_{j=1}^J \rho_{ji} - n_i \right) \right. \\
& - n_i \ln \left(\frac{\sum_{l=1}^L t_{li} \prod_{k=1}^K (1 + f_{lk}^t S_k) + \sum_{j=1}^J \rho_{ji}}{n_i} \right) \\
& + \sum_{j=1}^J \left(\left(\frac{\rho_{ji}}{F_j \prod_{k=1}^K (1 + f_{jk}^F S_k)} - b_{ji} \right) - b_{ji} \ln \left(\frac{\rho_{ji}}{F_j \prod_{k=1}^K (1 + f_{jk}^F S_k) b_{ji}} \right) \right) \left. \right] \\
& + \sum_{k=1}^K S_k^2.
\end{aligned} \tag{3.18}$$

i is the index for the I -binned histogram used; bin i contains n_i events; J represents the components of the model subject to Poisson statistics which are run over by the index j ; L represents the non-Poisson components and similarly are associated to the index l ; K are the independent sources of systematic uncertainty, parametrised by S_k where k is the index of K . t_{li} is the model prediction for the l th non-Poisson component in bin i ; b_{ij} is the number of counts in bin i from the subsidiary Poisson measurement which determines the model contribution. This value must be scaled to compute the expected contribution from this model to bin i , the central value of this is $F_j b_{ij}$ for Poisson source j . The unknown, ρ_{ij} , the rate of Poisson component j in bin i , is solved by minimising χ with respect to all of these. f_{jk}^F is the relative uncertainty on F_j due to systematic uncertainty k and f_{lk}^t is the relative uncertainty on t_{li} due to systematic uncertainty k .

Shape uncertainties are also included in the model. They are specified by providing alternative shape histograms for the model predictions for each nuisance parameter. If shape uncertainties are provided for a particular nuisance parameter and model component then variations of the nuisance parameter when toy throwing are restricted to be between the upper and lower shape variations.

The software available for running `MCLimits` is able to be run as a compiled script within ROOT taking histograms as inputs. It is built on the function shown in eqn. (3.18) and extended to allow simultaneous searches over several data histograms, meaning several searches for new physics can be combined together. These simultaneous searches can be used to combine different channels in the search for a Higgs boson. Each channel will contain all the information related to that channel; model information, data plots and nuisance parameters. Nuisance parameters are taken to be either 100% correlated or completely uncorrelated. If they are correlated they should have the same name in all channels.

`MCLimit` has the ability to call another program, `genlimit` written by Joel Heinrich [44] which allows Bayesian results to be produced, sharing as much of the preparation work as possible. The pseudo experiment set-up used to calculate p -values can be adapted for Bayesian results.

3.3.2 RooStats

`RooStats` [45] is a joint project between ATLAS and CMS, based on ROOT and `Roofit` [46], overseen by the ATLAS and CMS statistical committees. The aim of `RooStats` was to create a generic and versatile software able to implement different statistical methods for both simple number counting experiments and more complex ones which may include parametrisations of experimental distributions. `Roofit` provides classes for the declaration of models which can then be used by `Roostats` for all the specific high level statistical tools.

A useful tool in the `Roofit` framework is the workspace. The workspace contains data, fit, parameters and model information which can then be saved and shared as and when desired. The `RooStats` approach to combining re-

sults from multiple experiments was to use these workspaces. A macro, called `HistFactory` exists which can create a workspace from a string interface using a standard xml template and root files containing associated histograms.

`RooStats` implements different calculators according to which is required. The one of most interest in this thesis is the `ProfileLikelihood Calculator`, which applies the same technique as that of `MCLimits` outlined in the previous section except for the differences in the test statistic outlined in section 3.2.1.3.

There are two Bayesian calculators available in the `RooStats` framework, `BayesianCalculator` and `MCMCCalculator` (Markov-Chain Monte Carlo) . They both start from the model and data sets used to build the likelihood functions, incorporating, if they're present, the priors of the parameter of interest and nuisance parameters. They are integrated by the calculator using Monte Carlo techniques to obtain the posterior distribution. `BayesianCalculator` works if there is only one parameter of interest, using analytical or numerical integration to compute the posterior probability. `MCMCCalculator` uses a Markov-Chain Monte Carlo to perform the integration.

Since `MCLimits` had been used by previous experiments a comparison of the performance of the old and the new software tools offered an interesting way of validating the performance of both and cross-checking any results which would go on to be published. An adaptation of the framework being created for `RooStats` analyses would maximise the usefulness and utility of any comparison tool.

3.3.3 Comparison

Before starting to create a specific framework for comparing the two packages when considering Higgs searches, a toy situation was devised to take a first look at treatments of samples and gain a better understanding of both packages. Table 3.1 gives the outline of the conditions as they were for the toy experiment and Fig. 3.4 shows the input plots used for the comparison.

Two channels were considered, a one bin channel and a two bin channel. The one bin channel contained identical background and signal input histograms. The two bin channel considered input histograms that varied between signal and background. The data plots were taken as background only. The background rate was taken as 1, and the signal rate as 0.1. The CL_s value was then calculated over the entire signal range, from 0 to 100% of the 0.1 rate, using both `MCLimits` and `RooStats` and plotted as a function of the signal fraction. The $\pm 1\sigma$ values were also calculated and included in the plots. `MCLimits` has a function which allows for the assumption that the entries in each bin are Poissonian, and applies fluctuations accordingly. `MCLimits` was run twice, once with this function turned on and once without. The results of these analyses are shown in fig. (3.5). The `MCLimits` results produced without Poissonian fluctuations applied agree with those produced by `RooStats`. The assumption must be that in this case there is no bin-by-bin uncorrelated uncertainty. Future comparisons must also start from this assumption and so all `MCLimit` calculations shown later in this thesis do not use this function.

The simple toy experiment showed that in very basic situations the two programs produced results in agreement with one another. Clearly a more advanced model would need to be considered, including nuisance parameters, before any stronger statements could be made. The success of a statistical

	MCLimits	RooStats
Test statistic	Eqn. 3.9	Eqn. 3.10
Input histograms	Normalised to required luminosity	Normalised to unity
Nuisance parameters	Symmetric, asymmetric and shape variations	Symmetric, asymmetric and shape variations. No bin-by-bin fluctuations
Number of toy pseudo experiments	Same for both hypotheses	Different according to hypothesis

Table 3.1: Table outlining particulars of the set up of the two programs for the analysis of a toy experiment.

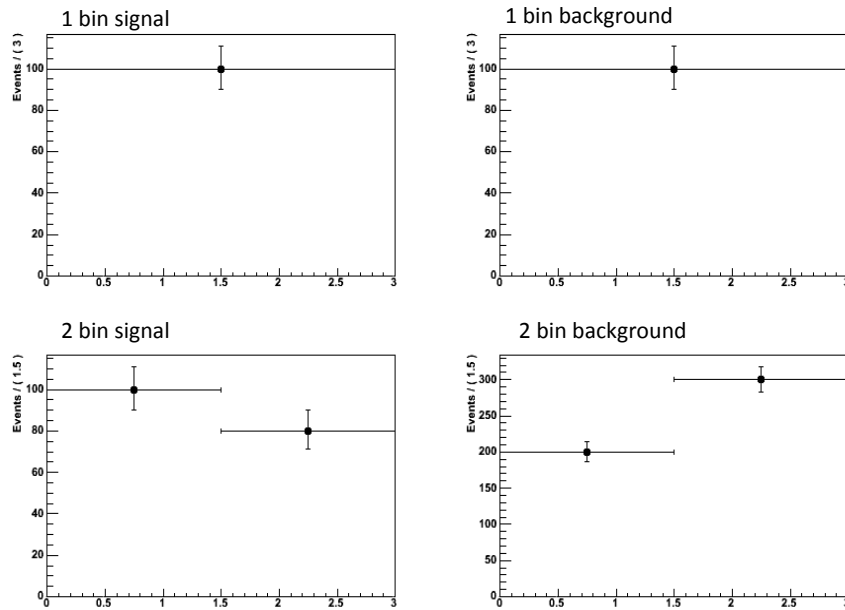


Figure 3.4: Two-channel toy experiment inputs. Signal is on the left and background is on the right.

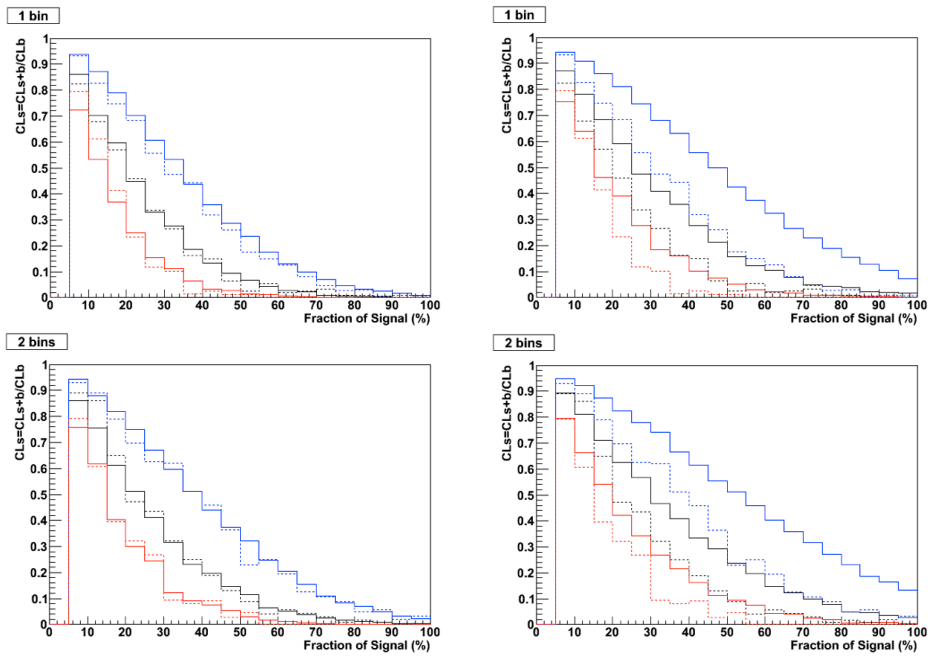


Figure 3.5: *Expected CLs value as a function of fraction of signal for the 1 and 2-bin channels in the toy experiment. RooStats results are dashed lines and MCLimits are solid lines. The black lines are the median results and the blue and red correspond to $\pm 1\sigma$ values. The plots on the left are where MCLimits has been run assuming the bin entries are not Poisson, whereas those on the right assume they are.*

program clearly depends on the quality of the inputs. With this in mind the next step was to move away from toy experiments to adapting `MCLimits` to the particular format of ATLAS results.

Chapter 4

Adapting `MCLimits` in a `Roostats` Environment

4.1 Constraints of `MCLimits`

The architecture of `MCLimits`, developed building on the experiences at the Tevatron, runs as a compiled script in `ROOT`. Instances of classes describing the models of the two hypotheses are created, which contain template histograms to be fitted to the data and descriptions of all the systematic uncertainties and correlations between them. An analysis may be made up of more than one channel, in which case the hypothesis models are collections of the available channels. Each channel will correspond to one data histogram. All the variables pertinent to a channel are stored in arrays, declared in a separate C++ file edited by the user. `MCLimits` is not the primary software choice for the analysis of LHC results, and here has not been altered to use the LHC test statistic, but it is important that it can be used as a cross-check. To avoid setting up the `MCLimits` architecture from scratch in the LHC environment, which would have necessitated a large amount of coding, an interface was

required. This is described below and was one of my primary contributions.

4.2 MCLimits with XML Interface

The `RooStats` developers adopted a different approach to inputting the data needed to create hypothesis models. `HistFactory` [47] is a routine which builds the probability density functions and saves them to `RooWorkspaces`. The input histograms are stored in `ROOT` files and organised using an XML [48] file.

By writing an interface to `MCLimits` which uses the same XML files and XML schema as `HistFactory`, the cumbersome task of rewriting all the channel input files for `MCLimits` could be bypassed. This would also reduce the possibilities for user error and make `MCLimits` a more attractive option for people analysing channels who wish to cross check their own results.

With the interface completed, initial comparisons of `MCLimits` and `RooStats` could begin. By this point, separate channels had begun to produce XML and companion `ROOT` files for limit setting using `RooStats`. One of the first channels investigated for these comparisons was $H \rightarrow ZZ \rightarrow ll\ell\ell$. It was selected since it used the `HistFactory` method to produce `RooWorkspaces` and was a fairly stable channel, with a robust method which meant that the XML and `ROOT` input files were ready in advance of some of the other channels. Each mass point, when analysed with `MCLimits`, took just under 6 hours of CPU time. A selection of points over the entire range covered by the 4 lepton channel were run through the `MCLimits` machinery and the results offered as a comparison to the ATLAS Preliminary `RooStats` produced results see fig. (4.1) and table (4.1) . The results shown in fig. (4.1) represent a proof of concept. The `MCLimits` results appear to give tighter limits than `RooStats` for larger

Higgs mass [GeV]	MCLimits expected	RooStats expected	MCLimits observed	RooStats observed
115	25	40	26	40
120	10	16	10	17
130	3	6	3	6
140	3	3	4	4
160	3	5	3	5
180	2	4	2	4
200	1	2	1	2
300	1	2	1	2
400	1	3	1	3
600	8	15	10	25

Table 4.1: Table comparing expected and observed limits for $H \rightarrow ZZ \rightarrow llll$ obtained using *MCLimits* and *RooStats* for 1.1fb^{-1} of integrated luminosity at a centre of mass energy of 7 TeV.

masses but, on further investigation, a scaling factor applied to cases greater than 200 GeV had been incorrectly read in the *MCLimits* wrapper.

The wrapper was updated and further tests on $H \rightarrow ZZ \rightarrow llll$ and other channels that produced workspaces using HistFactory, showed an improved agreement, see fig.(4.2). The agreement between the two statistical frameworks is still not within acceptable limits. In general *MCLimits* gives tighter limits than *RooStats*. As the amount of luminosity considered increases the discrepancy between the two frameworks reduces.

As the XML and ROOT files became available other channels were used as input, see fig. (4.2). Once the inputs for *MCLimits* have been prepared, *MCLimits* can also be used to calculate Bayesian limits, see fig. (4.3). Frequentist limits have been the standard in ATLAS so far but a comparison between the two methods is occasionally made as a valuable cross-check. Even

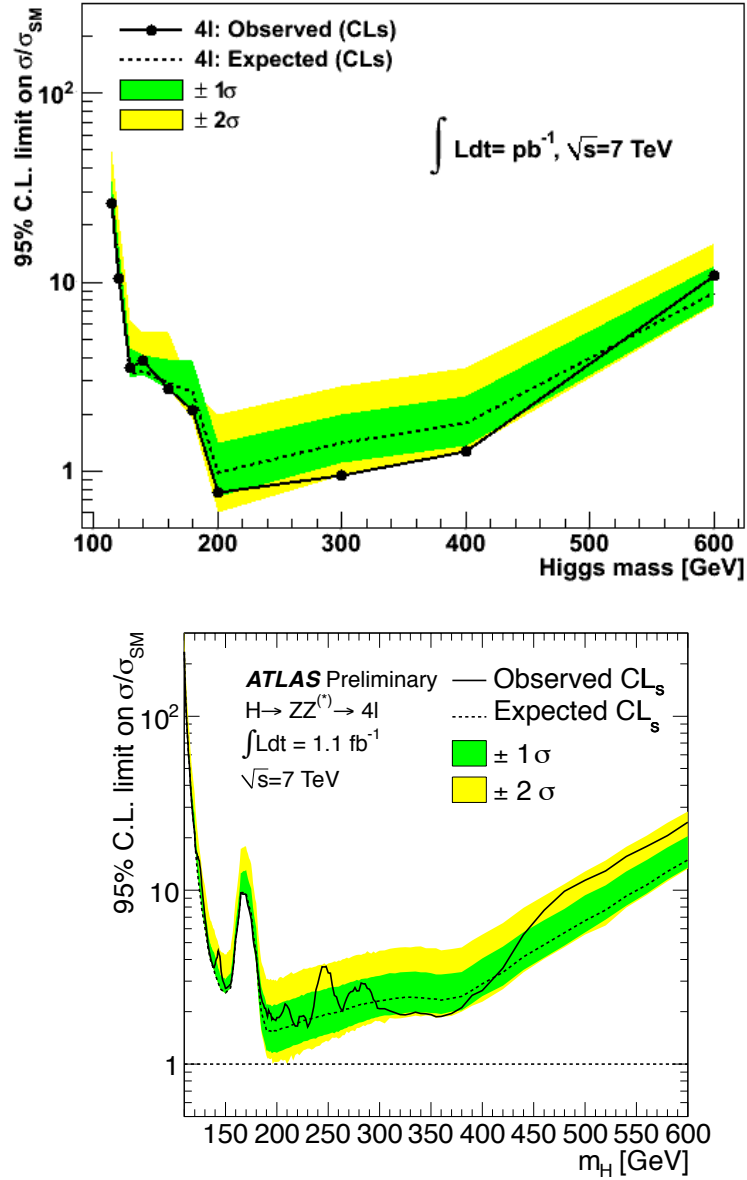


Figure 4.1: Limit plots for $H \rightarrow ZZ \rightarrow llll$ channel produced with *MCLimits* on the top and *Roostats* on the bottom. Both plots are produced from the same XML and ROOT input files, representing 1.1fb^{-1} of integrated luminosity at a centre of mass energy of 7 TeV. The solid lines show observed limits and dashed expected. Green and yellow bands represent 1 and 2 sigma bands respectively.

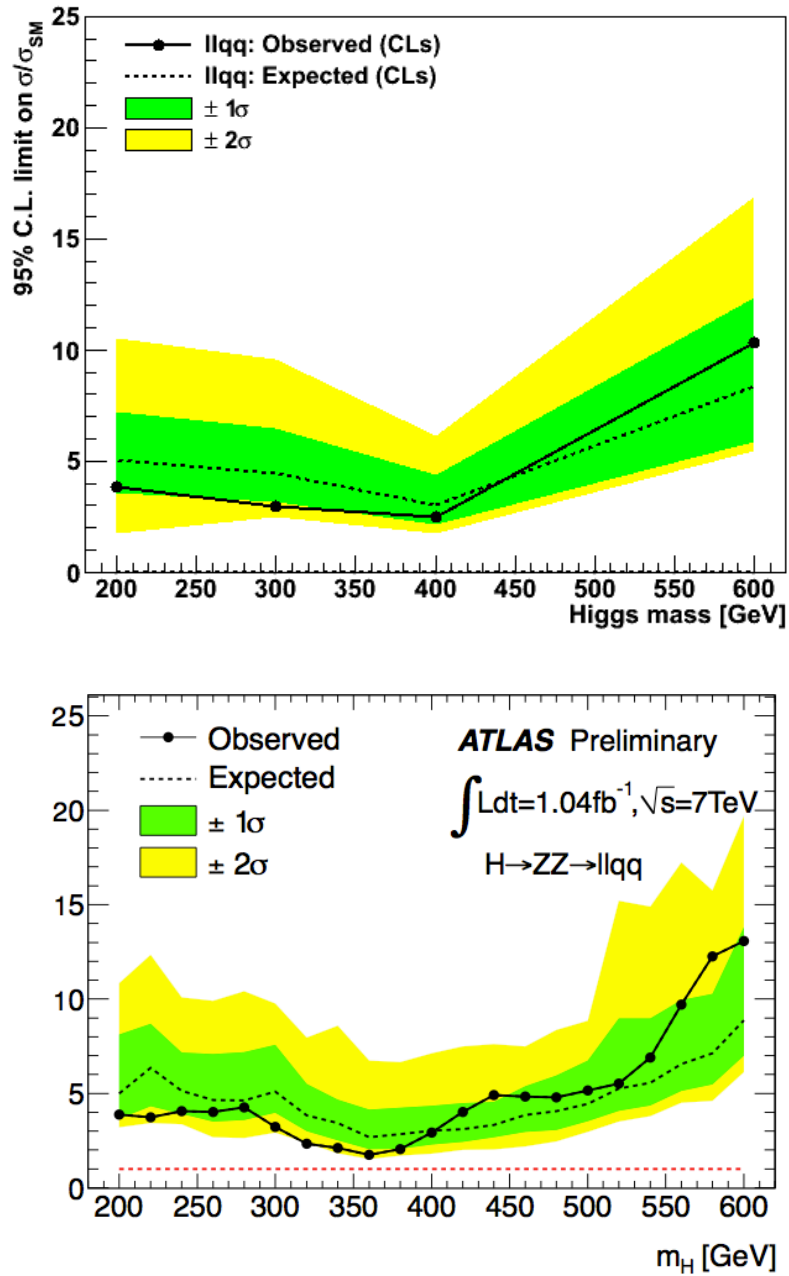


Figure 4.2: Limit plots for $H \rightarrow ZZ \rightarrow llqq$ channel produced with *MCLimits* on the top and *RooStats* on the bottom. Both plots are produced from the same XML and ROOT input files, representing 1.04 fb^{-1} of integrated luminosity at a centre of mass energy of 7 TeV. The solid lines show observed limits and dashed expected. Green and yellow bands represent 1 and 2 sigma bands respectively.

Higgs mass [GeV]	MCLimits expected	RooStats expected	MCLimits observed	RooStats observed
200	5.0	5.0	3.9	3.9
300	3.6	4.9	3.0	3.1
400	3.3	3.1	2.7	3.1
600	8.2	8.8	10.2	13.1

Table 4.2: Table comparing expected and observed limits for $H \rightarrow ZZ \rightarrow llqq$ obtained using *MCLimits* and *RooStats* for 1.04fb^{-1} of integrated luminosity at a centre of mass energy of 7 TeV.

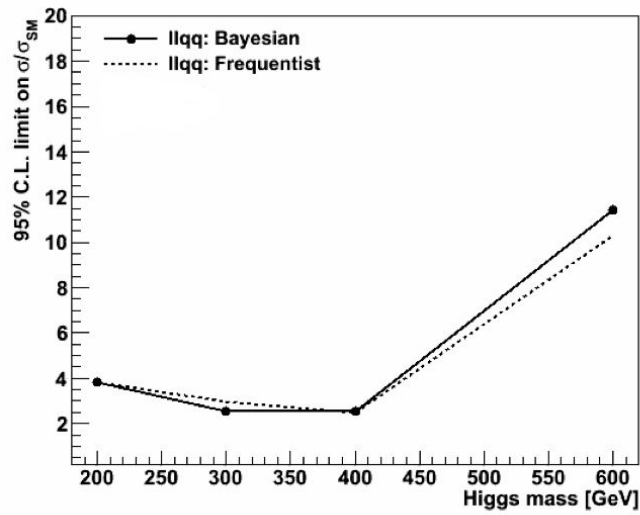


Figure 4.3: Comparison of the observed limits for the $H \rightarrow ZZ \rightarrow llqq$ channel. The dashed line is the frequentist limits and solid represents Bayesian limits. Both sets of limits are produced using *MCLimits* from the same XML and ROOT input files, representing 1.04fb^{-1} of integrated luminosity at a centre of mass energy of 7 TeV.

for a relatively small integrated luminosity dataset the two calculators agree within 10% across the entire mass range, indeed agreeing within 5% for the majority.

4.3 MCLimits from Workspaces.

Not all channel working groups use the HistFactory method for producing their workspaces. As of winter 2011, workspaces were created for $H \rightarrow \gamma\gamma$ and $H \rightarrow WW$ channels by defining the signal and background pdfs and manually specifying the form of the component parameters (see for example [49]). The different construction format necessitated a new wrapper in order to use MCLimits as the statistical software tool. Since the workspaces already existed and the construction method was not widely known the ideal would be to ‘backward engineer’ from the workspaces, extracting the inputs needed for MCLimits converting the format as and where necessary. The easiest way to start this process was by trying to extract the information from a workspace which had been produced in a known manner, i.e. one of the HistFactory produced workspaces. For similar reasons to before, $H \rightarrow ZZ \rightarrow lll$ was chosen as a test channel.

4.3.1 HistFactory produced workspaces.

The XML files used to create the workspaces can be split into two types: a top level file which, amongst other things, lists the lower level XML files, where each file represents a sub channel. The top level file contains instructions as to what the workspace should be called and where it should be saved, information on parameters which will be the same for all sub channels, for instance the luminosity and its error, and which parameter is the parameter of interest. In the search for the SM Higgs boson, the parameter of interest has been the Higgs signal cross section divided by the SM production cross section.

Each subchannel XML file, in essence, is a list of paths to histograms that

contain the data and the Monte Carlo simulations after the analysis of the sub-channel has been performed. Initially, most channels will perform a cut-based analysis, where the cuts, applied on selected variables, have been selected to favour signal events over background events wherever possible. The variables on which the cuts are applied differ between analyses, but can cover a wide range of properties of the events and the constituent particles as well as the geometric relationships between them. The XML line corresponding to the data histogram is a single line unlike those referring to the MC samples. The description of each sample, whether signal or background, like the data description, contains the path to the root file containing the representative histogram. The MC sample descriptions also contain information on the systematics relevant to that sample. The systematics can be given in one of two ways; either as a *histosys*, where two other histograms are given representing the maximum and the minimum of the sample under the effect of this systematic or as an *overallsys* which gives a flat error across the entire range of the sample and is given just as two values representing the percentage change in the histogram due to this systematic.

The workspace is created in a set manner when using HistFactory. According to how something is declared in the XML files it will be cast as a certain type of object within RooFit and then the objects combined in an approved way to create the model. Simple, stripped down workspaces were created, initially containing only one signal and one background sample as well as the data and no systematics. These toy workspaces were used to identify which format was used to save the bulk of the model. The different forms of systematics were added one by one and their presence in the workspace tracked. Finally by searching within a complete $H \rightarrow ZZ \rightarrow lll$ workspace created using XML files and the related ROOT files, which were also available, a full mapping between the RooFit casting and the direct element of the model in its input

form could be found.

The art of extracting the components of a workspace was perfected by Samir Ferrag. He built upon my work, described above, to create a tool which became known as ‘Workspace Extractor’ which could print out the contents of a histfactory produced workspace. The printed output could be controlled, printing out the contents to a specified depth, for instance the smallest depth would list just the subchannels contained in a workspace whereas the greatest depth would list the components of each subchannel model and the systematics relating to each component. The pdfs describing the distributions given by histograms could be viewed once again as histograms and compared with those that had been used as the primary input. ‘Workspace Extractor’ was used for a while on behalf of the Higgs combination working group to check for anything that was unexpected in the workspaces. Whilst the XML format was standardised and clearer than the declaration method used previously by `MCLimits`, a channel still needs hundreds of lines of code to fully describe it and errors do appear.

The next step towards running `MCLimits` from a workspace and testing the accuracy of ‘Workspace Extractor’ was to take the extracted components and use them as inputs to `MCLimits`. This was done in a similar way to the XML to `MCLimits` interface. The XML interface takes names given by the XML, accesses the (MCLimits compatible) objects they represent and hands these objects to the statistics machinery. The workspace interface extracts the (MCLimits incompatible) objects from the workspace, casts them into compatible objects and hands them to the statistics machinery. Checks using several different histfactory produced workspaces and the relative XML/ROOT file combinations were done. In all cases the XML interface and ‘Workspace Extractor’ produced identical results.

Higgs mass [GeV]	MCLimits expected	RooStats expected	MCLimits observed	RooStats observed
115	9.0	15.0	9.0	11.0
120	5.5	6.5	4.8	5.3
125	2.6	3.5	3.0	4.8
130	1.7	1.9	1.8	1.8
140	0.9	1.0	0.8	0.8
150	0.7	0.8	0.7	0.8

Table 4.3: Table comparing expected and observed limits for $H \rightarrow ZZ \rightarrow lll$ obtained using `MCLimits` and `RooStats` for 4.5fb^{-1} of integrated luminosity at a centre of mass energy of 7 TeV.

The bulk of the running time is taken up by the throwing of toy experiments, so the total time taken per signal mass did not change greatly depending on whether the XML or Workspace format was used. The best method for running the large number of CPU intensive jobs in this scenario was on batch systems. During these early days of limit setting at the LHC, `RooStats` was regularly updated to introduce new features or patches where bugs had been identified. This meant that analyses using `RooStats` (of which the `MCLimits` from workspace method was one) needed to use the most recent version of ROOT available. These versions of ROOT were frequently unavailable at grid sites. For this reason it was much more practical to install a copy of the needed ROOT release so that it could be local to a batch system and run the analyses there.

Fig. (4.4) and table (4.3) show one of the first `MCLimits` comparison plots produced using the batch system at Glasgow, which meant that the full mass range, rather than just a selection of mass points, could be used. Whilst the range shown on the `MCLimits` plot extends further than the official `RooStats` plot, comparing just the region shown on both shows many shape similarities:

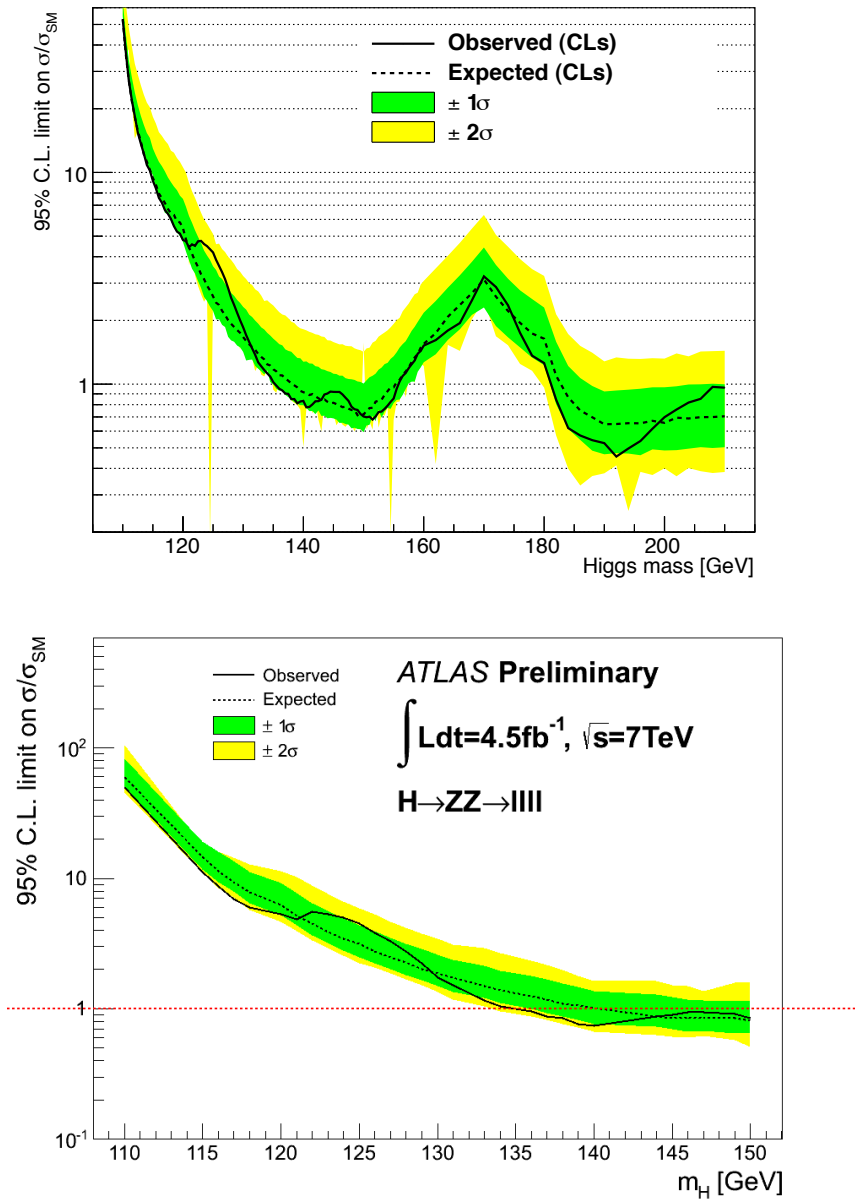


Figure 4.4: Comparison of *MCLimits* (top) and *RooStats* (bottom) limits for the $H \rightarrow ZZ \rightarrow llll$ channel. Analysis represents $4.5fb^{-1}$ of 7 TeV data. The *MCLimits* plot is produced using the workspace to *MCLimits* interface and 10,000 pseudo-experiments. The downward spikes shown in the yellow 2 sigma band are where 10,000 pseudo-events was not enough toy experiments to determine the correct value.

- A kink marking the beginning of a region where the observed is noticeably above the expected at 120 GeV.
- The end of the bump at 130 GeV
- The start of the excluded region (where the observed line passes below $y = 1$) at 135 GeV up until the end of the range shown by the `RooStats` plot.

The overall values show tighter limits being set by `MCLimits` than by `RooStats`. This is particularly the case for lower mass values where the limits themselves are larger. At $m_H = 115$ GeV the `MCLimits` expected value is nearly 50% tighter than that set by `RooStats`, however at $m_H = 150$ GeV this has reduced to less than 10%

A full range comparison of the expected and observed limits was also produced by the $H \rightarrow ZZ \rightarrow lll$ channel. This used the `MCLimits` results and compared them to the ATLAS standard (`RooStats` using asymptotic distributions of the test statistics, and employing a model data set to define the sensitivity of the experiment[34]) and also `RooStats` with toys, see fig (4.5).

The agreement in both plots between all three methods is very good. The expected limits agree within 5% over the entire mass range. The observed limits agree within 5% up to $m_H = 180$ GeV and within 10% over the rest of the considered mass range. In the expected plot between 200 and 350 GeV `RooStats` with toys has a less flat line than the other two. In the observed plot, below 180 GeV there is excellent agreement between `MCLimits` and `RooStats` with toys, with asymptotic `RooStats` seeming to produce a slightly tighter limit throughout. At higher masses the two `RooStats` limits agree better with each other than with `MCLimits`, again producing tighter limits.

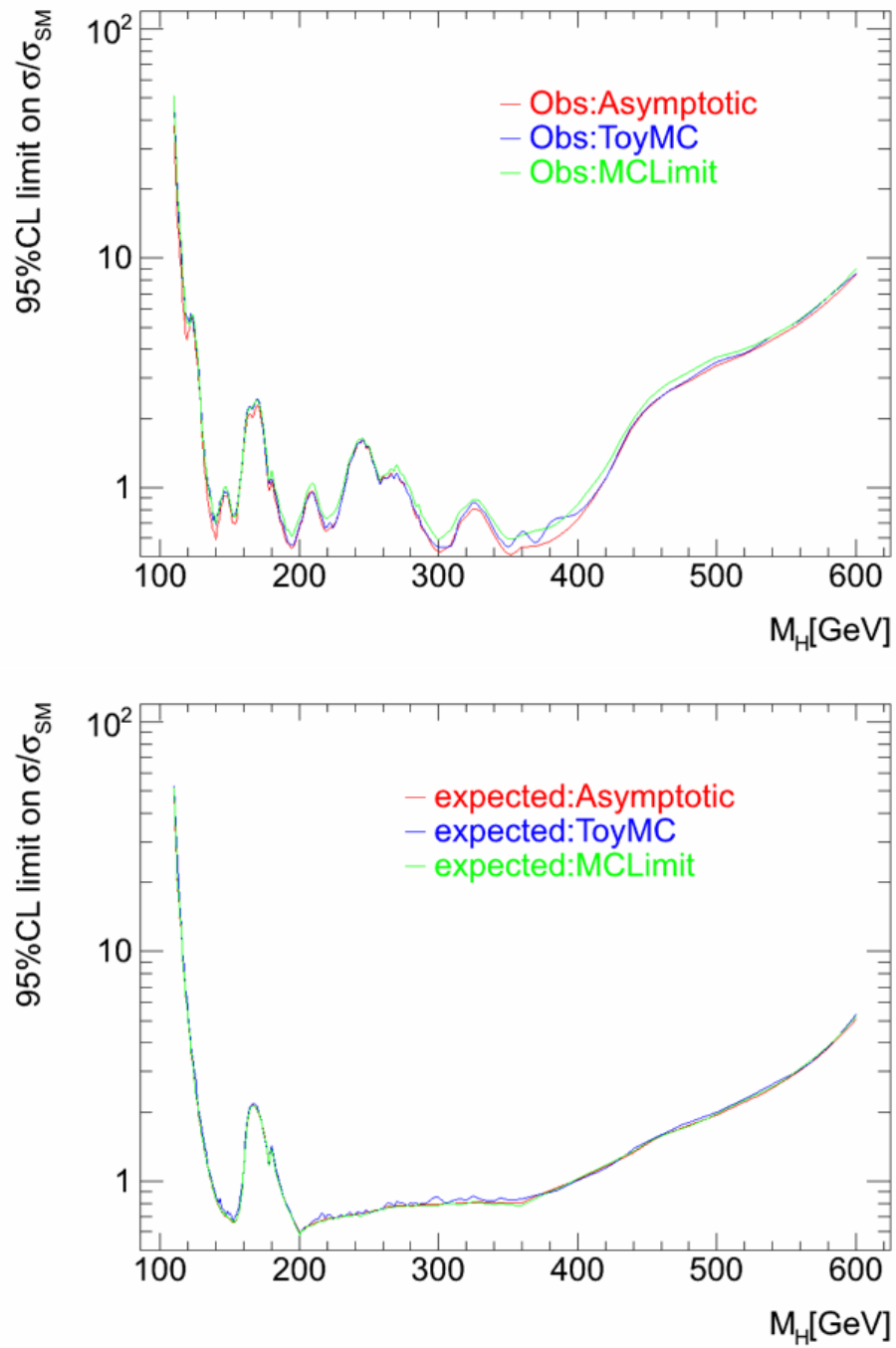


Figure 4.5: Comparison of observed (top) and expected (bottom) limits for the $H \rightarrow ZZ \rightarrow llll$ channel. Analysis represents 4.5fb^{-1} of 7 TeV data. The red line is calculated using *RooStats* employing asymptotic approximations, blue is *RooStats* throwing toys experiments and green is *MCLimits*.

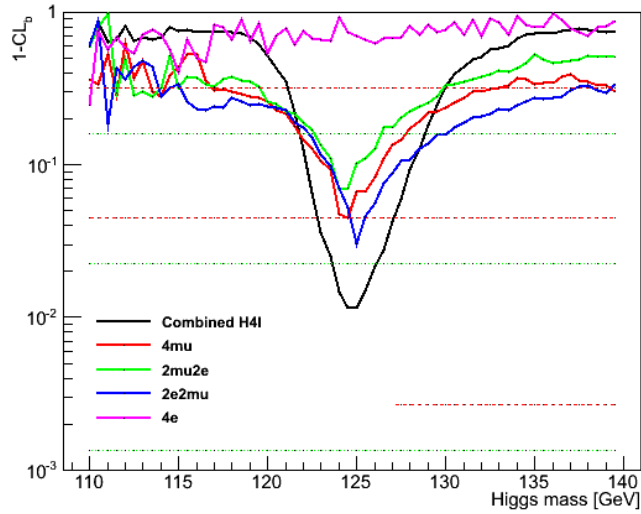


Figure 4.6: p_0 plot for the $H \rightarrow ZZ \rightarrow lll$ channel. The black line shows the combination of the four sub-channels, shown separately in colours. The green horizontal dotted lines represent, from top to bottom, 1, 2 and 3 sigma deviations.

The statistical output of `MCLimits` also provides p_0 values. The corresponding p_0 plot for the $H \rightarrow ZZ \rightarrow lll$ channel is shown, fig. (4.6). From this plot one can see a lack of candidates in the $H \rightarrow ZZ \rightarrow eeee$ channel. The subchannels combine to give a maximum significance of 2.2σ at a mass of 125 GeV.

These comparison plots marked the first real complete results produced using the `MCLimits` software interfaced to the initial stages of the ATLAS approved statistical framework. It showed that, at least in this case, when everything was correctly done, `MCLimits` produced a competitive result and was a good tool for cross checking results.

4.3.2 Non-HistFactory produced workspaces

The HistFactory produced channels all use histograms as their inputs. For the $H \rightarrow \gamma\gamma$ channel a different method was chosen, instead modelling the signal and background shapes as unbinned pdfs, fitted to MC simulations. Inside the workspace the model pdf was still listed as the combination of a series of different pdfs, they were just declared differently. This required me to modify and extend the `MCLimits` comparison framework.

Instead of trying to rewrite `MCLimits` to accept similar unbinned pdfs as model inputs it was decided to create binned histograms from the unbinned pdfs and normalisation factors held within the workspace. Using a similar technique to before, the composite model was unravelled piece by piece, allocating each part to a particular type of input information to be given to `MCLimits`. When a pdf was extracted that needed to be converted into a binned histogram before being handed to `MCLimits` it was routed through a method in the code which could create this histogram. The pdf in question was used to generate thousands of events, which then filled a binned histogram. This histogram was then scaled using the normalisation factor associated to the pdf in the workspace.

Fig. (4.7) shows the results of this binning, unbinned pdfs method. A comparison between this plot and the official ATLAS `Roostats` plot shows a few things:

- The overall shape of the two observed lines is very similar.
- The sigma bands are much larger for `MCLimits`.
- Most importantly the `MCLimits` plot appears to be scaled by a factor of 2 in relation to the `Roostats` plot.

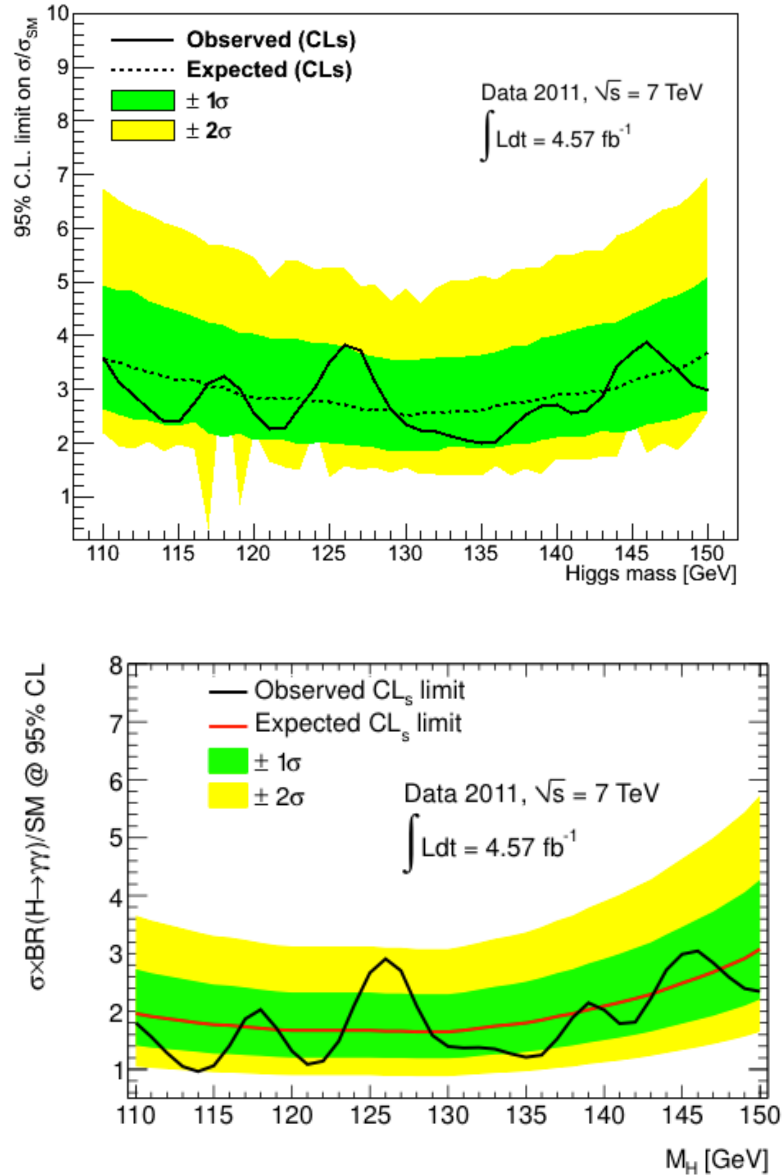


Figure 4.7: Comparison of *MCLimits* (top) and *RooStats* (bottom) limits for the $H \rightarrow \gamma\gamma$ channel. Analysis represents 4.57fb^{-1} of 7 TeV data. The *MCLimits* plot is produced using the workspace to *MCLimits* interface, producing binned histograms from the unbinned pdfs contained within. Limits set using *RooStats* seem to be a factor of 2 tighter than those set using *MCLimits*

Higgs mass [GeV]	MCLimits expected	RooStats expected	MCLimits observed	RooStats observed
115	1.6	1.8	0.9	1.8
120	1.5	1.7	1.2	1.7
125	1.5	1.8	3.0	1.8
130	1.5	1.6	1.5	1.6
140	1.6	2.0	1.5	1.9
150	2.1	2.7	1.6	1.8

Table 4.4: Table comparing expected and observed limits for $H \rightarrow ZZ \rightarrow \gamma\gamma$ obtained using *MCLimits* and *RooStats* for 4.9fb^{-1} of integrated luminosity at a centre of mass energy of 7 TeV.

The fact that the *MCLimits* plot appears to be scaled by almost exactly 2, was initially a cause for concern; a stray factor of 2 could have crept in during production. The *MCLimits* machinery was checked but nothing could be found to support this idea. Several months of investigation still produced no resolution as regards the difference between the two plots.

The total 7 TeV dataset for the $\gamma\gamma$ channel was 4.9fb^{-1} . The analysis of this dataset was published [50] and used in the final combination of just 7 TeV data [51]. The workspaces produced for the combination from this point became the most complete and reliable source. As well as the full combination, the separate channel workspaces and workspaces using combinations of a few subchannels, for instance all $H \rightarrow ZZ$ subchannels were produced and stored centrally. These central workspaces were particularly useful in testing which subchannels were still incompatible with the *MCLimits* wrapper. Some modifications had to be made to ensure that channels that had run previously, such as $H \rightarrow ZZ \rightarrow lll$ still ran, due to changes in naming conventions. With this in mind, the $H \rightarrow \gamma\gamma$ workspaces were tested and re-run also, using the full 7 TeV dataset. Fig. (4.8) and table (4.4) shows the results of using the centrally

produced workspace in comparison with the official published result. The limits set by `MCLimits` then became tighter than those set by `RooStats`, reflecting the results that had been found using HistFactory produced workspaces. The conclusion to be drawn is that the format of the workspaces had changed.

The difference between the two results using the same machinery must be due to differences in how the inputs are created. The method used previously, before the central production produced erroneous results when used in conjunction with the `MCLimits` wrapper. This was clearly not a problem when these workspaces were used to calculate limits using `RooStats`. The reason for the difference was not trivial to find, despite months of searching. Since there was already a move towards more standardised, central production and the differences observed were not seen as a high priority by the ATLAS Higgs group, the centralised production storage location was bookmarked and workspaces taken only from there for the rest of the work shown in this thesis.

$H \rightarrow \gamma\gamma$ was not the only channel to not use HistFactory. The $H \rightarrow WW$ analysis team also chose not to use HistFactory even though their analysis was binned. Early attempts at unpacking the WW workspace with the existing machinery failed. This meant that the workspace was composed in an entirely different way to any of the other channels. Enquires into the formulation of the workspaces produced for the WW channel revealed that it was intended to move away from the initial method used to create workspaces to a procedure described as being 'more HistFactory-like'.

These are the workspaces which are used as input to `RooStats` to produce the full combination statistical plots. Ideally the `MCLimits` interface should be able to read and run on these full combination workspaces. Since the creation method was set to change significantly, waiting for the newer format would be a prudent move.

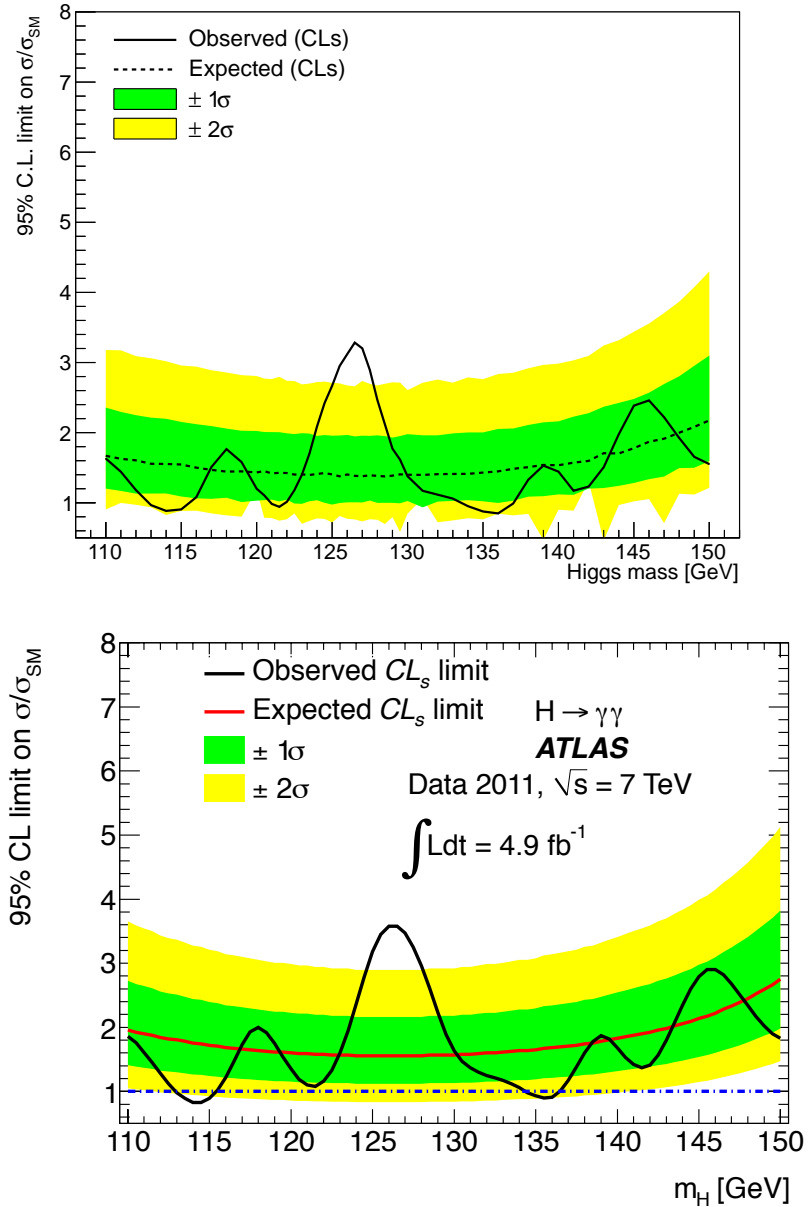


Figure 4.8: Comparison of *MCLimits* (top) and *RooStats* (bottom) limits for the $H \rightarrow \gamma\gamma$ channel. Analysis represents 4.9 fb^{-1} of 7 TeV data. The workspace used to produce the *MCLimits* plot is taken from the central repository. The *MCLimits* wrapper and mechanism is the same as previously.

Spring 2012 brought more data, this time at 8 TeV centre of mass energy and the publication of the results using the full 7 TeV dataset. The full 7 TeV dataset analysis also meant a new format for the remaining workspaces that were incompatible with the `MCLimits` interface. At this time $H \rightarrow WW$ had two subchannels $H \rightarrow WW \rightarrow l\nu l\nu$ and $H \rightarrow WW \rightarrow l\nu qq$. The change in production mechanism meant that the two $H \rightarrow WW$ channels, although slightly different in construction to each other still, could be used as input to the existing `MCLimits` code after adapting it for these channels.

With data and model information able to be extracted from the workspaces for all the subchannels it was possible to run on the full combination workspace, i.e. including all of the channels that were being analysed in the search for the Higgs boson. All of the extraction techniques were amalgamated and a small check to determine which extraction subroutine to use for each subchannel was implemented. The number of pseudo-experiments was increased to 1,000,000 to improve the calculation of the sigma bands. With this high number of pseudo-experiments each mass point in the full combination took 3 days to run.

$m_H = 120$	observed	expected	-1σ	-2σ	$+1\sigma$	$+2\sigma$
<code>MCLimits</code>	0.74	0.98	1.38	1.85	0.71	0.53
<code>RooStats</code>	0.7	1.0	1.4	1.8	0.7	0.5

Table 4.5: Full combination at 120 GeV. `RooStats` values only known to 1 decimal place.

Fig. (4.9) shows the official ATLAS Full combination Higgs search results analysed using `Roostats`, presented at the Moriond conference (March 2012) as well as the same `RooStats` workspaces analysed using `MCLimits`. As with the subchannel comparisons the full combination results are very close in shape. The overall values are also now in good agreement, continuing the trend where

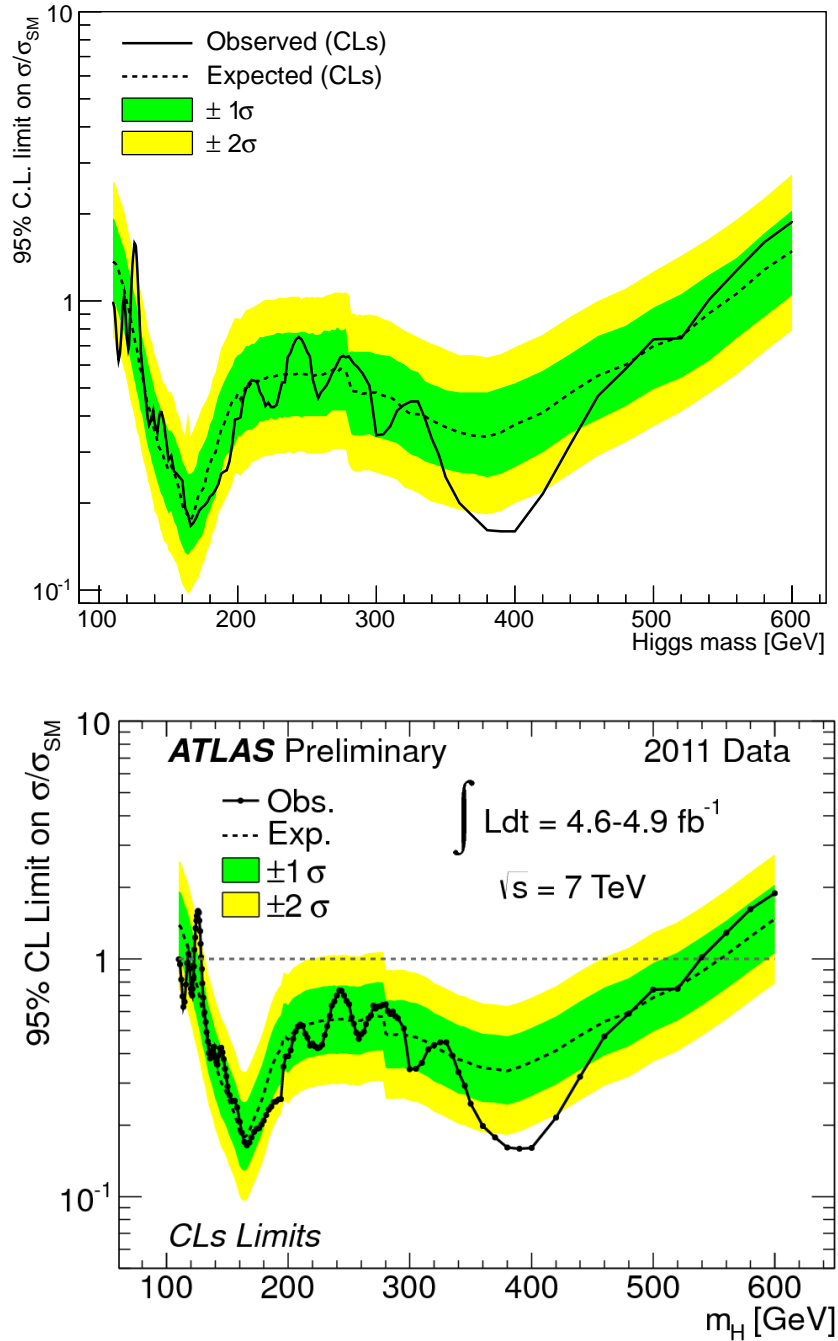


Figure 4.9: Comparison of *MCLimits* (top) and *RooStats* (bottom) limits for the full combination. Analysis represents 4.9fb^{-1} of 7 TeV data.

$m_H = 200$	observed	expected	-1σ	-2σ	$+1\sigma$	$+2\sigma$
MCLimits	0.39	0.48	0.65	0.87	0.34	0.25
RooStats	0.4	0.5	0.7	0.9	0.3	0.2

Table 4.6: Full combination at 200 GeV. *RooStats* values only known to 1 decimal place.

$m_H = 400$	observed	expected	-1σ	-2σ	$+1\sigma$	$+2\sigma$
MCLimits	0.16	0.37	0.52	0.69	0.27	0.20
RooStats	0.2	0.4	0.5	0.7	0.3	0.2

Table 4.7: Full combination at 400 GeV. *RooStats* values only known to 1 decimal place.

the two statistical frameworks are in better numerical agreement as the limits become tighter, see tables (4.5 - 4.7). The expected values and sigma bands agree within, at most, 10% normally within less than 5%. The agreement of the observed values is again within 5% for the mass range up to 350 GeV. For the higher mass range the agreement is within 20%.

The full combination using the full 7 TeV dataset shows that it is possible to produce LHC Higgs limits using **MCLimits** software. It provided a useful double check whilst **RooStats** was undergoing a period of rapid development whilst simultaneously being used to produce official ATLAS results. The logfile outputs created by the workspace extraction method were useful to verify that all the expected components of a channel were present in the workspace and were used to alert groups to missing shape variations in a couple of cases. The **MCLimits** interface was never intended to permanently run concurrent to the **RooStats** results, indeed the greater flexibility of **RooStats** meant that the construction of the workspaces became more and more complex and specific to **RooStats**. It became necessary to rewrite the extraction subroutine for a subchannel every time the production method changed slightly, each time

becoming more and more contrived. With the checks made in the initial periods completed, the `MCLimits` from `Roostats` workspace code wasn't updated for 8 TeV datasets.

Chapter 5

Heavy Higgs Reweighting

5.1 Search for the Heavy Higgs

The original ATLAS letter of intent [52] laid out plans to search for a Standard Model Higgs boson in the range up to 1 TeV. With the discovery of a particle with a mass in the region of 126 GeV one could be forgiven for considering the extension of the SM Higgs search up to 1 TeV as a lower priority. However, with work ongoing to investigate the properties of the new particle it makes sense to continue the search over the entire intended range, not only for the sake of completeness; it is as yet unclear whether the particle found is the SM Higgs boson. There exist several theories beyond the Standard Model which could incorporate a relatively light mass Higgs and still leave room for something at a higher mass. For instance the two Higgs doublet models (THDM) could contain a light SM-like Higgs boson as well as a heavy Higgs boson, with mass splitting allowing the electroweak precision data to be satisfied [53].

At the time of writing, the discovery of the resonance at 126 GeV is recent and theories incorporating this into BSM scenarios are still being implemented.

As experimentalists, the main problem with this is that a lack of a solid theory to test also means a lack of any Monte Carlo simulations to describe this. Hence for now, heavy Higgs searches continue to use SM Higgs signal samples. This doesn't however mean that improvements can't be made for existing and yet to be produced samples. This chapter will describe the work done to implement improved theoretical predictions for heavy Higgs searches (> 600 GeV).

5.2 Complex Pole Scheme

Initial searches for the Higgs boson assumed on-shell (stable) Higgs boson production. The Higgs boson lineshape is estimated by a running or fixed width Breit Wigner distribution. The limitations of this technique become more important for higher masses ($m_H > 400$ GeV) and affect the lineshape [54]. In previous analyses this problem has been addressed in three ways:

- All published analyses stopped at 600 GeV
- The uncertainty on the cross section was computed as $1 + (1.5 \times \frac{m_H}{TeV})^3$
- The lineshape had a conservative theoretical uncertainty, expressed as a percentage and calculated as $150 \times m_H^3$ where m_H is in TeV.

The uncertainty on the lineshape where all analyses stopped, at 600 GeV, was $\pm 32\%$. If the analyses had been extended up to 800 GeV this would have increased to $\pm 77\%$. Clearly, in order to realistically extend the searches a better model with smaller uncertainties would be needed.

Such a model was suggested by Giampiero Passarino and others [55]. In this scheme he starts by considering the complete amplitude of a process, a

combination of the production amplitude, propagator and decay amplitude. This complete amplitude corresponds to the signal, background and interference. For lower Higgs masses ($m_H < 400$ GeV) the interference plays a very small part and so has been ignored up until now. The interference effect for higher masses, however, becomes important and is considered later on in this chapter.

The ideal model calculates the production and decay amplitudes for an off-shell particle and has a propagator which takes account of the virtuality of the particle, which cannot be ignored at higher masses. The reason this hadn't been done previously was mainly because it was very complicated to model the ideal. Passarino *et al.* propose a scheme, known as **OFFP** in the associated paper, which whilst still not being ideal is much better than the existing technique. This is the scheme which I implemented into existing MC samples and tested for heavy Higgs analyses in ATLAS and has become known as the Complex Pole Scheme (CPS).

Of particular concern to this chapter is the propagator. A fixed width Breit-Wigner distribution is represented by:

$$f_{FBW} = \frac{gm}{(s - m^2)^2 + (gm)^2}, \quad (5.1)$$

where m is the Higgs mass, g is the Higgs width and s is the square of the invariant mass of the Higgs. As can be expected, a running width Breit-Wigner distribution introduces an extra dependence on s ;

$$f_{RBW} = \frac{\frac{gs}{m}}{(s - m^2)^2 + (\frac{gs}{m})^2} \quad (5.2)$$

The propagator associated with the CPS uses instead g_{off} which is the width of the off-shell Higgs. It also includes γ_H which is found by taking μ_H (similar to the on-shell mass) as a free parameter in the complex pole parametrisation

$s_H = \mu_H^2 - i\mu_H\gamma_H$. Hence the CPS propagator can be represented as:

$$f_{CPS} = \frac{\sqrt{s}g_{\text{off}}}{(s - \gamma_H m^2)^2 + (gm)^2} \quad (5.3)$$

This chapter focusses on the technical steps taken to implement this lineshape into the existing ATLAS framework. This work builds on the theoretical development of the line width described in full detail in the Passarino paper.

5.3 Reweighting tool

5.3.1 Initial Gluon Gluon Fusion Reweighting

Initial comparisons, see Fig. (5.1) between the Powheg [56] produced Monte Carlo lineshape used in analyses and the lineshape given using the complex pole scheme showed a noticeable difference that increased with the Higgs signal mass. The ideal would be to implement the complex pole scheme into Powheg in place of the Breit Wigner distribution that has been used previously. Future Monte Carlo productions will benefit from this, but time and CPU hour availabilities mean existing Monte Carlo samples will not be recreated. Similar situations to this have arisen previously, and one solution has been to apply a reweighting to the variable(s) in question.

A reweighting tool should:

- work with as many analysis groups' frameworks as possible
- run as a standalone if necessary to check behaviour
- work on an event by event basis

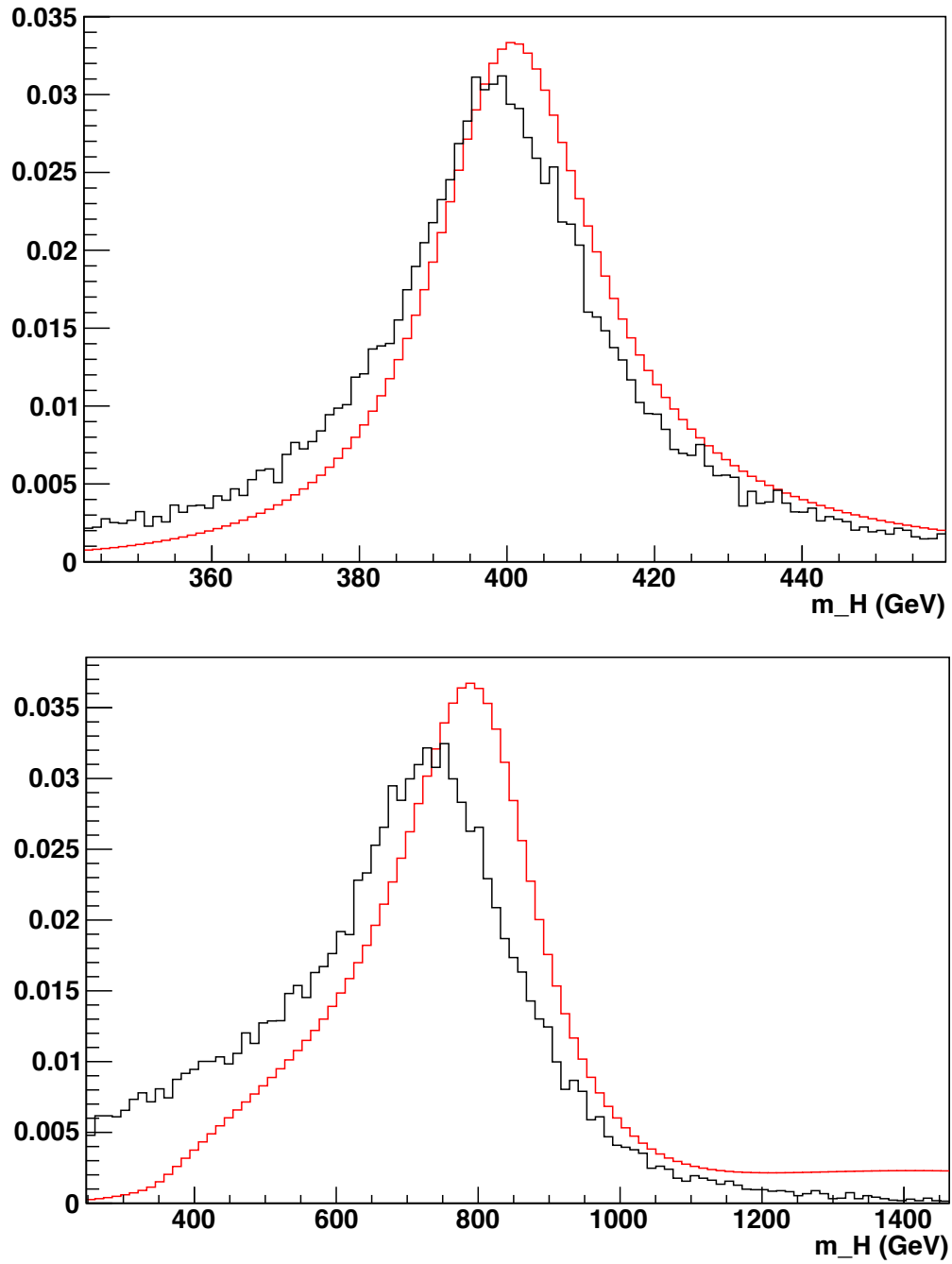


Figure 5.1: *Higgs lineshape distribution comparisons for $m_H = 400$ GeV (top) and $m_H = 800$ GeV (bottom). The distribution given by the complex pole scheme is shown in red whereas the black histogram is taken directly from the gluon gluon fusion 7 TeV Powheg [56] samples.*

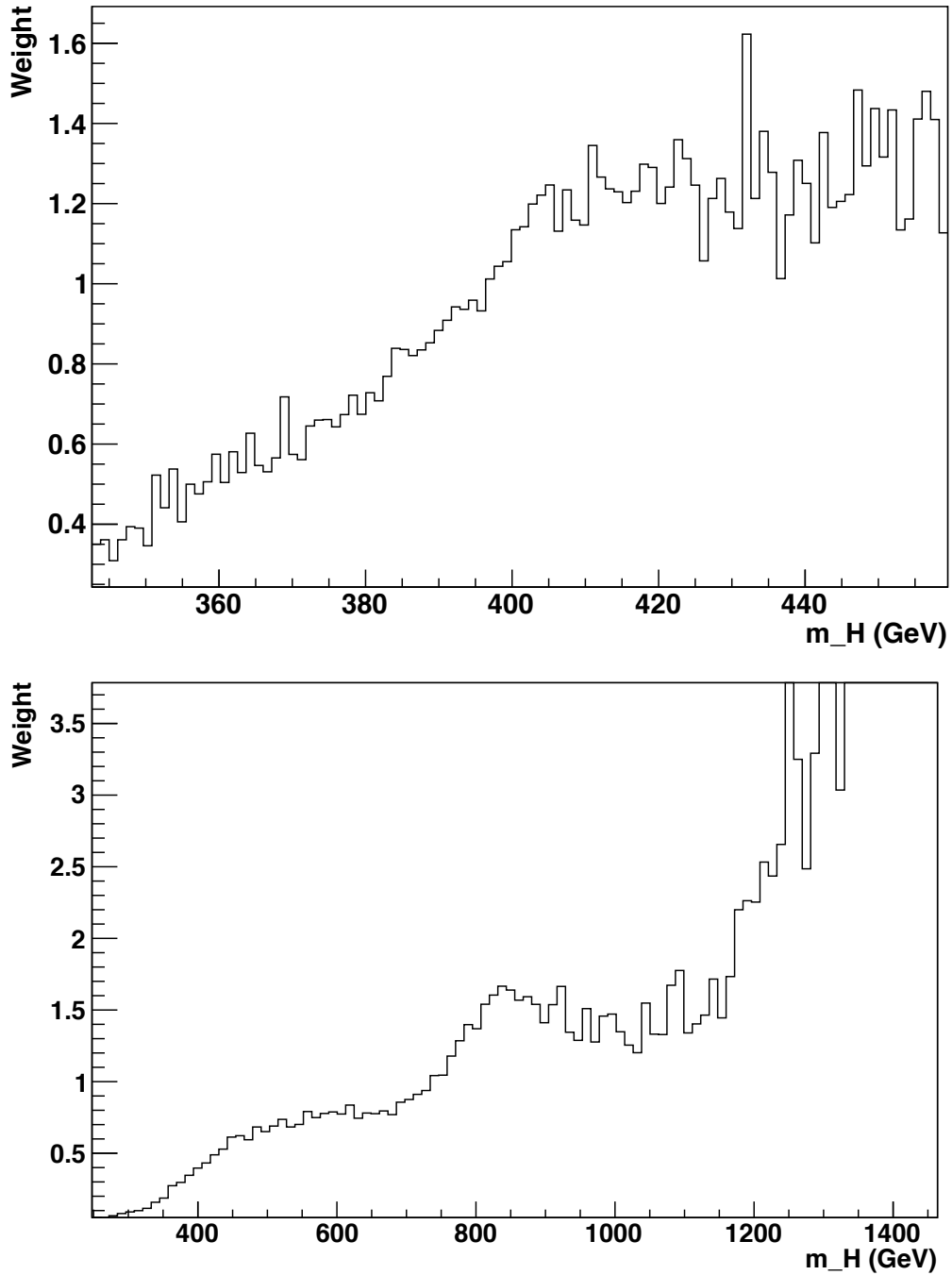


Figure 5.2: *Weight histograms for $m_H = 400$ GeV (top) and $m_H = 800$ GeV (bottom), produced by dividing the complex pole scheme histogram by the Powheg distribution. The lower plot has had its y-axis restricted due to low statistics at higher values of m_H producing very large fluctuations. The plots remain unsmoothed, until a treatment of errors is decided upon.*

- be simple to update.

Initially the distributions for the complex pole scheme were available only for gluon gluon fusion production. A simple first tool was produced which reweighted directly from the existing Powheg to the complex pole scheme. A series of weight histograms was produced, one per Higgs mass. The complex pole scheme distributions came as text files, giving the lower and upper bin edges and the contents of each bin. The data held in these text files were converted into histograms showing the distributions. By creating histograms with identical range and binning to the complex pole scheme and filling them with the data extracted from the Powheg samples it was possible to divide each complex pole scheme histogram by its equivalent Powheg histogram to produce a weight histogram, see Fig. (5.2).

The final piece needed to create a usable tool is the interface between the user and the weights ROOT file. A simple C++ macro was created which takes as input first the Higgs signal mass. This mass is compared to the library of masses for which weight histograms exist. If the signal mass doesn't exist, the tool returns an error explaining that this is the case. If the mass is in the library, the relevant root weight file is opened. Once this has been completed a subroutine can be called to get the weight for a specific found Higgs mass. This can be repeated as necessary for different found Higgs masses all under the same conditions. The subroutine returns the weight, which is found by locating the bin in which the found Higgs mass falls and extracting the content of that bin from the weight histogram. The first implementation of this tool did not concern itself with errors due to theoretical uncertainty on how to treat them. It also did not concern itself with the change in cross section that occurs due to the change in propagator. Both sets of histograms were normalised before dividing to create the weight histogram. The initial idea behind this was to

include the change in cross section in the final inclusive cross section, provided by the Higgs cross section group [57] and used by all the analyses.

5.3.2 Initial Vector Boson Fusion Reweighting

With a sample tool created for gluon gluon fusion (ggF), the next stage was to consider vector boson fusion production. The complex pole scheme code that had been used to create the text files used in ggF reweighting was specific to ggF production. New sample distributions created using the CPS would be needed for VBF production. The Higgs cross section group, amongst others, had for a while been using a program known as HAWK (a Monte Carlo generator for the production of Higgs bosons Attached to Weak bosons at hadron colliders) [58] which includes, amongst other things, NLO QCD and electroweak corrections. The EW corrections reduce the cross sections by 5% [59], but the effect is not flat across the Higgs mass distribution. Since the idea behind the tool was to provide a reweighting factor specific to the point in the distribution where a value falls, the EW correction scaling factor could be included alongside the complex pole scheme reweight.

The HAWK authors were able to implement a subroutine which meant that the lineshape could be either Breit Wigner (as used in concurrent Powheg samples) or the new complex pole scheme lineshape. HAWK distributions were generated for Higgs mass samples between 400 and 900 GeV, which included the electro-weak interference effect and used the complex pole scheme lineshape. As in the ggF tool these were then used as inputs, along with the existing Powheg distributions (which didn't include electro-weak interference effects), to create weight histograms.

Initially, the histograms that were divided to produce the weight histograms

were, as in ggF, the ‘ideal’ (in this case HAWK implementing complex pole scheme and EW corrections) divided by the distributions as they currently were in the Powheg samples in use in analyses. Referring back to fig. (5.1) two main issues arise due to this technique:

- despite gathering as many Powheg samples as possible, limited statistics mean that the Powheg plot has fluctuations from bin to bin, as opposed to the smooth distribution given by the complex pole scheme numbers. These fluctuations are transferred to the weight histograms, see fig. (5.2).
- the Powheg plots have certain features which are not echoed in the shape of the complex pole scheme plots. For instance the lower hand plot in fig (5.1) has a distinct shoulder on the left hand side of the peak, instead of steadily diminishing as the complex pole scheme distribution does. The test files which contained the complex pole scheme distributions, which decided the range and the binning of all the histograms, represented 95% of the total distribution. Outside of this range there would be nothing to reweight with.

These two issues contributed to a decision to create the weights without using the Powheg distributions at all. Instead of having one ‘ideal’ distribution two could be created, using the same machinery, just varying the one thing that was to be changed - i.e. the lineshape. For ggF, Giampiero Passarino agreed to modify his code so it could produce identical results but with a running Briet Wigner distribution. For VBF, HAWK was once again employed to create Powheg-like distributions, with the running BW and also without electro-weak corrections. Both tools were updated to use the new improved weight histograms that had been created by dividing the two ‘ideal’ distributions.

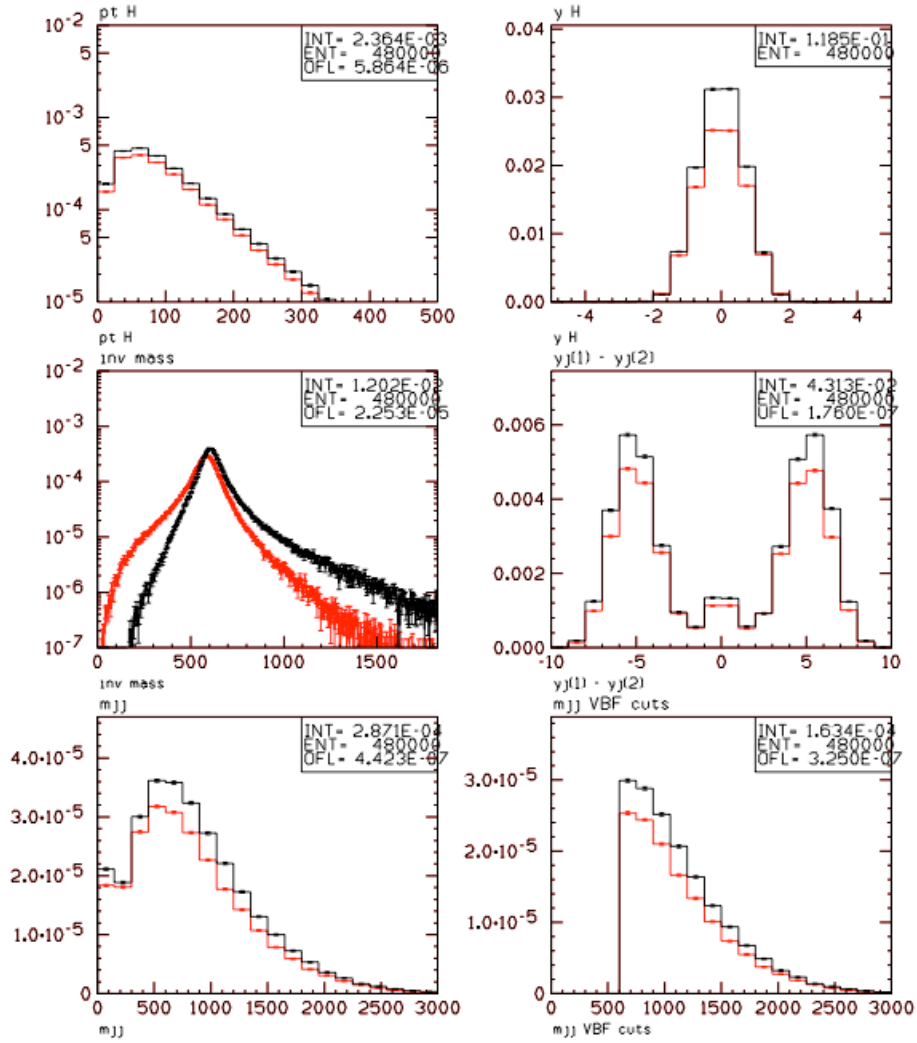


Figure 5.3: Plot made by Carlo Oleari included in this thesis for comparison purposes. This plot shows the output distributions of his Powheg event reweighting tool for a 600 GeV sample. Red shows Breit Wigner running width as in existing Powheg samples and black is the events reweighted to account for the complex pole scheme. Clockwise from top left the sub-plots show; the transverse momentum of the Higgs particle, the rapidity of the Higgs particle, the difference in rapidity of the two leading jets, the summed mass of the two leading jets when cuts designed to isolate VBF events have been applied, the summed mass of the two leading jets without the VBF cuts and finally the invariant mass of the Higgs boson.

At the same time as this first version of the VBF tool was being created, the authors of Powheg also created a Fortran subroutine to reweight Powheg events according to the complex pole scheme prescription. This tool was able to be used for both ggF and VBF production and reweighted the entire event as opposed to just the lineshape, see Fig. (5.3).

The distributions presented by Carlo Oleari, showing before and after his reweighting reiterated that the main difference between the complex pole scheme and the running Breit Wigner was in the lineshape. This meant that the tools that are the subject of this chapter were not made redundant by the Fortran subroutine. Whilst they are less thorough, they have the advantage of being much faster to run and easier to insert into existing C++/ROOT code, which is the predominant language used in ATLAS analyses. The Fortran tool also doesn't include the EW corrections for VBF cases which are not able to be included directly as a flat effect.

The approach of having two very different tools to perform the same thing was particularly useful for cross checking results. The ggF reweighting tool, described earlier, performed well and replicated the results found by the Fortran based Powheg reweighting. The VBF tool however presented a different distribution when reweighted by the two different methods, even when EW effects were accounted for, see fig. (5.4). Whilst the distributions peak in the same region, the normalisation is quite different. This difference was eventually traced to a mistake in the implementation of the complex pole scheme in HAWK. With the mistake corrected the jobs were re-run and the tool updated with new weight histograms.

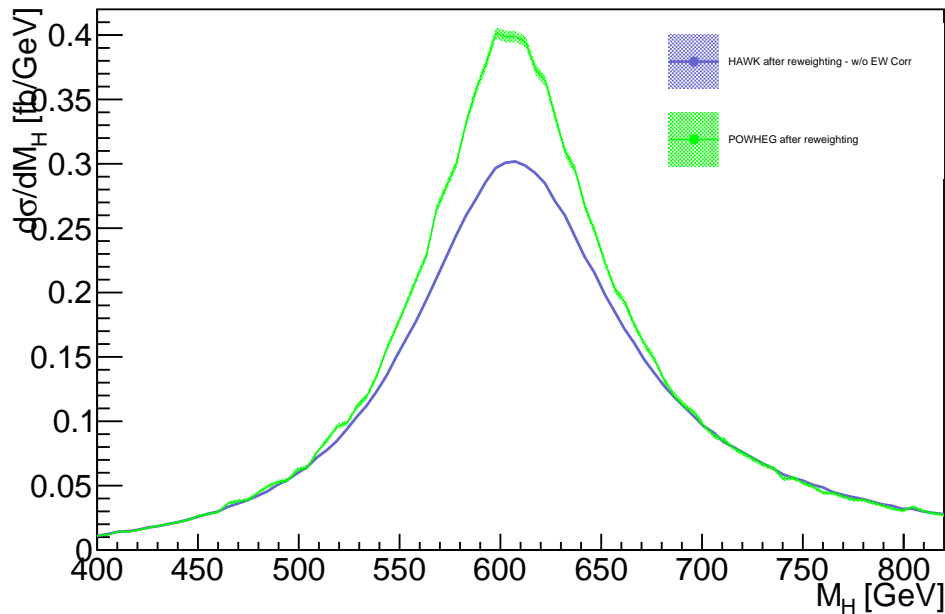


Figure 5.4: A comparison of the complex pole scheme implemented in two different ways, green shows the Powheg reweighting (the output of the Fortran tool) and blue shows the implementation in HAWK. The HAWK plot is without electro-weak corrections. Both curves have been normalised to their own cross-section.

5.3.3 Gluon Gluon Fusion Reweighting Tool, Second Incarnation.

With a tool available for both ggF and VBF, initially the thought was to combine both, and make the production mechanism an option when loading the tool. The combined tool was used by some groups, however there were always plans to improve the tool, for instance by assigning errors to the weights and in the end what was wanted by the different groups meant that the tools diverged once again.

The first round of the ggF tool had dealt only with 7 TeV samples as they were what had been created first. The intention was to reproduce the weight files with 8 TeV samples when they became available and once again add 7 or

8 TeV as an option when loading the tool. In the end the difference between 7 and 8 TeV in terms of the difference between running Briet Wigner and the complex pole scheme was small, so either centre of mass energy weight files could be used. The upgrade of the ggF tool required the analyses of some new samples which were available only in 8 TeV so 8 TeV samples were then used throughout.

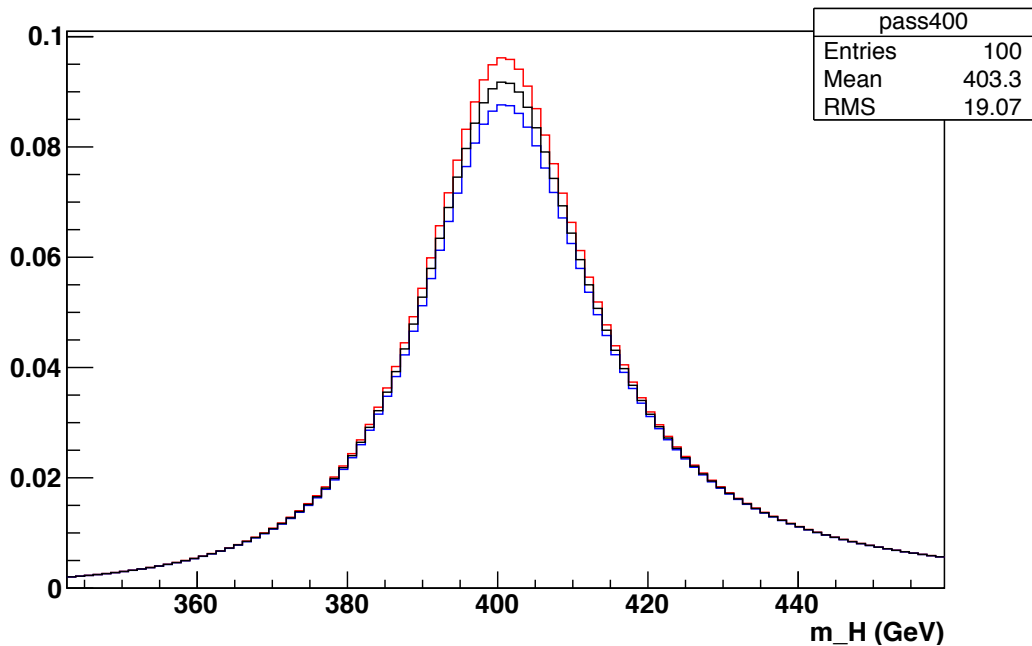


Figure 5.5: *Complex pole scheme distribution for $m_H = 400$ GeV, with maximum (red) and minimum (blue) distributions, used to calculate the percentage errors.*

Groups using or considering using the tool initially requested two improvements: that it would reweight other variables used in their analyses (such as the transverse momentum of the Higgs particle) and that it would also give an error value. The extension to transverse momentum reweighting was produced and presented to the group who had requested it. The effect of the reweighting on the transverse momentum was deemed to be, at that stage, insignificant and no further variables were requested. The prescription for the inclusion of errors was decided upon by Giampiero Passarino who re-ran his code to produce upper and lower limits, varying the uncertainties due to the remaining theoretical

uncertainties, see fig. (5.5). The percentage errors were calculated using the maximum and minimum distributions, dividing the difference between each and the central value by the central value itself.

Like the VBF tool, the reweighting provided for gg^F could also reweight for other effects that had been proposed by theorists after the Monte Carlo samples currently in use had been produced, such as signal-background interference effects in $gg \rightarrow ZZ$ [60].

5.3.4 Higgs Interference Effects.

The current Higgs experimental analyses must take into account uncertainties from a variety of different sources. One section of these uncertainties are theoretical uncertainties which can again be split down into different component parts such as those from missing perturbation terms and those due to imprecise knowledge of the parton density functions. Up until recently the interference effect between the Standard Model Higgs boson and the continuum distributions in $gg \rightarrow ZZ$ was treated as an additional uncertainty. Recent work has made the interference effect partly available and it is in the interest of the experiments to include this as opposed to treating it as a theoretical uncertainty.

The results considered here are for the process $gg \rightarrow ZZ$. The whole cross section can be written as:

$$\sigma_{gg \rightarrow ZZ} = \sigma_{gg \rightarrow ZZ}(S) + \sigma_{gg \rightarrow ZZ}(I) + \sigma_{gg \rightarrow ZZ}(B), \quad (5.4)$$

where S , B and I represent signal ($gg \rightarrow H \rightarrow ZZ$), background ($gg \rightarrow ZZ$) and interference. Whilst the signal processes are known to next to next to leading order (NNLO), background and interference are known only to leading

order (LO). The options available are to use the full LO calculation or try to include a K -factor to have effective NNLO observables. Since at various points in the mass range, the interference effects may be as big as the NNLO correction the effects need to be quantified before choosing a course of action. Starting from a distribution D , such as;

$$D = \frac{d\sigma}{dM_{ZZ}}, \quad (5.5)$$

where M_{ZZ} is the invariant mass of the ZZ pair, the effective distribution can be additive;

$$D_{\text{eff}}^{\text{NNLO}} = D^{\text{NNLO}}(S) + D^{\text{LO}}(I) + D^{\text{LO}}(B), \quad (5.6)$$

or multiplicative;

$$D_{\text{eff}}^{\text{NNLO}} = K_D [D^{\text{LO}}(S) + D^{\text{LO}}(I)] + D^{\text{LO}}(B), \quad K_D = \frac{D^{\text{NNLO}}(S)}{D^{\text{LO}}(S)} \quad (5.7)$$

Both these options are valid only for a restricted ZZ invariant mass range, in effect not going above 1 TeV. Which option is better depends on the region; the multiplicative approach is better for regions with destructive interference, whereas additive approach-[/] is better for regions with positive interference effects.

By considering higher order corrections to the signal and the Higgs virtuality the definition of K_D can be factorised as;

$$K_D = K_D^{gg} = K_D^{\text{rest}}, \quad K_D^{gg} = \frac{D^{\text{NNLO}}(gg \rightarrow H(g) \rightarrow ZZ(g))}{D^{\text{LO}}(gg \rightarrow H \rightarrow ZZ)} \quad (5.8)$$

which leads to a third option, intermediate;

$$D_{\text{eff}}^{\text{NNLO}} = K_D D^{\text{LO}}(S) + (K_D^{gg})^{1/2} D^{\text{LO}}(I) + D^{\text{LO}}(B) \quad (5.9)$$

which is believed to best simulate the inclusion of K -factors at the amplitude level.

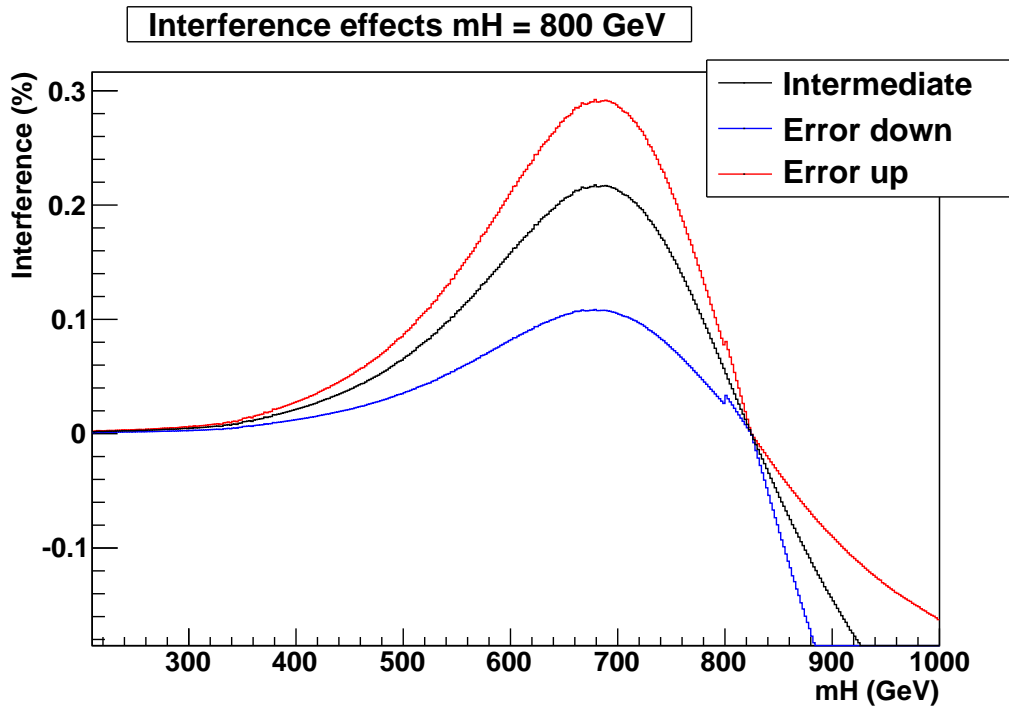


Figure 5.6: *Interference effect for $m_H = 800$ GeV, with maximum (red) and minimum (blue) distributions, used to calculate the percentage errors. Step visible in error plots at $m_H = 800$ GeV an artifact of the switch between the two distributions.*

As recommended by theorists the intermediate option for the distribution is used to calculate the effect of the interference. This can be expressed as a percentage allowing it to be applied as a reweighting in a similar way to the CPS reweighting. Upper and lower limits are derived by comparing the intermediate value with the additive and multiplicative values. For masses below the central lineshape distribution value the multiplicative distribution gives a larger value and so is used to calculate the upper error, however after the peak the larger value is provided by the additive meaning for these values the additive is used to calculate the upper error. The switch is echoed in the lower error calculations, see fig, (5.6).

The reweighting tool was modified to require two boolean statements as input, controlling whether the end reweighting value and associated error came

from the complex pole scheme, the interference or both. If the reweighting was to take account of both CPS and interference the reweighting factor was given as the multiple of the two separate reweighting factors and associated errors for each were combined in quadrature. The splitting of the two effects is important to allow as many different MC samples to be reweighted as possible. The MC samples used for 7 TeV analysis should use both reweightings, as should the 8 TeV samples up to 600 GeV. However 8 TeV samples above 600 GeV which are still to be produced should already include the CPS and so need just to be reweighted for interference effects.

5.3.5 Vector Boson Fusion Reweighting Tool Extension

With groups starting to use the tools, there was a request from one group to extend the tool to reweighting the p_T distribution as well; however after implementation of this feature it was agreed that the effect was too small to warrant its inclusion in the current analyses. It also became clear the VBF tool would have to be extended to reweight 8 TeV MC samples. This provided an opportunity to check whether the assumption made by the ggF group that the same reweighting could be applied for both 7 and 8 TeV would hold for the VBF case as well.

The input distributions were once again provided by HAWK. The normalised distributions and weight histograms were compared for the 7 and 8 TeV cases, see fig. (5.7). The two weight histograms were very different in shape, indicating that, in the current situation it wouldn't be possible to use one weight histogram for both reweightings. The extent of the difference in the two weighting histograms was unexpected and warranted further investigation.

Fig. (5.8) shows the comparison of the HAWK produced plots, using the

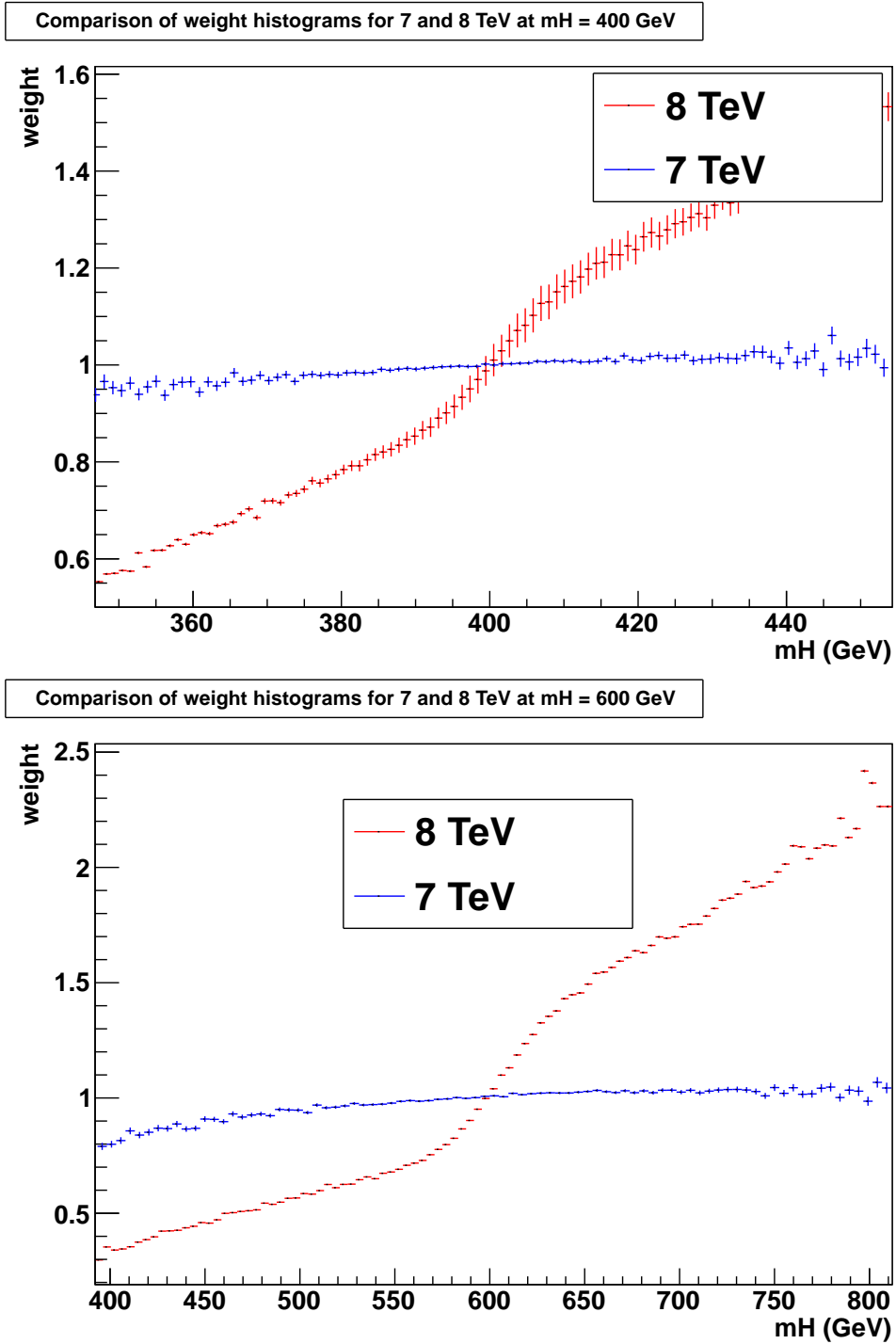


Figure 5.7: Comparison of 7 (blue) and 8 TeV (red) weight histograms for $m_H = 400$ GeV (top) and 600 GeV (bottom).

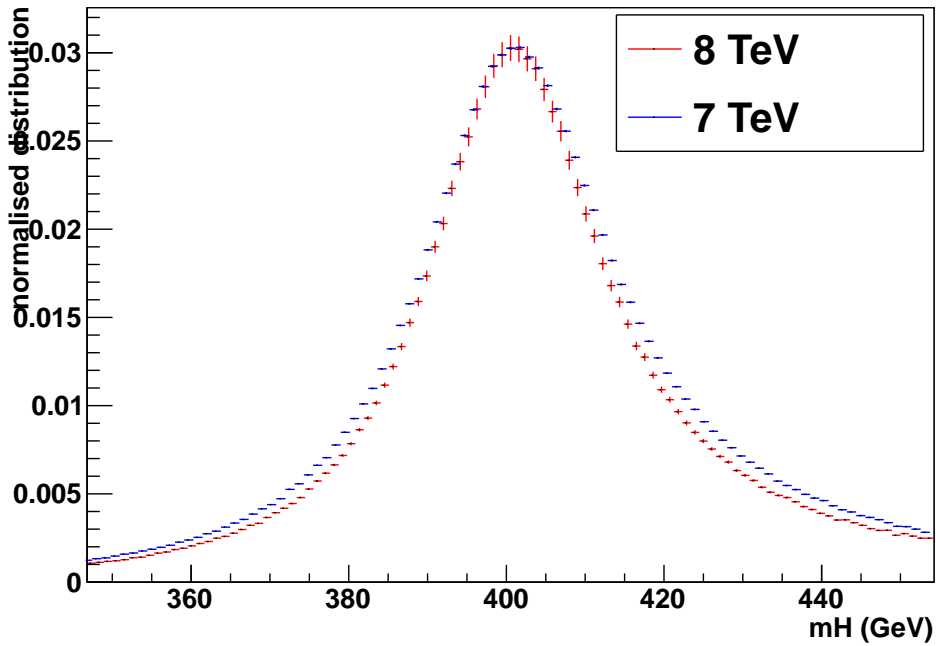
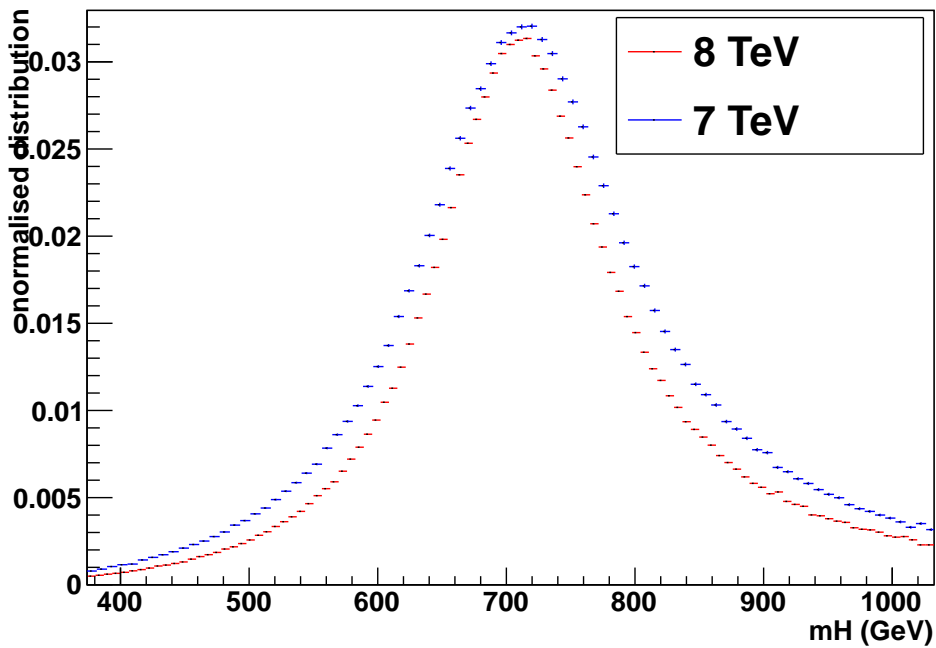
Comparison of CPS+EW input histograms for 7 and 8 TeV at $m_H = 400$ GeVComparison of CPS+EW input histograms for 7 and 8 TeV at $m_H = 700$ GeV

Figure 5.8: Comparison of 7 (blue) and 8 TeV (red) Complex Pole Scheme distributions for $m_H = 400$ GeV (top) and 700 GeV (bottom), both produced using HAWK. Distributions include electro-weak effects. Both plots are normalised. The difference in apparent height is due to differing ranges between the two distributions.

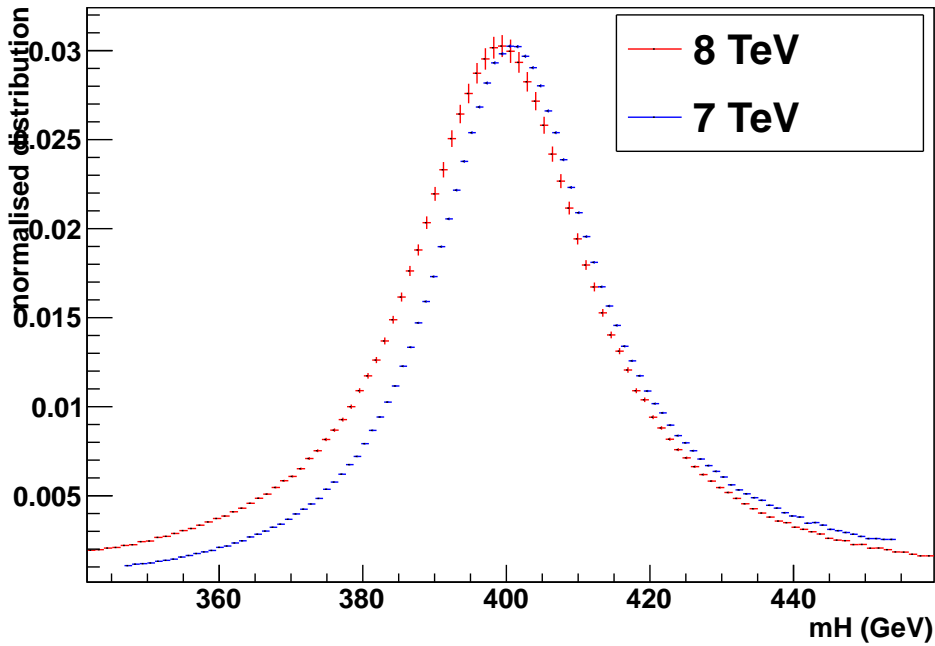
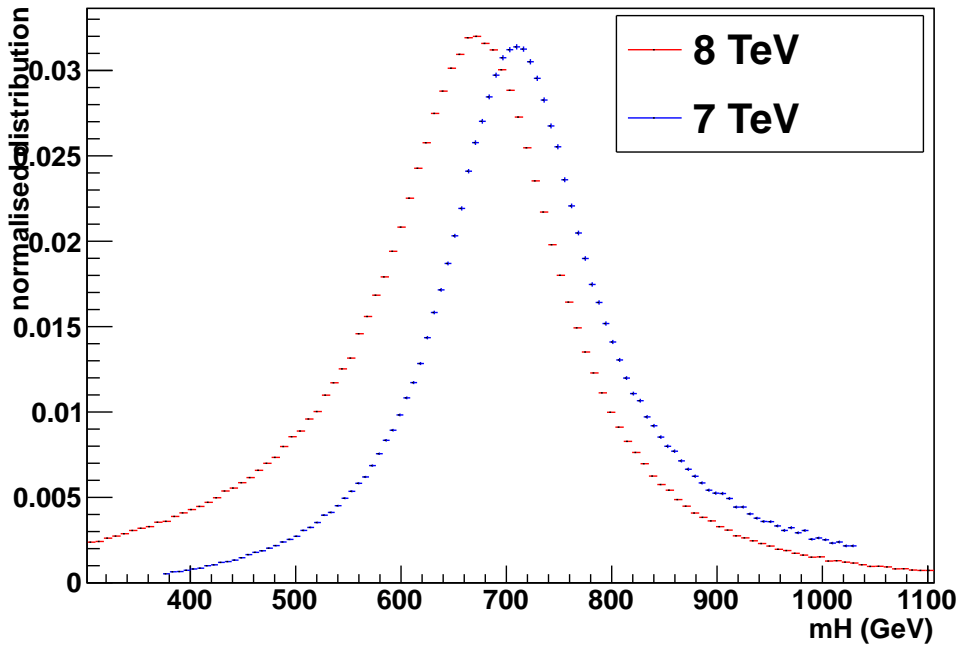
Comparison of BW input histograms for 7 and 8 TeV at $m_H = 400$ GeVComparison of BW input histograms for 7 and 8 TeV at $m_H = 700$ GeV

Figure 5.9: Comparison of 7 (blue) and 8 TeV (red) running width Breit Wigner distributions for $m_H = 400$ GeV (top) and 700 GeV (bottom), both produced using HAWK. Difference in peak position is the cause of the unusual behaviour seen in the weight histograms and is to be investigated further.

complex pole scheme and including electro-weak corrections. The distributions remain the same between 7 and 8 TeV. The difference in the weight histograms must then come from the Breit Wigner input distributions, see fig. (5.9). The input test files were checked; since HAWK automatically includes EW correction factors these have to be subtracted to create the distributions imitating Powheg, however no error could be found in these calculations. The next check was a comparison of the Powheg sample against the HAWK distribution that was supposed to represent the same conditions as the Powheg, e.g. running Breit-Wigner and no EW corrections, see fig. (5.10). The comparison plots would indicate that there is a problem with the 7 TeV ‘a la Powheg’ HAWK samples. This is being investigated but still remains unsolved.

5.3.6 Current and Future Use for the Tools.

The extension of the search for the SM Higgs boson above 600 GeV has, up until now, been infeasible due to theoretical uncertainties becoming too large. These searches will make use of 7 and 8 TeV data taken in the entire run so far. It would be unrealistic to expect existing MC simulations to be recreated to include the new advances. A simple to use reweighting tool seems like a sensible option for the quick implementation of the effects due to new or adjusted theoretical calculations.

The disadvantage of the tools created here is how dependant they are on the two input distributions and the distribution to be reweighted. As shown in the previous section, if an input plot is generated incorrectly or shows a feature that is not understood it will affect the weight histogram and thus the reweighted product. The disadvantage was shown once again during comparisons between new Powheg samples produced with CPS implemented and new BW Powheg samples reweighted using these tools. The latest version of Powheg was used

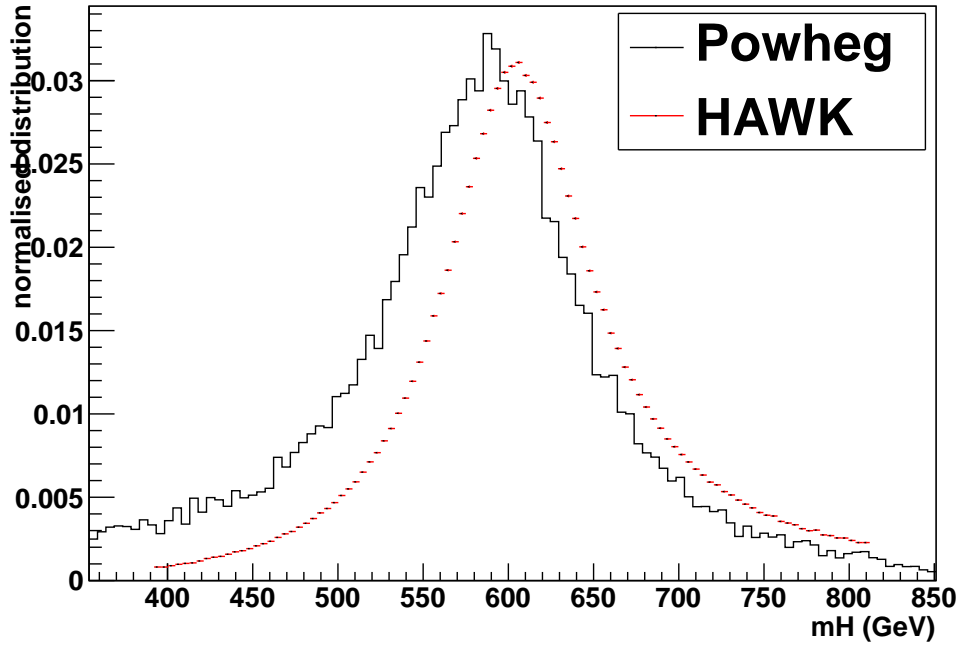
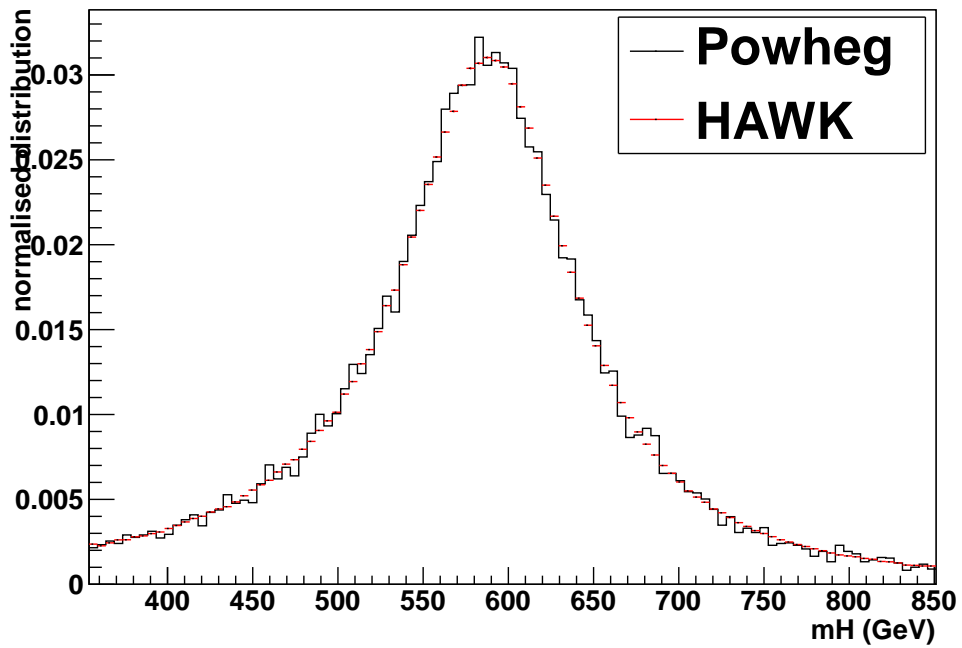
Comparison of HAWK 'a la Powheg' and Powheg 7 TeV samples at $m_H = 600$ GeVComparison of HAWK 'a la Powheg' and Powheg 8 TeV samples at $m_H = 600$ GeV

Figure 5.10: Comparison of running width Breit Wigner distributions for $m_H = 600$ GeV produced by Powheg (black) and HAWK configured to reflect the Powheg setup (red) for 7 (top) and 8 TeV (bottom).

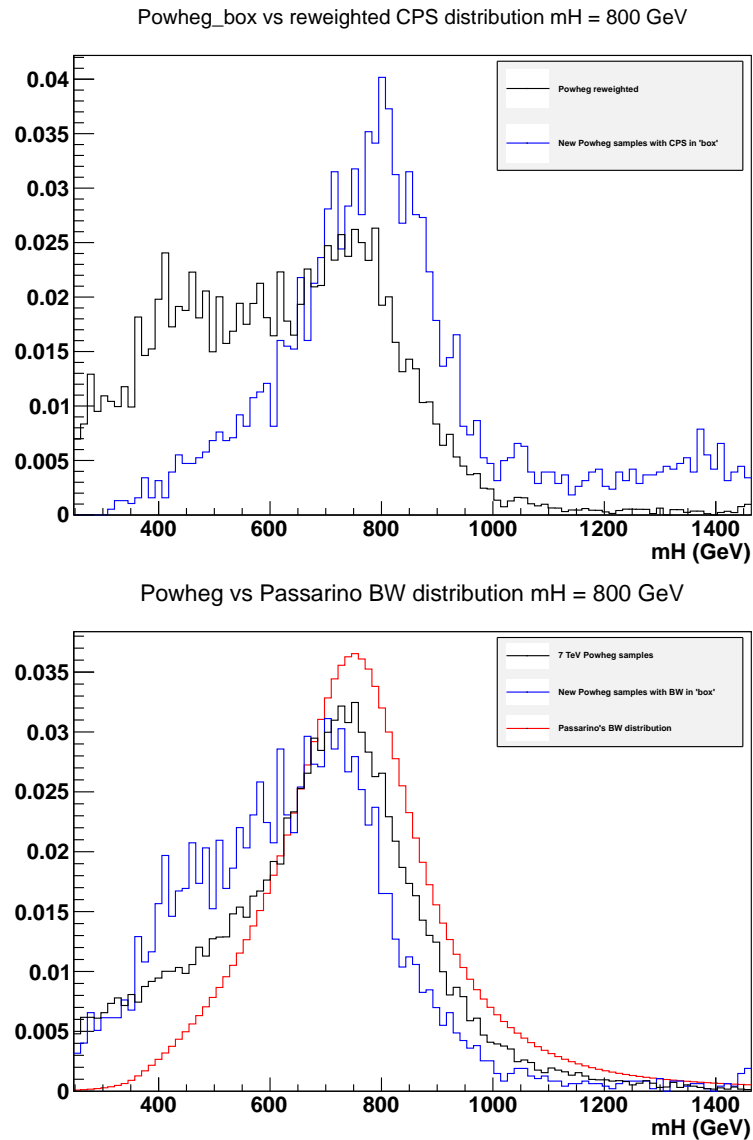


Figure 5.11: The top plot shows a comparison of new 8 TeV $m_H = 800$ GeV samples produced using CPS (blue) within Powheg and using a BW distribution and then reweighted using the ggF reweighting tool (black). The bottom plot is a comparison of running width Breit-Wigner distributions. Red shows the idealised distribution produced by Passarino and used as input to the reweighting tool, black shows the 7 TeV Powheg samples, blue shows the new 8 TeV samples produced especially for tests.

to generate two sets of samples; one using the Breit-Wigner distribution and one using the complex pole scheme, now implemented within Powheg. Fig. (5.11) top plot shows a comparison between the CPS Powheg sample and the BW Powheg sample reweighted with the ggF reweighting tool. The two plots do not agree well. Fig. (5.11) bottom plot is a comparison of the Breit-Wigner distributions. The smooth red curve is the ideal running width Breit-Wigner distribution provided by Giampiero Passarino and used as input to the reweighting tool. The black and blue lines show the Powheg running width Breit-Wigner samples for 7 and 8 TeV respectively. The 8 TeV sample has large fluctuations due to low statistics, however there is a visible bump in the range 300-700 GeV. In this range the 8 TeV sample is far above the 7 TeV sample and as a result pulls the entire normalised distribution. The bump in this sample will be carried through when reweighted using the tool; if the distribution that's being reweighted differs greatly from the sample distribution used to represent unreweighted conditions the reweighted distribution will also differ greatly from the sample CPS distribution.

Because of the odd behaviour of the 8 TeV Powheg sample between 300 and 700 TeV a better comparison of the reweighting tool and new Powheg with CPS implemented inside would be to reweight the 7 TeV Powheg, see fig. (5.12) top plot. Here the ideal CPS distribution is shown in red, blue shows Powheg with CPS implemented internally and black is reweighted 7 TeV Powheg. There are two main things to note:

- The shoulder at the lower end of the mass range, present in the reweighted 7 TeV Powheg distribution.
- The divergence of the 8 TeV Powheg with CPS from the other two distributions at the higher end of the mass range.

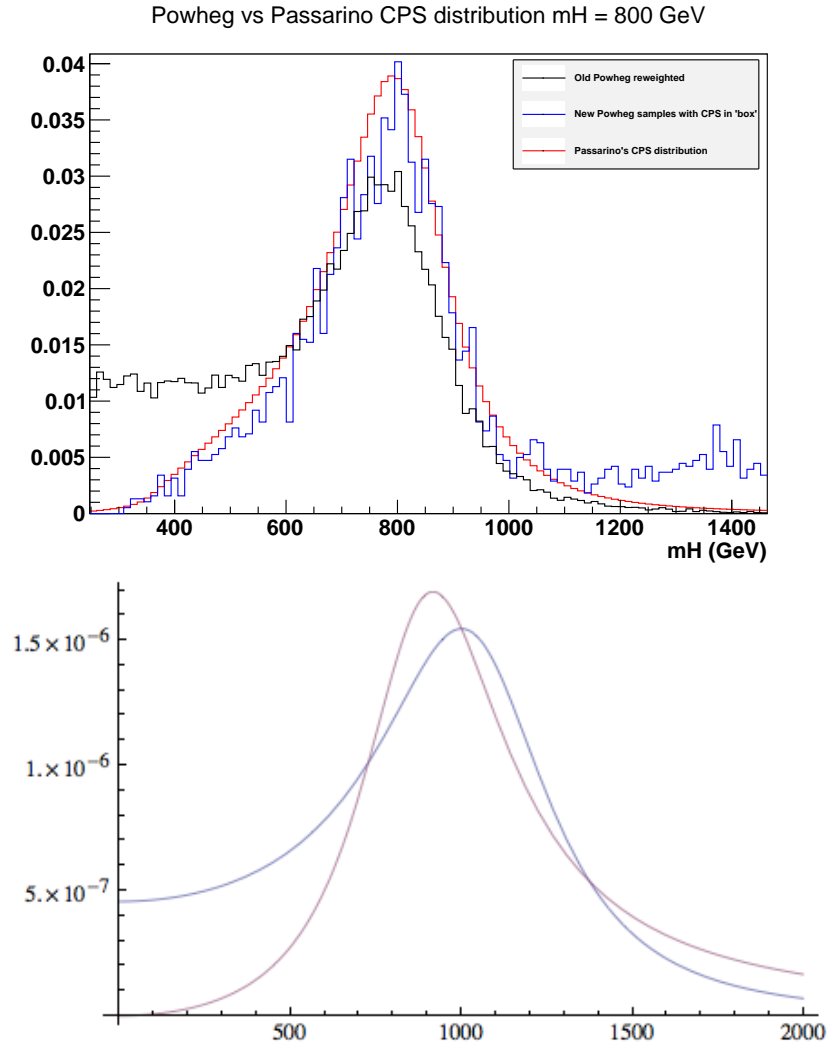


Figure 5.12: The top plot shows a comparison of normalised Higgs boson distributions for $m_H = 800$ GeV. The red line is the ‘ideal’ distribution produced by Passarino, the blue line shows the 8 TeV Powheg distribution produced using CPS implemented within Powheg. The black line shows the 7 TeV Powheg distributions produced using a BW distribution and then reweighted to imitate the CPS. The bottom plot is a sample plot produced by Sara Bolognesi contrasting a fixed width Breit-Wigner distribution (blue) to a running width distribution (red). Both distributions are for $m_H = 1000$ GeV.

Both the 7 TeV Powheg sample and the newer 8 TeV BW Powheg sample differ from BW distribution at the lower end of the range, showing a left hand shoulder. Fig. (5.12) bottom plot shows a histogram created by Sara Bolognesi of CMS and the LHC Higgs Cross Section Working Group. Her plots shows the two Breit-Wigner distributions for $m_H = 1000$ GeV, blue is fixed width and red is running width. This plot would seem to show that the BW distribution in the 7 TeV Powheg samples, despite what the creators of these samples thought, is fixed width. The 8 TeV new BW Powheg sample could well be fixed width as well but the lack of statistics and the presence of the bump make it not so obvious as the 7 TeV case.

The presence of the tail for the 8 TeV Powheg with CPS distribution is being investigated by other members of the collaboration and the people responsible for implementing CPS within Powheg.

Whether a reweighting factor is provided by these tools or not, the machinery will be useful in other ways. Some channels are using it just to provide errors, which are easily accessible per value, but also as an overall error histogram which can then be stored in a root file/XML combination and used with the HistFactory machinery when performing statistical analyses. The ggF tool also provides a reweighting to account for the most up to date theories describing interference effects, currently only for $H \rightarrow ZZ$ but with an extension to $H \rightarrow WW$ to be implemented soon. The tool was designed in such a way so that it can be used just for interference effects if the sample already uses the CPS.

The machinery created during the development of these tools was made to be as generic as possible. This means it can be quickly adapted to other situations; if some data files exist or can be made showing a distribution before and after the implementation of a new idea or theory, the tool can offer a

quick way to test the effect of this change. Since the completion of this work I received several requests for the tool. Upon leaving the field I updated the tool one last time and bequeathed it to a colleague. As of March 2014, the tool was being proposed as being the official tool for reweighting by Higgs Sub Group 4, adapted to meet their needs as they see best.

Chapter 6

Conclusions

The start of 2015 will see the restart of the LHC, its injection chain having been restarted towards the end of 2014 in anticipation. The conditions for the experiments in Run 2 will be even more complex than those seen in Run 1, as the pursuit of ever more integrated luminosity continues.

The achievements of the LHC experiments with the data produced during Run 1 are incredible. One of the main goals of the LHC was to find the Higgs boson. The teams of ATLAS and CMS managed to find a new particle, likely to be the Higgs, after only a year and a half of data taking. The speed with which analyses are done in the LHC era should leave people, more than ever, searching for cross-checks for their results.

This thesis presented several Higgs boson limit results calculated using an alternative statistical framework to that chosen for official ATLAS results. The limits set by the two frameworks were not in good agreement at low integrated luminosity values for single channels, but agreement improved with increased integrated luminosity and for combinations of several channels. Where they differed, the alternative statistical framework produced tighter results than the

official framework, implying the official results are conservative.

In complex analyses, such as the search for the Higgs boson, a dual technique approach provides a cross-check for all stages from input, through analyses algorithms and finally to error calculations. The sheer scope and speed of the analyses performed by ATLAS meant that it became very difficult to maintain the `MCLimits` framework single-handedly, and after the calculation of the results shown here the effort was not continued. One of the advantages of `RooStats` as a statistical framework is, because of the separation of the model and the calculator, internal cross-checks can be performed. With a sufficiently well maintained code and accompanying documentation it should be possible for several groups to perform the same calculations, benchmarking each others results as they go.

The work done in comparing limit setting machinery highlighted just how important the minimisation of uncertainties is. An incorrectly applied, or omitted, uncertainty can, depending on the scale of the uncertainty, have a sizeable effect on the limit setting results produced. The work done on the inclusion of the complex pole scheme in ATLAS heavy Higgs analyses shown in this thesis resulted in a reweighting tool. In its current form the reweighting tool is specifically to modify existing monte carlo samples to better reflect the complex pole scheme model. The mechanics of the tool are, however, sufficiently generic to be able to be modified to reweight diverse quantities rapidly updating or testing new theories without the need for intense monte carlo sample production campaigns. The tool is now standard within several heavy Higgs analysis groups and it's modification and adaptation is encouraged.

Bibliography

- [1] `www.cern.ch`
- [2] Wyss, Carlo (ed.). *LEP design report, v.3* CERN-AC-96-01-LEP-2. 1996
- [3] Regenstreif, Edouard. *The CERN Proton Synchrotron* CERN-59-29. 1962
- [4] *The 300 GeV programme.* CERN-1050-E. 1972.
- [5] *ATLAS: Detector and physics performance technical design report.* Volume 1. CERN-LHCC-99-14.
- [6] *CMS Physics : Technical Design Report Volume 1: Detector Performance and Software.* CERN-LHCC-2006-001
- [7] *LHCb : Technical Proposal.* CERN-LHCC-98-004
- [8] *ALICE : Technical proposal for a Large Ion collider Experiment at the CERN LHC.* CERN-LHCC-95-71
- [9] *Luminosity Determination in pp Collisions at $\sqrt{s}=7$ TeV Using the ATLAS Detector at the LHC.* Eur.Phys.J.C71:1630, 2011
- [10] *ATLAS inner detector : Technical Design Report, 1.* CERN-LHCC-97-016
- [11] *ATLAS liquid-argon calorimeter : Technical Design Report.* CERN-LHCC-96-041

-
- [12] *ATLAS tile calorimeter : Technical Design Report*. CERN-LHCC-96-042
- [13] M. Aharrouche, et al., *Energy Linearity and Resolution of the ATLAS Electromagnetic Barrel Calorimeter in an Electron Test-Beam.*, Nucl.Instrum.Meth.A568:601-623,2006
- [14] U Bratzler on behalf of the ATLAS Collaboration, *The ATLAS muon precision chamber system.* , Nuclear Instruments and Methods in Physics Research Section A: Accelerators, Spectrometers, Detectors and Associated Equipment, Volume 409, Issues 1?3, 21 May 1998
- [15] M. E. Peskin and D. V. Schroeder, *An Introduction to Quantum Field Theory*. Westview Press, 1995.
- [16] ATLAS Collaboration, *Evidence for the spin-0 nature of the Higgs boson using ATLAS data*. Phys. Lett. B 726 (2013) 120
- [17] J. Beringer et al. (Particle Data Group), Phys. Rev. D86, 010001 (2012)
- [18] S. Glashow, Nucl. Phys. 22, 579, 1961.
- [19] S. Weinberg, Phys. Rev. Lett. 19, 1264, 1967.
- [20] A. Salam, *Elementary Particle Theory*, W. Svartholm, Almquist and Wiksell, Stokholm, 1968.
- [21] Goldstone, J. *Field Theories with Superconductor Solutions*, Nuovo Cimento 19: 154?164, 1961
- [22] P Higgs, *Broken symmetries, massless particles and gauge fields*, Phys. Lett., 12:132-133, 1964
- [23] P Higgs, *Broken symmetries and the mass of gauge bosons*, Phys Rev Lett, 13:508- 509, 1964

- [24] G.S. Guralnik, C.R. Hagen and T.W.B. Kibble, *Global conservation laws and massless particles*, Phys. Rev. Lett. 13: 585-7, 1964
- [25] Englert, F and Brout, R, *Broken symmetry and the mass of gauge vector mesons.*, Phys. Rev. Lett. 13: 321-3, 1964
- [26] S. Dawson, *Introduction to electroweak symmetry breaking*, arXiv: hep-ph/9901280.
- [27] ALEPH, DELPHI, L3 and OPAL Collaborations, *Search for the Standard Model Higgs Boson at LEP*, CERN-EP/2003-011, Phys. Lett B565 (2003) 61-75.
- [28] CDF and D0, *Combined CDF and D0 Upper Limits on Standard Model Higgs Boson Production with up to 8.6 fb⁻¹ of Data* arXiv:1107.5518 [hep-ex]
- [29] <http://lepewwg.web.cern.ch/LEPEWWG/plots/summer2011/>
- [30] FERMILAB-CONF-12-318-E; CDF Note 10884; D0 Note 6348
- [31] *Official press release* <http://www.atlas.ch/news/2012/latest-results-from-higgs-search.html>
- [32] *Official press release* <http://cms.web.cern.ch/news/observation-new-particle-mass-125-gev>
- [33] *Oxford Dictionaries Online*, Oxford University Press, <http://oxforddictionaries.com/>
- [34] G.Cowan, K. Cranmer, E. Gross, O. Vitells *Asymptotic formulae for likelihood-based tests of new physics* Eur.Phys.J.C71:1554,2011
- [35] A.T Doyle, S. Ferrag, C. Wright *Sensitivity studies using ttH at the LHC* ATL-COM-PHYS-2008-024

- [36] A.L. Read, *Presentation of search results: the CLs technique* J. Phys. G 28, 2693 (2002) *Modified frequentist analysis of search results (the CLs method)* CERN-OPEN-2000-205.
- [37] Robert D. Cousins and Virgil L. Highland. *Incorporating systematic uncertainties into an upper limit*. Nucl.Instrum.Meth., A320:331335, 1992.
- [38] *Combined CDF and D0 Upper Limits on Standard Model Higgs-Boson Production with 2.1 - 5.4 fb⁻¹ of Data* arXiv:0911.3930v1 [hep-ex]
- [39] ATLAS, CMS, *Procedure for the LHC Higgs boson search combination in Summer 2011* ATL-PHYS-PUB-2011-11, CMS NOTE-2011/005.
- [40] Eilam Gross and Ofer Vitells. *Trial factors for the look elsewhere effect in high energy physics*. The European Physical Journal C - Particles and Fields, 70:525–530, 2010. 10.1140/epjc/s10052-010-1470-8.
- [41] Tom Junk. *Sensitivity, Exclusion and Discovery with Small Signals, Large Backgrounds, and Large Systematic Uncertainties* CDF 8128 http://www-cdf.fnal.gov/~trj/mclimit/mclimit_csm.pdf
- [42] <http://root.cern.ch/drupal/>
- [43] T. Junk, *Building a More General χ^2* , CDF 7904
- [44] J. Heinrich, *Bayesian limit software: multi-channel with correlated backgrounds and efficiencies*, CDF 7587.
- [45] Lorenzo Moneta, Kevin Belasco, Kyle Cranmer, Sven Kreiss, Alfio Lazzaro, Danilo Piparo, Gregory Schott, Wouter Verkerke, Matthias Wolf, *The RooStats Project* arXiv:1009.1003v2 [physics.data-an]
- [46] <http://root.cern.ch/drupal/content/roofit>

- [47] <https://twiki.cern.ch/twiki/pub/RooStats/WebHome/HistFactoryLikelihood.pdf>
- [48] <http://www.w3.org/TR/REC-xml/>
- [49] <https://cdsweb.cern.ch/record/1453249/files/ATL-COM-PHYS-2012-732.pdf>
- [50] The ATLAS Collaboration. *Search for the Standard Model Higgs boson in the diphoton decay channel with 4.9fb^{-1} of pp collisions at $\sqrt{s} = 7\text{ TeV}$ with ATLAS*, Phys. Rev. Lett. 108 (2012) 111803
- [51] The ATLAS Collaboration. *Combined search for the Standard Model Higgs boson in pp collisions at $\sqrt{s} = 7\text{ TeV}$ with the ATLAS detector*, Phys. Rev. D86 (2012) 032003
- [52] *ATLAS:letter of intent for a general-purpose pp experiment at the large hadron collider at CERN*. <http://atlas.web.cern.ch/Atlas/internal/tdr.html>
- [53] S. Kanemura, Y. Okada, H. Taniguchi and K. Tsumura *Indirect bound of heavy scalar masses of the two-Higgs-doublet model in light of recent Higgs boson searches*. Phys.Lett B704 (2011) 303-307
- [54] M.H. Seymour, *The Higgs boson line shape and perturbative unitarity*, Phys. Lett. B354 (1995) 409-414
- [55] Stephano Gorla, Giampiero Passarino and Dario Rosco *Higgs boson line-shape* arXiv:1112.5517v2[hep-ph]
- [56] <http://powhegbox.mib.infn.it/>
- [57] LHC Higgs Cross Section Working Group: S. Heinemeyer, C. Mariotti, G. Passarino, R. Tanaka (eds.) *Handbook of LHC Higgs Cross Sections: 3. Higgs Properties* arXiv:1307.1347 [hep-ph]

-
- [58] A. Denner, S. Dittmaier, A. Mück. *A Monte Carlo generator for the production of Higgs bosons Attached to Weak bosons at hadron colliders*. <http://omnibus.uni-freiburg.de/~sd565/programs/hawk/hawk.html>
- [59] M.Ciccolini, A. Denner, S. Dittmaier. *Strong and electroweak corrections to the production of Higgs+2jets via weak interactions at the LHC* Phys.Rev.Lett.99:161803,2007
- [60] Giampiero Passarino *Higgs Interference Effects in $gg \rightarrow ZZ$ and their uncertainty*. arXiv:1206.3824v2[hep-ph]